THE APPLICATION OF LOW COHERENCE INTERFEROMETRY TO THE MICRON SCALE IMAGING OF THE LIVING HUMAN RETINA

A THESIS SUBMITTED TO

THE UNIVERSITY OF KENT

IN THE SUBJECT OF PHYSICS

FOR THE DEGREE

OF DOCTOR OF PHILOSOPHY

George Dobre

March 2000

Acknowledgements

It is a great pleasure to begin by recalling the people who have offered me their support throughout my years at Kent. These are:

Professor David Jackson who, in his capacity as supervisor, gave me not only constant guidance and frequent and valuable suggestions but also sustained motivation, a great deal of practical help and moral support.

Dr Adrian Podoleanu, who has always been, if I may modestly say so, an example of total commitment and enthusiasm. The hard working attitude that he instils in his collaborators, together with his stubborn non-acceptance of any kind failure, was essential in achieving the goals of this project.

Mauritius Seeger, the perfect colleague (I mean it!) and a great friend.

All the members of the Physics Department, and especially the boys in the Electronics and Mechanical Workshops for completing various jobs at short notice, usually from diagrams written on the back of an envelope.

My parents, as the people who have invested most in me in terms of hope and aspiration, deserve a very special mention and it is to them that this work is dedicated.

And finally, my wife Silvia, who, by unconditionally lending me her emotional support, provided me with the most important reasons to keep going that anyone could have.

Abstract

Current optical and ultrasound techniques for high resolution *in vivo* retinal imaging cannot provide the depth accuracy required to enable sensitive ophthalmologic diagnosis to be carried out on the basis of images of retinal microstructures. The axial depth resolution of one of the recently introduced retinal imaging instruments, the scanning laser ophthalmoscope, is restricted by the combined effect of the depth of focus achievable through the eye pupil and aberrations to about 300 μm.

A new imaging technique, based on low coherence interferometry, providing improved depth resolution figures of the order of a few microns, is demonstrated here. Non-invasive topographic and tomographic measurements can be performed with an instrument based on this technique.

A novel path modulation procedure, the Newton rings sampling function, is presented together with experimental results obtained in its application to the imaging of various objects including human *in vivo* retina.

The advantages and disadvantages of novel and more conventional imaging modes, their associated techniques and the overall importance and likely impact of the novel Newton rings modulation method are considered.

The measurement of 3-dimensional profiles of various targets, including tomographic images of *in vivo* human retinas from volunteers' eyes, is presented.

The utility of OCT measurements in the high-resolution mapping of *in vivo* tissue and its potential usage alongside scanning laser ophthalmoscopy in identifying features in the human eye are discussed.

Contents

1. Overview of high resolution non-contact surface profiling and eye imaging

1.1 Introduction

The present work is organised in seven chapters.

Chapter 1 is an overview of current activity in optical and non-optical surface profiling and eye imaging techniques related to the scope of the research presented here. The application of interferometric techniques alongside other established techniques for the measurement of surfaces and intra-ocular distances and topography is reviewed. Chapter 2 contains a review of the theoretical aspects of low coherence interferometry and fiberised interferometric configurations, followed by an analysis of the options available for the implementation of a high resolution low coherence interferometric imaging system. Chapter 3 describes the implementation of a system for one-dimensional depth profile measurements of semitransparent multi-layered targets. A preliminary experimental set-up for one-dimensional depth ranging is discussed alongside the associated signal processing schemes.

Chapter 4 deals with a novel path modulation technique, the Newton rings sampling function, and presents supporting theoretical background and experimental results obtained in its application to the imaging of various objects including human *in vivo* retina. The extension of methods described in Chapter 3 to surface profiling of objects, eye distance measurements and retinal imaging is discussed in Chapter 5, where several imaging modes are presented and analysed. Chapter 6 deals with the practical implementation of an optical coherence tomograph (OCT) incorporating all the major findings of previous chapters and Chapter 7 concludes this work by looking at the advantages, disadvantages and overall importance of the OCT method and OCT instrument.

Data on ocular physical parameters as well as some information on several LabView programs developed to assist in generating and displaying the images is presented in the appendices.

1.2 Low coherence interferometry

The aim of the research presented in this thesis is to provide a novel way of carrying out high-resolution surface profile and depth measurements and follow it up with an extension to three-dimensional imaging of human retina. Central to this objective is the concept of low coherence interferometry, which ever since its use by Michelson in 1895 for the measurement of the international standard meter has found implementations in various forms within the wider, established framework of interferometric technologies in the fields of metrology, optical testing and optical ranging.

Light sources with a 'broad' spectrum (20 nm bandwidth or more) exhibit a set of properties known as 'low coherence' and are a key component of low coherence interferometry systems.

Generally a low coherence source provides the input to an interferometer whose arms are matched within a controllable optical path difference (OPD) allowing the measurement of distance with sub-micron accuracy by observing at the interferometer output a well-defined peak in the interference signal.

Having originated from a light source and travelled to a detector along two different paths, the reference arm and the measurement arm, two wave packets emitted at the same time will only interfere if the optical path delay introduced between the two arms is less than the coherence length of the source, which could be of the order of a few microns.

For a number of applications and particularly for distance or displacement measurements, low coherence represents an advance on the more traditional coherent interferometers, which in general introduce a 2π phase ambiguity in the output reading. In low coherence interferometry the ambiguity is reduced to zero by detecting the point where the path imbalance between the arms is zero or approaching zero. It is at this unique point that the centroid of the interferometer transfer function, i.e. the measurable maximum of the phenomenon of interference between the two beams, can be found.

The detector readout as a function of the scanned path length resembles a fringe pattern modulated by the coherence profile of the source, peaking at the zero path imbalance point. Micron resolution path length measurements are possible through the controlled adjustment of the optical path imbalance between interfering beams, which results in a measurable variation of fringe visibility over the coherence range. With an

operating range in principle limited only by the path modulation procedure, this feature makes low coherence interferometry and the techniques which have it at its core, such as low coherence reflectometry, surface profilometry and optical coherence tomography particularly well suited for high resolution absolute distance measurements.

Although interferometric sensors offer extremely high resolution (periodic phase variations corresponding to a path variation of 10^{-14} m have been reported [1]), their development as general-purpose displacement sensors and their employment in distance measurement applications is relatively recent. The problems to be overcome in field applications are usually related to the difficulty of achieving a stable relative alignment of external and internal components. These obstacles have partly been overcome with sensor interferometers composed entirely from optical fibres [2]. The concern regarding geometrical instability is removed in this way but the fibre itself introduces a set of variable optical parameters, which are discussed in Chapter 2.

Optical fibre interferometers offer several advantageous features compared with more conventional techniques when used in ranging systems. They operate in a non-contact manner, are very sensitive and the probing radiation can be easily directed towards the measured object. Collimating light through single-mode fibres also offers the advantage of generating a spatially coherent beam, which is often essential for imaging applications.

Interferometric optical ranging sensors employing partially coherent, or 'white light' sources, have been regarded for several years as valuable tools for reflectometry and profilometry applications that require high resolution. Low coherence reflectometry (LCR) is one such method offering high sensitivity and high resolution. It is used for investigating depth reflection profiles primarily of optical targets and is based on coherence matching light returned by a target with reference light.

Recent advances in optical communications systems require the identification, localisation and quantification of optical fibre defects and reflection characterisation in fiberoptic systems. This can be achieved using a variant of LCR, usually termed optical coherence domain reflectometry (OCDR) [3],[4].

A decisive factor in establishing the viability of OCDR for this range of applications is a parameter called 'two event resolution' which shows how close two reflection sites can be in order to be resolved as individual reflections. With the two event resolution given by the coherence in the region of 10-50 microns and relatively insensitive to parasitic reflections, OCDR represents an important advance on older, established techniques such as narrow pulse optical time domain reflectometry and

optical frequency domain reflectometry which can discriminate only down to a few centimetres.

The application of LCR to one-dimensional profile measurements in fibre-optic and integrated optic structures [5] was swiftly followed by a number of low coherence surface profiling techniques [6],[7],[8] in which full images of two-dimensional target profiles were constructed one point at a time by raster scanning the collimated investigation beam across the object plane and coherence matching the returned light with the reference beam.

Optical coherence tomography is an extension to three dimensions of the depth discrimination properties of LCI and LCR. The coherence-related depth discrimination of optical coherence tomography allows the acquisition of a sequence of coherence slice images from a three dimensional specimen which in their ensemble constitute tomographic volume data for the specimen.

All coherence tomography techniques rely on low coherence interferometry to obtain depth information. Low coherence interferometry and optical coherence tomography have both found applications in medicine, mainly in ophthalmoscopy. However, the range of anatomical structures suitable for OCT investigations is continuously being extended, with recent reports detailing the application of OCT to skin [9] and the gastrointestinal tract [10].

1.3 Measurement of the surface profile of industrial objects. Non-contact surface profiling techniques

The field of industrial object surface profiling is a very wide area of research. The traditional need of optical component manufacturers for characterising the quality of smooth surfaces and the growing interest in quantifying surface roughness and tolerances in a non-contact fashion by the wide-ranging needs of the larger industry have prompted a plethora of various techniques to be proposed, which has led to the development of a number of powerful optical and non-optical instruments for surface characterisation. Suitability for each particular case is determined by the profiler's range, resolution (lateral and vertical), size and the ability of the instrument to supply information about the nature of the surface under investigation.

Powerful techniques such as heterodyne interferometry, capable of phase detection with accuracy better than $\lambda/10000$, largely dominate resolution-demanding applications. Although in the application to the profiling of surfaces beam diffraction is the limiting factor, phase unwrapping, heterodyne interferometry and multiple

wavelength interferometry capable of vertical resolutions in the nanometer to angstrom regime [11],[12],[13] have been demonstrated.

Surface profiling is generally undertaken with a view to provide a three dimensional dataset; the surface roughness, as a statistical interpretation of the dataset, is intimately related to the profile. If there are significant variations of surface roughness across the surface, statistical averages may need to be taken over smaller, more localised areas. The precision of the surface roughness measurement is linked to the lateral and longitudinal profiling resolution. However, the surface roughness value can be determined locally without a full 3-D dataset. In systems employing a reference surface, if the determination of the surface shape of the test object is not required, the reference surface is no longer the limiting factor. The errors it introduces can be removed with computer algorithms and averaging, thus enabling sub-angstrom surface roughness measurement even with a much rougher reference surface [14].

The measurement of an object's surface is generally carried out by defining a surface grid and measuring the surface height at each grid position (pixel), a procedure known as point measurement profiling. In interferometric systems of this type point by point information is gathered by scanning the measurement point over the surface and comparing the distance for each location to a reference distance. Pixels on the object surface are delineated by the focus of the investigation beam whose size has important implications on the achievable resolution, as shown below.

1.3.1 Diffraction limits for lateral and longitudinal resolution

Diffraction theory gives the irradiance profile produced by a beam passing through a circular aperture. For an aperture radius a the irradiance profile at a point P subtending an angle θ with respect to the optic axis is given by [15]:

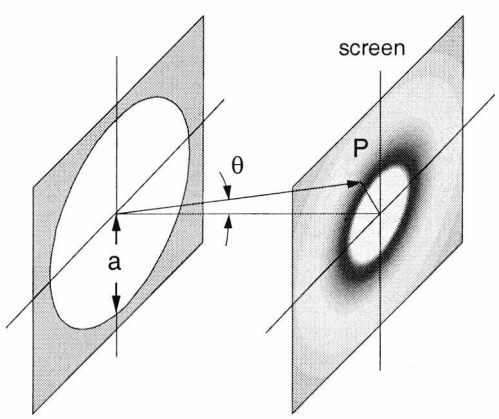

Figure 1.1 Diffraction at a circular aperture

$$I(\theta) = I(0)\left[\frac{2J_1(ka\sin\theta)}{ka\sin\theta}\right]^2 \tag{1-1}$$

where I(0) is the intensity on the optic axis, J_1 is the first order Bessel function of the first kind and k is the wave number. The pattern consists of a number of concentric disks (known as Airy disks) separated by dark annular regions. The central Airy disk is often referred to as the point spread function of an imaging system. For two adjacent points, each producing its own pattern, the minimum resolvable separation is usually taken to be the one defined by Lord Rayleigh's criterion, i.e. the points are said to be just resolved when the centre of one Airy disk falls on the first minimum of the Airy pattern of the other point. A limit Δl_{min} is defined to be the radius of the central Airy disk and corresponds to the value of the product $(ka\sin\theta)$ which results in the first zero of J_1, as can be seen from equation (1-1). In most imaging systems the diffracting aperture is the exit aperture of a lens which is situated at a distance from the screen equal to its focal length, f. The following formula gives the resolution Δl_{min} as a function of wavelength λ, focal length and aperture diameter D:

$$\Delta l_{min} = 1.22\frac{f\lambda}{D} \tag{1-2}$$

The value of Δl_{min} represents the minimum spot size of a beam focused on a test surface. A wavefront reflected by the illuminated area carries information about a multitude of points, some of which are lying at the extremities of this spot and are separated by Δl_{min}. The lateral imaging uncertainty range δx (Figure 1.2) can therefore be thought of as Δl_{min}.

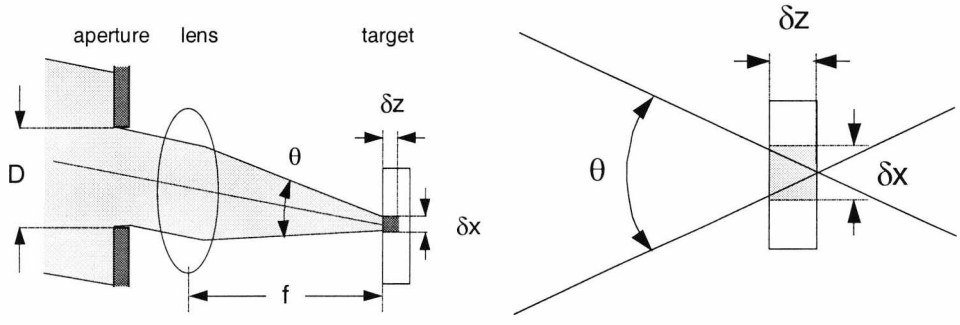

Figure 1.2 Illustration of the parameters defining the uncertainty voxel

In the case of rough surfaces, statistical height variations leading to a depth uncertainty δz can be significant over the lateral range δx. From the geometry in Figure 1.2, δz can be defined as:

$$\delta z = \frac{\delta x}{\sin\theta} \tag{1-3}$$

which indicates that for rough surfaces the longitudinal resolution limit is severely limited by diffraction (for example, for sin θ = 0.2 the longitudinal resolution is 5 times worse than the lateral resolution). This limitation should be taken into account when assessing the applicability of point measurement profilers to rough surface measurements.

1.3.2 Confocality

Confocality represents a tight focus on the object surface coupled with the rejection, before the detector, of light not passing through the confocal correspondent of the illuminated point on the object surface. The size of the confocal aperture determines the degree of confocality of the image, with small confocal apertures giving rise to sharper confocal images.

The first requirement of a confocal system is achieved in practice when the light is focused within a small axial range centred on the focal plane of the optics. The depth discrimination capability, characterised by the degree of confocality, is proportional to the steepness of the axial light gradient in the target volume corresponding to size of the focused beam spot (voxel).

Further discrimination is obtained by inserting an aperture in the plane of the image, and rejecting all light incident outside the aperture area. Only light scattered back from the focus on the illuminated object voxel arrives at the detector, which results in additional improvement of contrast.

When confocal systems are used in surface profile scanning configurations, the nature of the scan can influence the quality of images obtained. The optical contrast for the case of one-dimensional scanning (slit scanning) is lower than for the case of 2-dimensional scanning (beam scanning) [16].

The unaccommodated human eye has a relatively small aperture (3-4 mm) (see Appendix A.1). This places a limit on the achievable lateral resolution since the minimum spot size on the retina, s_{min}, is given by equation (1-4):

$$s_{min} = \frac{1.22\,\lambda\,f}{D_{max}} \tag{1-4}$$

where λ is the wavelength of light in the investigation beam, f is the focal distance of the crystalline lens and D_{max} is the maximum aperture of the pupil (Figure 1.2). The beam spot size (and therefore the voxel) will therefore have a lower limit imposed by

the anatomy of the eye. Usually this limit is of the order of 10 to 12 μm, depending on the particularities of each eye, with aberrations playing an important role.

Confocal eye imaging systems possess a number of advantages such as the exclusion of light returned from multiply scattering structures (hard exudates), media opacities, minimisation of the influence of light scattered by structures outside the focused object plane.

1.3.3 The scanning microscope

The main feature of the scanning microscope, presented in Figure 1.3, is the restriction of the object field to only one point at a time, in contrast with conventional optical microscopes, which offer an image of the entire object field [17]. A scanning mechanism is essential since in order to produce the entire image point by point the investigation spot must be scanned relative to the target.

A diffraction-limited spot from a laser beam is provided by the objective lens and when the beam is fixed and the object is scanned it ensures space invariant imaging (the resolution and contrast are identical across the entire field of view), usually at the cost of a much longer acquisition time. Space invariance is not achieved, however, if the beam spot is scanned and the object fixed.

A third option is the scan of the collimating lens, with both the optical system and the object fixed. This technique has been found [18] to result in an effectively on-axis imaging system and, if larger objects are examined, it is easier to implement since it does not require rastering the specimen relative to the optical system.

An increase in longitudinal resolution and a simultaneous increase in the depth

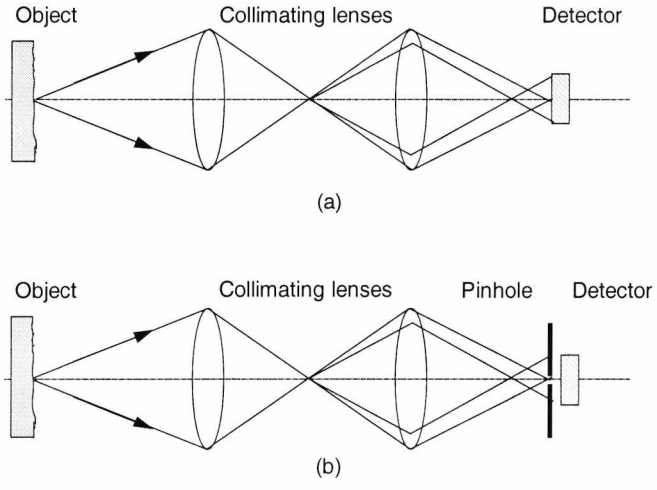

Figure 1.3 Schematic diagram of a scanning microscope (top: conventional, bottom: confocal)

discrimination capability of the conventional scanning microscope can be obtained by minimising the size of the detector [17], thus rendering the system confocal as shown in Figure 1.3 bottom. This can be achieved by placing a small pinhole in front of the detector. The concept of confocality, which is central to high resolution scanning microscopy, is discussed in greater detail in paragraph 1.3.2.

Interferometric sensors, widely used in optical metrology and absolute distance measurements, offer some of the highest resolutions of all non-contact surface profilers. A diagram with some of the most common focused beam interferometric profilers is given in Figure 1.4. It shows three different ways in which the beam can be separated in the object and reference sub-components with interference observed at the recombination of light scattered by the object and light returned from the reference surface (usually a mirror).

The Michelson geometry, generally used for low magnifications, keeps to a minimum the errors induced by lens aberrations, thanks to its single objective. This is also the case of the Mirau interferometer, which provides slightly higher magnifications (up to 40X). The Linnik geometry uses two matched objectives and thus achieves reasonably high magnifications (100X and above). The collimators can be brought close to the test and reference surfaces thereby achieving a high numerical aperture, which gives it a high optical resolution.

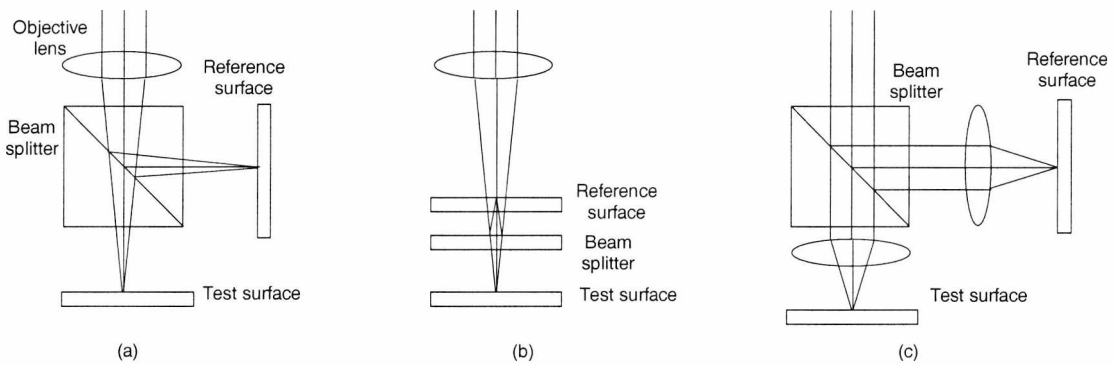

Figure 1.4 Geometry of three interferometric configurations used in surface profiling. (a) Michelson interferometer; (b) Mirau interferometer; (c) Linnik interferometer

The three bulk configurations in Figure 1.4 can easily be implemented with optical fibres acting as waveguides with the addition of a beam collimator at the fibre exit. Such systems have the advantage that light is collected back into the system through the fibre aperture, which provides an extremely effective rejection of non-confocal light (see [18]).

The focused beam profilers discussed above are ideally suited for operation with the classic point detector. However, their reliance on a tight beam focus on the object

surface can be a disadvantage when narrow holes are explored, due to the restricted entrance aperture of such holes, which, as explained below, places a constraint on the lateral resolution.

1.3.4 Non-scanning interferometric profilers

Recently introduced profiling systems, some already commercialised, are making more and more use of solid state imaging devices such as CCD cameras in order to provide aperture-independent resolution and, by illuminating the whole surface of the object of interest at once, eliminate the need for surface scanning and result in the production of an image in a parallel fashion.

An example of this kind is a coherence system, which uses two-dimensional CCD array detection in a telecentric telescope arrangement [19], [20]. The configuration is shown in Figure 1.5. It consists of a Michelson interferometer with the optics adapted such that the object is illuminated by a parallel, expanded beam rather than a focused beam. Each pixel on the CCD array can be ray-traced to a corresponding pixel on the object. A telecentric stop allowing only object light scattered in the backward direction at 180° to reach the detector ensures minimisation of stray light detected by a camera pixel from pixels on the object surface other than its ray-traced object pixel.

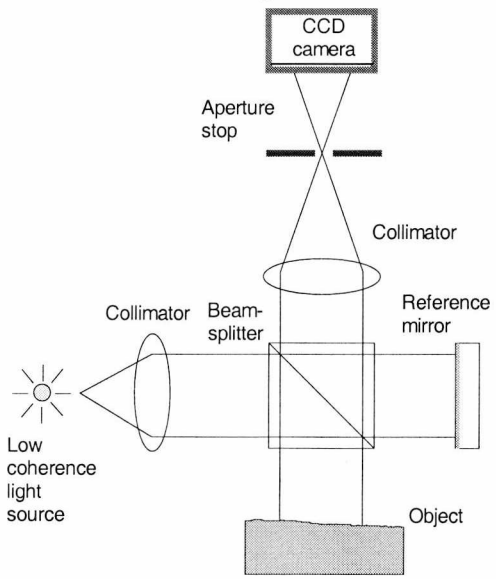

Figure 1.5 Schematic diagram of the coherence radar for the measurement of 3-D shapes

A complete 3-D profile of the surface can be generated by scanning the reference mirror in depth and measuring the maximum coherence signal as a function of depth for each pixel. The surface is subsequently recovered from the array of coherence maxima.

The technique has the important advantage that it is not aperture limited and therefore its theoretical resolution is dictated only by the roughness of the surface explored. Simultaneous imaging of the entire pixel grid comes at the cost of a lower sensitivity and dynamic range although advances in solid state imaging may well lead to CCD devices with dynamic ranges comparable to single point photodetectors.

1.4 Imaging for ophthalmologic diagnosis

The practice of measuring and recording the topology of various structures in the *in vivo* human eye is relatively recent. Historically most imaging methods have been restricted to visual observation of the inside of the eye through adapted instruments such as the fundus camera. The living human eye (Figure 1.6), transparent under most circumstances, is optically accessible and well suited for investigations relying on the detection of a light beam launched through the pupil and subsequently backscattered from intra-ocular tissue.

In vivo imaging of the retinal anatomy has found many applications in modern clinical ophthalmology. As opposed to conventional techniques which provide only a visual and rather subjective characterisation of the areas under investigation, recent imaging technologies offer planar or volumetric data in the form of an absolute determination of feature size and intra-ocular distances with a high degree of repeatability. These techniques also allow the subsequent production of conventional

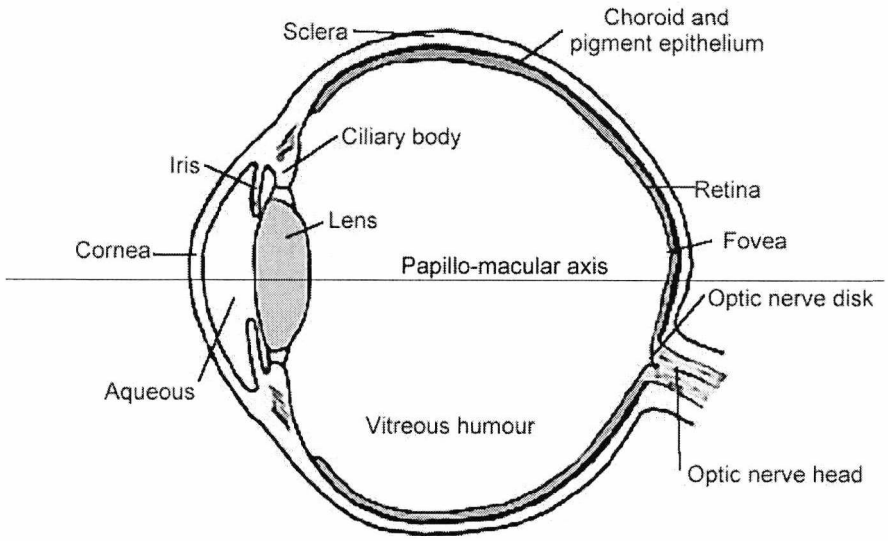

Figure 1.6 Schematic diagram of the human eye

images on the basis of stored data.

Topological information regarding the eye fundus offered by *in vivo* imaging and measurement techniques is usually one or two-dimensional and until recently was restricted to cross-sectional planes perpendicular to the papillo-macular axis (Figure 1.7).

A major part of research in ophthalmic imaging is now being directed towards the acquisition of longitudinal depth information parallel to the papillo-macular axis and the production of two-dimensional tomographic images of structures lying behind superficial tissue at the back of the eye. Most such structures are identifiable through

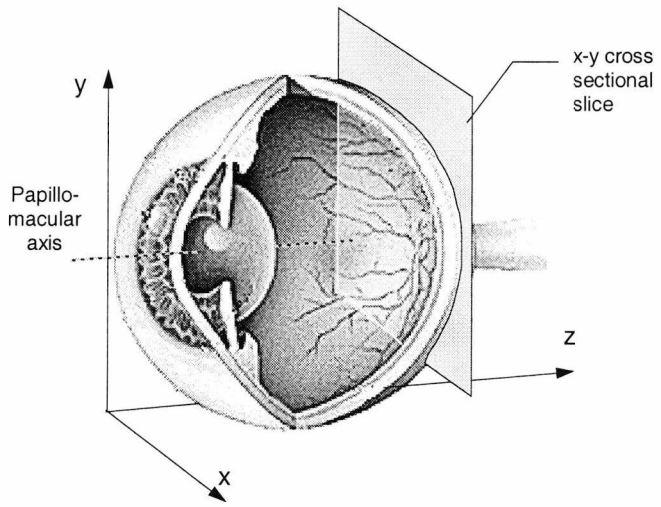

Figure 1.7 Illustration of the geometry of ophthalmic tomographic images. A Cartesian system of co-ordinates is chosen such that the papillo-macular axis is parallel to the z axis, with x-y cross sectional slices perpendicular to the papillo-macular axis.

comparison with available histological data. However, a further aim is the subsequent correlation of data with images generated with more conventional equipment in use by ophthalmologists such as fundus cameras, slit cameras and scanning laser ophthalmoscopes.

The production of high resolution *in vivo* topographic (surface) and tomographic (depth) images of the eye allows inspection of internal tissue structure for evidence of abnormal anatomical features or pathological changes. The driving force behind research for new, more powerful methods in ophthalmic imaging originates in the conclusion of recent studies regarding the pathology of retinal structures responsible for vision. These studies indicate that a large number of ocular conditions can be diagnosed and assessed from variations in the thickness and shape of retinal tissue and other eye fundus structures. In the initial stages of disease progression the changes can be as small as a few tens of microns and therefore high-resolution quantifiable depth information is required for their detection. Storage of such information in a database, with the possibility of repeatable comparisons between datasets over time, enables ophthalmologists to monitor the changes and detect a trend in variations, therefore enhancing the possibility of early diagnosis.

1.4.1 Abnormal structural changes in the eye fundus

The human eye retina is constituted from a series of layers interrupted in the region of the optic nerve head, or the optic disk, by the retinal ganglion cell axons, which, densely packed, converge at the optic disk and exit the optic nerve. The presence of a high number of axons in such a small, localised area leads to an increased sensitivity of vision to local physical deformations. The absence of retinal neurons in this area leads to the formation of a vision blind spot.

1.4.1.1 Glaucoma

In glaucoma, a visual field loss condition characterised by raised intra-ocular pressure, changes in the appearance of the optic nerve head are detectable. It is often the case that there is a delay of up to a few years between morphological optic nerve changes and the onset of detectable visual field changes in patients with glaucoma, time when a large proportion of the optic nerve fibres can be lost to the disease. The early detection of morphological changes to the optic disk and nerve fibre layer, whose thinning can also be a good indicator of the risk of developing glaucoma, would mean that therapy could be initiated sooner. At the same time, systematic and accurate optic nerve imaging can help clinicians follow progressive disk damage and detect advanced glaucoma damage.

Recent studies [21] suggest there may be other morphological changes that can potentially aid early detection of glaucoma. One hypothesis advanced has been that optic nerve head damage from raised intra-ocular pressure is related to the structure of *lamina cribrosa*, a structure located under the neuroretinal rim [16]. However, the imaging in depth of the *lamina cribrosa* is difficult with conventional methods in most patients since the neuroretinal rim has a very high scattering coefficient.

1.4.1.2 Macular degeneration

The macula is the sensitive region of the retina that provides fine-detail vision. In many elderly patients the tissues of the macula are subject to a degenerative ageing and thinning process leading to the appearance of macular holes of various thickness, from minimal thickness progressively to full thickness holes resulting in decreased visual acuity and impeded vision. Patients lose the ability to look straight ahead and distinguish fine detail or read small print, and must eventually rely on peripheral vision. Structures such as choroidal neo-vascular membranes, which are often formed before vision loss, can alert the ophthalmologist to the condition if they are detected early [22].

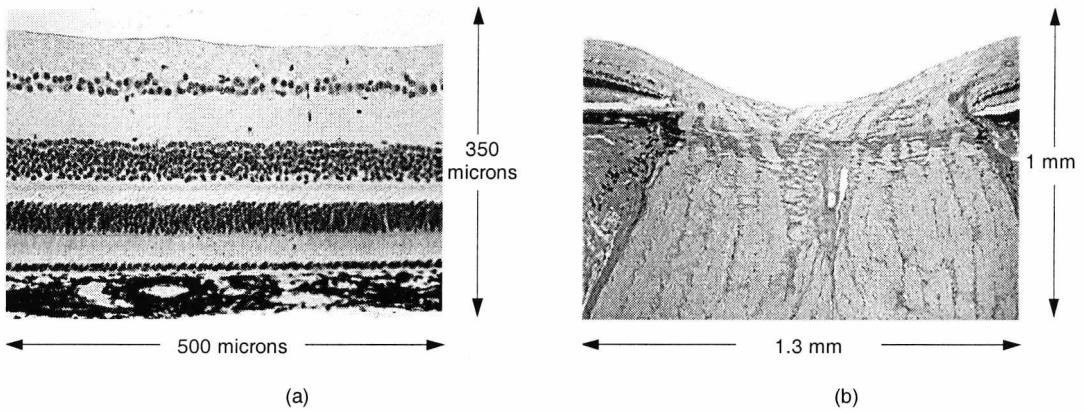

Figure 1.8

(a) Histological sample of a human retinal nerve fibre layer, RNFL. From top to bottom: Inner Limiting Membrane, Nerve Fibre Layer, Ganglion Cell Layer, Inner Plexiform Layer, Inner Nuclear Layer, Outer Plexiform Layer, Outer Nuclear Layer, Inner and Outer Segments of Photoreceptors, Retinal Pigment Epithelium, Choroid. Courtesy of the New York Eye and Ear Histology Database

(b) Histological sample of the optic disk of a human retina. Courtesy of the New York Eye and Ear Histology Database

Any high resolution automated imaging of retinal tomography that does not depend on operator judgement and skill and could offer a high degree of repeatability is therefore extremely useful for both the diagnosis and scale assessment of macular diseases. With the decision on surgical intervention depending critically on the discrimination of full-thickness holes from other stages of development, such quantitative topographical information on the scale of the disease is an important aid to the surgeon.

1.4.1.3 Detachment of neuroretinal rim

Another condition which can be detected by inspection of the tissue is the detachment of the neuroretinal rim, defined by an elevation of the retina and the accumulation of fluid from the vitreous between the neurosensory retina and the retinal pigment epithelium which further contributes to retinal detachment [23].

1.4.1.4 Diabetic retinopathy

Diabetic retinopathy is an ocular disease characterised by damaged and abnormally growing blood vessels within the retina. It most often occurs in patients with long-term diabetes. There are two types of diabetic retinopathy: non-proliferative

and proliferative. Non-proliferate diabetic retinopathy is characterised by damaged retinal vessels leaking fluid (fat and protein particles), which become deposited in patches known as retinal exudates. The retinal blood vessels may also bleed, causing tiny haemorrhages. Proliferative diabetic retinopathy is characterised by new abnormal blood vessel growth extending over the surface of the retina and occasionally invading the vitreous of the eye. These new abnormal blood vessels frequently break, causing vitreous bleeding. Untreated, this can cause a significant decrease in vision. [24]. Such morphological changes together with high backscattering caused by the presence of hard exudates make this abnormal condition identifiable on the inspection of tomographic data.

1.4.2 Conventional eye imaging techniques

The importance of imaging microstructures on the eye fundus for ophthalmologic diagnosis has directed research both towards the adaptation of conventional surface imaging techniques to the ocular geometry and towards the extension of the capabilities of existing ophthalmologic instruments, frequently resulting in some degree of hybridisation taking place.

Computer tomography and magnetic resonance imaging are established imaging methods that can be applied to various parts of the human body. Computer tomography relies on the irradiation of the body with X rays while magnetic resonance imaging is based on mapping the signal emitted by nuclei of hydrogen and free water placed in a strong, static magnetic field when excited by electromagnetic radiation. In both cases the detected signal is digitised, stored and converted into an image. Magnetic resonance imaging does not use ionising radiation but is counter-indicated for use on patients with foreign metallic bodies or cardiac pacemakers. An intra-ocular imaging resolution of 300 microns has been reported with MRI using special surface receiver coils [25]. Both techniques are used for evaluation of macroscopic lesions and normal and abnormal anatomical features and are well suited for the imaging of larger parts of the eye not requiring high resolution.

Ultrasound has been used in ophthalmic imaging for a few decades. It is marginally invasive in the sense that the ultrasonographic transducer requires contact with the eye via a layer of gel since ultrasonic waves cannot easily propagate in air. Ultrasound scans of the eye can be divided into the brightness mode category (B-mode) which produces images similar to the cross-sectional slices in scanning ophthalmoscopes and amplitude mode category (A-mode), similar to longitudinal slices. The resolution of standard clinical ultrasonography is limited by the

wavelength of sound in ocular tissue to about 150 μm [26]. Nevertheless, A and B scan ultrasonography are used routinely in clinical practice to image and differentiate orbital disease and intra-ocular anatomy (Humphrey USA, OTI Canada).

A more recent contact technique is high frequency ultrasound biomicroscopy, capable of 20 μm resolution. It uses high-frequency ultrasound in the range of 40 MHz to 100 MHz to image subsurface structures in the living eye with high resolution. At this frequency, the sound waves can penetrate 4 to 5 mm and image the entire anterior segment [27],[28].

Colour Doppler ultrasound imaging is a technology that measures the blood flow in the vessels of the human fundus by detecting changes in the frequency of sound reflected from the blood flow. Doppler information is then superimposed in colour over the two-dimensional grey-scale ultrasound image. The technique has the ability to localise small vessels in the eye, orbit and optic nerve and see flow in the retinal vessels but cannot accurately assess vessel diameters [26].

One of the oldest optical instruments used for intra-ocular visualisation is the ophthalmoscope, which allows an observer to look into the patient's eye and see an image of the retina to be examined. Its optics (Figure 1.9) consist of a collimating lens which in conjunction with a deflecting element (mirror or prism) directs the beam from a light source to the back of the patient's eye, illuminating the retina. The illuminated spot of light on the retina of the observed eye comes to a focal spot on the retina of the observer's eye. A choice of corrective lenses, usually mounted on a turret, assist in the formation of a clear image in each case.

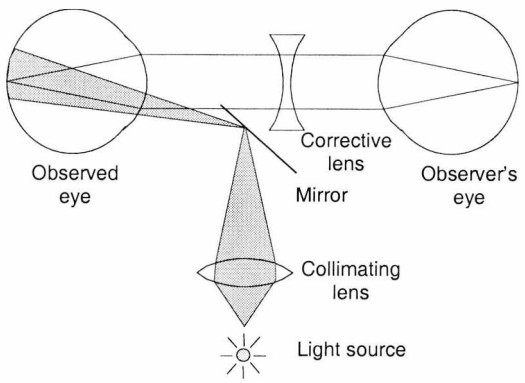

Figure 1.9 Schematic diagram of the optics of an ophthalmoscope

Slit lamp biomicroscopy is an investigative procedure consisting of the visual inspection of the internal eye by means of an adapted microscope. Adjustable optics allows the operator to bring into focus various parts of the eye such as cornea, lens, and retina. A conventional image is produced in real-time, which contains information on the reflectivity but not on the topography of the observed tissue, is generated by scanning an illumination slit across the target.

Fundus cameras and slit cameras are optical instruments designed around the same principle as the ophthalmoscope to offer an overall image in the visible spectrum

for direct observation. It is worth mentioning that fundus photography had been the principal investigation method for the eye fundus before the advent of scanning ophthalmoscopes [29],[30].

3-D topography has been demonstrated with measurements of the nerve fibre layer contour by computerised videographic image analysis and stereophotogrammetry. A drawback of these procedures is that homogeneous loss, i.e. loss caused by the sagging of the entire fundus is not readily measurable, since these changes do not reflect in the relative topography of the fundus seen in isolation.

In addition to these imaging instruments used currently in clinical practice, low coherence interferometers concerned with one-dimensional measurements of intra-ocular distances such as the eye length and the distance between cornea, crystalline lens and retina have been proposed for use in optometry evaluations, mainly prior to cataract surgery, in order to predict the converging power of an artificial lens which would produce emmetropia [26], [31].

A new commercially available device for retinal thickness measurement is the nerve fibre analyser [32]. It consists of a scanning laser ophthalmoscope with an integrated laser polarimeter and is designed to measure the change in the state of polarisation of laser light passing through the birefringent retinal fibre layer. The thickness of the layer is then obtained by applying a correction coefficient to the measurement obtained. However, other retinal structures cannot be measured and birefringence compensation for cornea and lens is a complex requirement with several variable factors to be taken into account for each patient.

1.4.3 The Scanning Laser Ophthalmoscope

The scanning laser ophthalmoscope (SLO), and particularly its newer confocal version (cSLO) provide the natural choice of architecture to accommodate a coherence tomography system, as it will be shown later in Chapter 5.

The design of the apparatus is very similar to that of the scanning microscope, with some adaptations for intra-ocular observations. A diagram of the cSLO is shown in Figure 1.10. The scan of a focused laser beam over successive points on the eye fundus produces images of those points (pixels) which line up to form a frame whose dimensions and refresh rate are given by the ratio of horizontal and vertical scan frequencies.

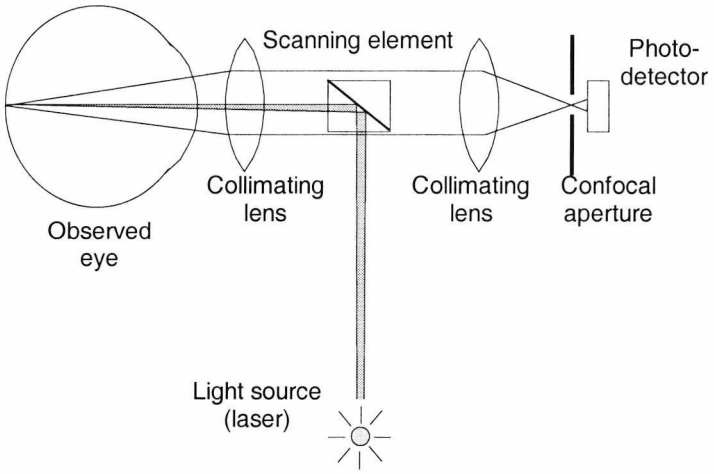

Figure 1.10 Schematic diagram of the confocal scanning laser ophthalmoscope

The instrument can operate in two scan modes: two-dimensional spot scanning or one-dimensional slit scanning (see 2.2.1). in each case the detection system must be made to scan in synchronicity to the laser illumination such that the illumination and the detection are directed at the same point on the fundus [16].The area defined on the retina by the scanning process can be visualised through a fundus camera whose operation is compatible with the SLO.

The images obtained by the cSLO contain information about a thin volume slice all other light being rejected by the confocal detection. These images differ from conventional monochromatic images in that the contrast in a confocal image arises mainly from differences in the reflection and refraction coefficients between what appear as dark and bright areas, rather than by differences in absorption of the incident light [33].

The limited penetration depth of the optical probe light in highly scattering tissue is due to the exponential attenuation with the number of scattering events encountered [34],[35]. The backscatter signal from sub-retinal structures may also appear dim as a consequence of high absorption or reflection at hard exudates or a retinal blood vessel. Some eye conditions such as vitreous haemorrhage, lens opacities, vitreous clouding also contribute to an increase in the attenuation of light returned by the fundus.

A commercially available device, the Heidelberg laser tomographic scanner, has been used to measure the depth of full thickness macular holes in a group of patients [36]. For holes of 144 μm average depth the authors report a figure of 30 microns depth resolution.

The confocal SLO, which has been available commercially for several years, represents a useful tool for obtaining repeatable and detailed images of the in vivo

retina, is limited by ocular aberrations and maximum entrance pupil diameter of the eye to 200 to 300 μm [16].

1.5 Optical coherence tomography

Optical coherence tomography (OCT) is a non-contact, non-invasive optical imaging technique using non-ionising low coherence radiation. It is capable of high resolution imaging of various surface types, notably biological tissues. For low scattering tissue it is also capable of probing subsurface tissue layers. Depending on specimen thickness, light from the investigation beam can be detected either in transmission or reflection.

The basic scheme of a Michelson interferometer-based reflection OCT is shown in Figure 1.11. The term "tomography" describes the process of acquiring slice images of the internal structure of three-dimensional objects and consists of two steps: data acquisition followed by image display. In optical coherence tomography image slices are obtained through the detection of interference between mutually coherent light returned from the object and from the reference path (see Chapter 2).

OCT of the eye can produce either *en face* cross sectional images at various depths or two-dimensional slice images of reflectivity vs. depth in eye structures. The part of the eye to be imaged is placed in the object (see Figure 1.11) and is illuminated by a light beam focused to a narrow spot, which can be accurately positioned at a chosen location on the eye fundus through a scanning mechanism. During the scanning process, which is a combination of beam scanning (lateral) and reference

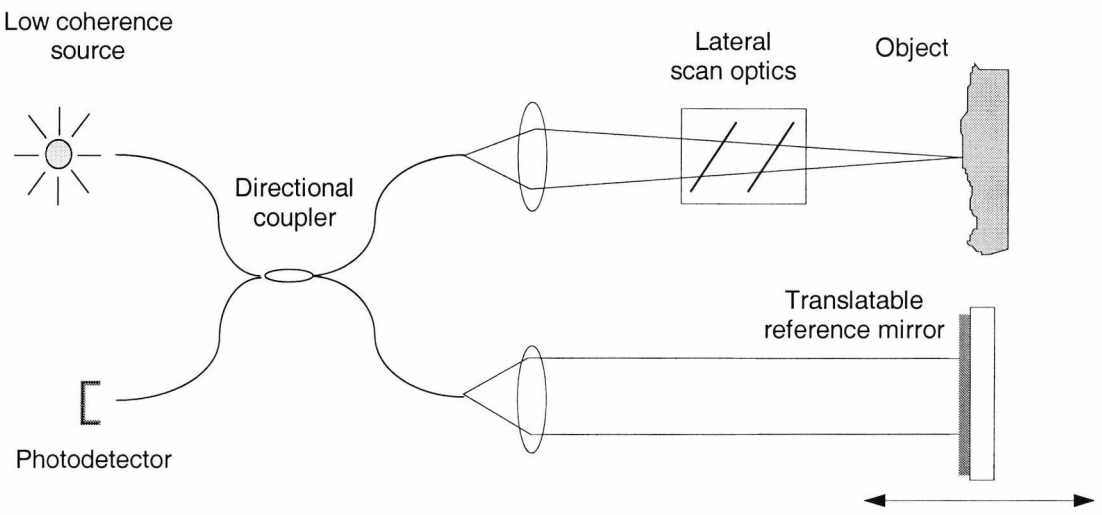

Figure 1.11 Basic scheme of an Optical Coherence Tomograph (OCT)

path length scanning (longitudinal), the investigation beam is displaced across the region of interest.

Depth information is obtained by the detection of an interferometric signal at each beam position. Cross-sectional tomograms of ocular tissue are produced in this way for each longitudinal position in a chosen range. From the stack of images the height at each pixel position can be subsequently calculated and displayed on the monitor as part of a topographical map.

The design of the optical interface of ocular OCT systems is similar to that of the confocal scanning ophthalmoscopes (cSLO). The use of optical fibre leads in OCT systems, with light wavefronts emerging from a 5 micron diameter single mode fibre, is advantageous due to the high confocality (light exits fibre end, is reflected and then re-coupled into the fibre) and high degree of spatial coherence of light exiting such a narrow aperture.

When applied to eye investigations, OCT brings a marked improvement on the longitudinal resolution of the cSLO. Its theoretical axial resolution is given by the source coherence length and is not limited by the pupil aperture and aberrations (which is the case of the cSLO, between 200 microns and 300 microns) or scattering in the media. The diffraction limited lateral resolution of OCT systems is in the region of 10-15 microns at the retina based on the Gullstrand schematic eye (see paragraph 1.3.1 and Appendix).

Improvements in superluminescent diode technology within the last few years have made near infrared devices available with coherence lengths of less than 20 μm and capable of coupling powers of a few mW in single mode fibre (see 2.1.3.3), which allow the detection of a sufficiently large amount of fundus scattered light for detection and processing. Due to the reduced eye sensitivity to infrared light, the OCT examination is well tolerated by patients. However, biological tissue OCT imaging has the disadvantage of being sensitive primarily to directly reflected probe light, which exponentially attenuates as it propagates through the retina, and therefore its penetration depth is limited to a few mm in highly scattering tissue [37].

As well as being established as a clinically viable and powerful biomedical optical imaging technology, OCT has found several applications in industrial metrology: optical characterisation of materials, microscopy in scattering media, femtosecond transillumination tomography, measurement of surface profiles [38].

2. Low coherence surface profilometry

2.1 Coherence reflectometry

2.1.1 Interference of two monochromatic light waves

The irradiance, or the intensity of a lightwave is the time average of the amount of energy that crosses in unit time a unit area perpendicular to the direction of energy flow. In order to derive the irradiance of a light wave at a point in space one should begin by considering the space-time dependence of the electric field at that point.

The electric field intensity vector $\vec{E}$ of a monochromatic wave at a point of co-ordinates $\vec{r}$ and t is given by:

$$\vec{E}(\vec{r},t)=\mathrm{Re}\left[\vec{A}(\vec{r})\ e^{-i\omega t}+\vec{A}^{*}(\vec{r})\ e^{i\omega t}\right] \tag{2-1}$$

After raising both sides in the above to the power of two, we have:

$$\left[\vec{E}(\vec{r},t)\right]^{2}=\mathrm{Re}\left[\left[\vec{A}(\vec{r})\right]^{2}\ e^{-2i\omega t}+\left[\vec{A}^{*}(\vec{r})\right]^{2}\ e^{2i\omega t}+2\left[\vec{A}(\vec{r})\right]\left[\vec{A}^{*}(\vec{r})\right]\right] \tag{2-2}$$

Taking the time average of the magnitude of the electric field squared over a large interval compared with the period $T = 2\pi/\omega$ (which for visible light is of the order of 10^{14} Hz), the experimentally detectable wave intensity (irradiance) I is readily obtained as:

$$I=\left\langle\vec{E}^{2}\right\rangle=\frac{1}{2}\vec{A}\cdot\vec{A}^{*}=\frac{1}{2}\left[\left|A_{x}\right|^{2}+\left|A_{y}\right|^{2}+\left|A_{z}\right|^{2}\right] \tag{2-3}$$

where the components A_x, A_y and A_z of the complex amplitude $\vec{A}$ have been introduced. These coefficients carry information about the state of polarisation of the wave and depend on the position $\vec{r}$ as follows:

$$A_{x}=a_{1}(\vec{r})e^{i\left(\vec{k}\cdot\vec{r}-\delta_{1}\right)} \tag{2-4}$$

$$A_{y}=a_{2}(\vec{r})e^{i\left(\vec{k}\cdot\vec{r}-\delta_{2}\right)} \tag{2-5}$$

$$A_{z}=a_{3}(\vec{r})e^{i\left(\vec{k}\cdot\vec{r}-\delta_{3}\right)} \tag{2-6}$$

where $a_j(\vec{r})$ (j = 1,2,3) are real functions, $\vec{k}$ is the propagation vector and δ_j are phase constants which specify the state of polarisation.

$$\langle \vec{E}^2 \rangle = \frac{1}{2}\left[|A_x|^2 + |A_y|^2 + |A_z|^2\right] = \frac{1}{2}\left(a_1^2 + a_2^2 + a_3^2\right) \tag{2-7}$$

When two monochromatic waves of electric field vectors $\vec{E}_1$ and $\vec{E}_2$ are superposed at a point in space, the total electric field at this point will be the vector addition of the two fields:

$$\vec{E} = \vec{E}_1 + \vec{E}_2 \tag{2-8}$$

$$\langle \vec{E} \rangle^2 = \langle \vec{E}_1 \rangle^2 + \langle \vec{E}_2 \rangle^2 + 2\langle \vec{E}_1 \cdot \vec{E}_2 \rangle \tag{2-9}$$

In this last equation $\langle \vec{E}_1 \rangle^2$ and $\langle \vec{E}_2 \rangle^2$ can be identified with I_1 and I_2, the respective intensities of the two beams taken separately. The $2\langle \vec{E}_1 \cdot \vec{E}_2 \rangle$ term arises as a consequence of wave interaction and is an interference specific term. If $\vec{A}$ and $\vec{B}$ are the amplitudes of the two waves, we have

$$2\langle \vec{E}_1 \cdot \vec{E}_2 \rangle = \frac{1}{2}\left(\vec{A} \cdot \vec{B}^* + \vec{A}^* \cdot \vec{B}\right) \tag{2-10}$$

and the total intensity at the detector is

$$I = I_1 + I_2 + a_1 b_1 \cos(\Delta\varphi_1) + a_2 b_2 \cos(\Delta\varphi_2) + a_3 b_3 \cos(\Delta\varphi_3) \tag{2-11}$$

where a_j, b_j are the respective components of $\vec{A}$ and $\vec{B}$ while $\Delta\varphi_1$, $\Delta\varphi_2$ and $\Delta\varphi_3$ represent the phase differences introduced between the corresponding Cartesian rectangular components of the two waves, arising from a combination of differences of path length and initial phase angle. For a particular set of conditions, these phase differences may be the same and have a non-zero value, i.e.

$$\Delta\varphi_1 = \Delta\varphi_2 = \Delta\varphi_3 = \Delta\varphi \tag{2-12}$$

provided that the two interfering waves have the same frequency (otherwise the phase difference would be rapidly varying with time and would average to zero).

It follows that:

$$I = I_1 + I_2 + \left(a_1 b_1 + a_2 b_2 + a_3 b_3\right)\cos(\Delta\varphi) \tag{2-13}$$

In the particular case of two waves propagating along the z-direction, linearly polarised with their $\vec{E}$ vectors in the x-direction,

$$a_2 = a_3 = b_2 = b_3 = 0 \tag{2-14}$$

and the intensity I becomes

$$I = (I_1 + I_2) + \left(2\sqrt{I_1 I_2}\cos(\Delta\varphi)\right) \tag{2-15}$$

Equation (2-15) also holds for unpolarised light waves propagating in the same direction since a beam of unpolarised light can be represented as a superposition of two mutually incoherent beams linearly polarised at right angles to each other. On the other hand, two linearly polarised beams in directions perpendicular to each other do not interfere, as it is seen from (2-13) if the condition $a_2 = b_1 = a_3 = b_3 = 0$ is set.

As the fringe pattern quality can vary due to a number of parameters such as polarisation (see 2.1.4), a useful measure of the fringe pattern quality is the fringe

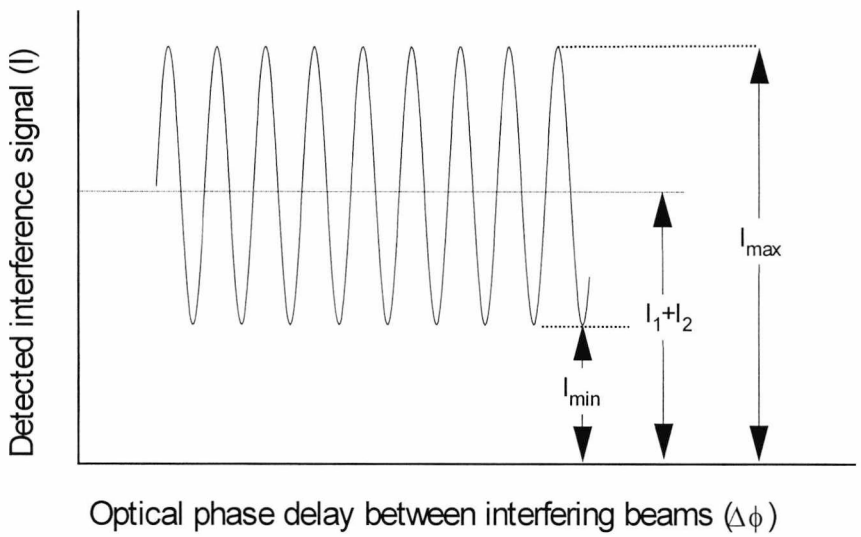

Figure 2.1. Illustration of the transfer function in a monochromatic light interferometer with constant visibility fringes

visibility at a particular point in the interference pattern with neighbouring maximum and minimum intensity values I_{max} and I_{min}. The fringe visibility V (Figure 2.1) is defined as:

$$V = \frac{I_{max} - I_{min}}{I_{max} + I_{min}} \tag{2-16}$$

Maximum visibility corresponds to $I_{min} = 0$.

2.1.2 Interference of partially coherent light beams

Light waves, it could be argued, are never strictly monochromatic. Light emission by atoms in thermal motion, located in sources of finite size, results in damped wave trains of limited temporal and spatial extent, with uncorrelated phases.

In examining the properties of interference between non-monochromatic light waves, it is useful to relate to the concepts of coherence time and coherence length. These quantities are seen as measures of the amount of correlation between light disturbances, due to one source or more, at two instants in time or points in space, in a particular medium. In the simpler case of light waves originating from only one source, the term 'source coherence length' relates to the spatial interval along the direction of propagation of light, over which, at any given time, the optical excitation from the source exhibits a finite degree of correlation, arbitrarily defined.

For a polychromatic light source, with components covering a wavelength range $\Delta\lambda$ around a central wavelength $\bar{\lambda}$ (it should be mentioned here that in practice this is frequently the case of a near-monochromatic source, with $\Delta\lambda << \bar{\lambda}$), the interference signal resulting from the combination of waves from the light source is strongly influenced in shape and extent by a source parameter $\gamma_{11}(\tau)$ called the normalised source auto-correlation (or self coherence) function. This is a function of the time delay τ between the arrival at the detector of two beams originating from the source, which can be expressed in terms of the optical phase delay between beams, $\Delta\varphi$, and the velocity of light in vacuum, c, as:

$$\tau = \frac{\Delta\varphi}{\bar{k} \cdot c} \tag{2-17}$$

and

$$\Delta\varphi = \bar{k}\,\Delta L \tag{2-18}$$

where $\bar{k}$ is the wavenumber associated with the central wavelength $\bar{\lambda}$ and ΔL is the optical path difference (OPD) between interfering beams.

The interferometer transfer function can now be written:

$$I(\tau) = (I_1 + I_2) + \left(2\sqrt{I_1 I_2}\,|\gamma_{11}(\tau)|\cos\Delta\varphi(\tau)\right) \tag{2-19}$$

In a similar manner with the previously discussed case of monochromatic interference, the total intensity is again the sum of two terms: the constant term, equal to the addition of individual beam intensities I_1+I_2, and the interference term which

now depends on the auto-correlation function $\gamma_{11}(\tau)$ as well as on $\Delta\varphi$, as shown in Figure 2.2.

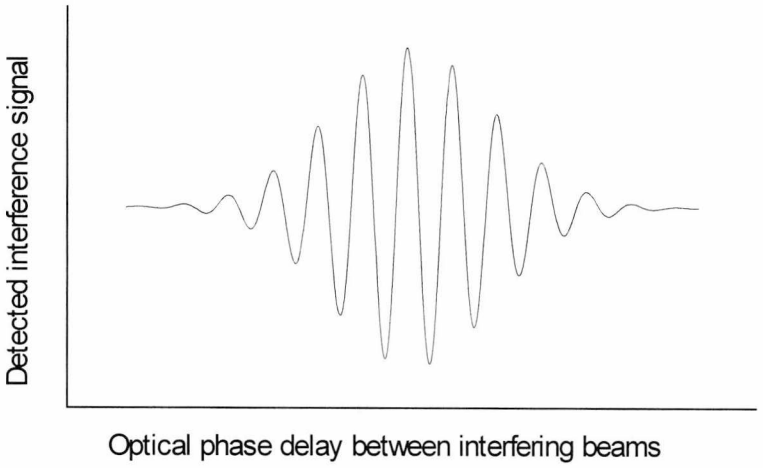

Figure 2.2 Auto-correlation of low coherence light

The visibility value from equation (2-16) can be written in terms of I_1 and I_2 as follows:

$$V=\frac{2\sqrt{I_1 I_2}}{I_1+I_2}\left|\gamma_{11}(\tau)\right| \tag{2-20}$$

and if the average intensity I_m is defined as:

$$I_m=\frac{I_{max}+I_{min}}{2}=I_1+I_2 \tag{2-21}$$

then the expression of the transfer function in terms of visibility is:

$$I=I_m\left(1+V\cos(\Delta\varphi)\right) \tag{2-22}$$

Since the case of polychromatic light beam interference represents a departure from the particular case of monochromatic light beam interference, it is somewhat to be expected that the auto-correlation function would be related to the source spectrum. The relationship between them is known as the Wiener-Khintchine theorem, which states that the autocorrelation function is obtained by taking the Fourier transform of the power spectrum of the source [39].

The shape of the auto-correlation function is determined by the statistical properties of the light source, governed by its homogeneous and inhomogeneous radiation broadening mechanisms [40].

When the same transition centre frequency ν_0 and the same resonance lineshape is common to radiating atoms the term 'homogeneous' is used to describe the broadening process. Homogeneous broadening is characterised by a finite interaction lifetime of emitting or absorbing atoms, which determines a spread in frequencies $\Delta\nu$. The spectral profile is a Lorentzian spectral distribution function, given by:

$$P_{Lorentz}(\nu)=\frac{2\Delta\nu}{\pi\left[4(\nu-\nu_0)^2+\Delta\nu^2\right]} \tag{2-23}$$

In the case of inhomogeneous broadening atoms have slightly different transition frequencies. The spectral distribution of spontaneous emission reflects the spread in the individual transition frequencies due to phenomena such as Doppler broadening, temperature effects, inhomogeneous DC magnetic fields, source substrate imperfections [41]. Significant temperature-related Doppler broadening effects induce a linewidth temperature dependence which is an important spectral output modifier [42]. In this case, the spectral profile is Gaussian, with the normalised power spectral density function expressed as follows [43],[44]:

$$P_{Gauss}(\nu)=\frac{2\sqrt{\ln 2}}{\sqrt{\pi}\,\Delta\nu}\exp\left[-\left(2\sqrt{\ln 2}\frac{(\nu-\nu_0)}{\Delta\nu}\right)^2\right] \tag{2-24}$$

In both equations above $\Delta\nu$ is the full width at half maximum frequency separation between points on the spectral power curve where $P_L(\nu)$ and $P_G(\nu)$ are down to half of their peak values and ν_0 is the frequency value where the power emitted is maximum.

According to the Wiener-Khintchine theorem one can obtain the normalised autocorrelation function by taking the inverse Fourier transform of the normalised power spectra in (2-23) and (2-24), i.e.

$$\gamma_{Lorentz11}(\Delta L)=\exp\left(-\frac{|\Delta L|}{L_c}\right) \tag{2-25}$$

$$\gamma_{Gauss11}(\Delta L)=\exp\left[-\frac{\pi}{2}\left(\frac{\Delta L}{L_c}\right)^2\right] \tag{2-26}$$

The Lorentzian and Gaussian functions representing the source auto-correlation in the two situations described above both peak at $\Delta L = 0$. This property is at the heart of low coherence sensing since the detection of a peak in the interference pattern removes the ambiguity of the transfer function of a coherent interferometer.

2.1.2.1 Visibility and resolution

Equations (2-16) and (2-20) relate visibility to the intensities of the interfering beams and to the auto-correlation function describing source properties. They show that the visibility function is governed by the coherence properties of source and by the quality of interferometer. In the case of an ideal monochromatic wave with matched polarisation states, the visibility value depends solely on the ratio I_1/I_2 (equation (2-20)). The shape of this dependence can be seen in Figure 2.3.

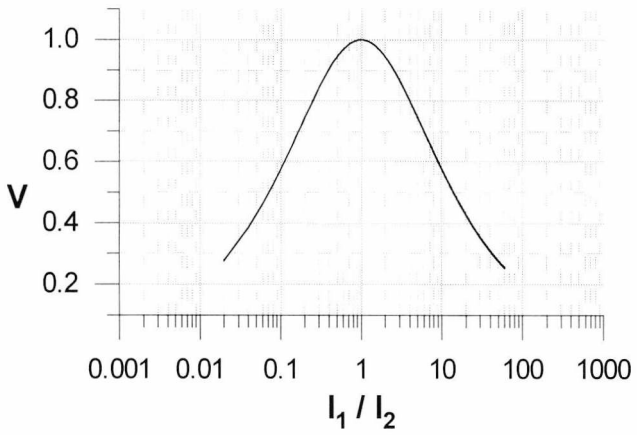

Figure 2.3 Visibility dependence on the ratio between the intensities of interfering beams with matched polarisation states

However, in the majority of experimental situations, in the absence of polarisation control, even when the interfering beams are coherence matched (i.e. the auto-correlation function is close to its peak value), the visibility is less than 1 due to the unmatched polarisation states of recombining beams (see paragraph 2.1.4).

The theoretical resolution Δz, based on the detection of the rectified fringe pattern generated in an interferometer operating with a source of a Gaussian spectral profile is the *full width at half maximum* (FWHM) of a reflection generated signal, expressed as a optical path difference (see Figure 2.4). This definition is somewhat similar to that of the point spread function discussed in 1.3.1 except that the rectified fringe pattern does not have zeros. Most authors in the field of LCI agree on the definition of axial resolution as the FWHM value of the rectified fringe pattern.

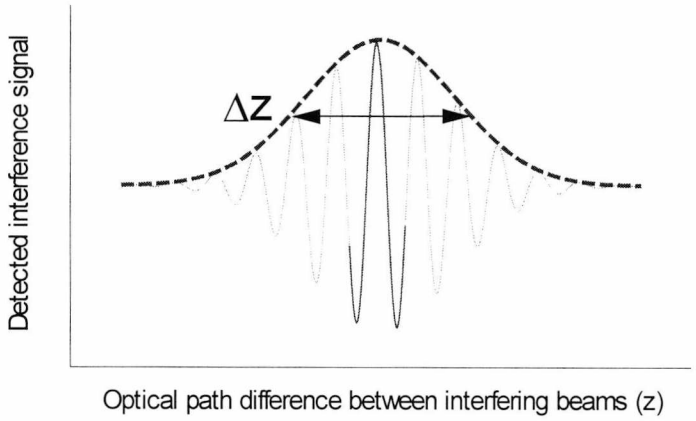

Figure 2.4. Resolution given by the rectified envelope of a coherence signal (Δz) compared to the resolution given by phase measurement of the central fringe.

Equation (2-26) shows that the spectral properties of the source are contributing factors to the width of the interference signal. The following relationship links the group velocity of the light wave v_g and the FWHM of the light spectrum $\Delta\nu$ with the theoretical resolution value Δz [45]:

$$\Delta z = \frac{v_g}{2\Delta\nu} \tag{2-27}$$

The relationship between the source coherence length L_{coh}, the central wavelength λ_0 and the FWHM of the wavelength spectrum $\Delta\lambda$ results as:

$$L_{coh} = (\ln 2)\frac{2\lambda_0^{\,2}}{\pi\Delta\lambda} \tag{2-28}$$

e.g. for a superluminescent diode operating at 800 nm with a FWHM of 20 nm, the coherence length is about 14 μm. This value, which has been reported in literature [10], gives an estimate of the depth resolution commonly achieved with currently available sources.

An important feature of this transfer function is that the maximum of the coherence envelope corresponds to an exactly zero path imbalance between the interfering beams, therefore high resolution measurements on the micron scale or better are possible on the basis of precise centroid determination using computer post-processing techniques. As well as centroid determination, which will be discussed later, it is possible to perform a computer phase measurement around the position of zero optical path imbalance, which results in a further resolution improvement.

2.1.3 Fibre configurations for low coherence interferometry

As discussed in the previous chapter, interferometric non-contact distance measurements to a target are carried out by measuring the length of the air path traversed by the sensing light beam. The necessity of having an air path requires the investigating beam to travel outside the existing fibre leads and be directed via collimating optics onto the target, which implies that any interferometric configuration for surface profiling must necessarily be hybrid (bulk + fibre).

With the rapid advance of optical fibre technology in recent years the implementation of partially or totally fiberised interferometric sensors can be done in a cost-effective way, many components now being commonly available. The use of optical fibres facilitates compact experimental arrangements and fibres can access, due to their nature, geometrically difficult spaces.

2.1.3.1 Fibre Michelson interferometer. Basic operation

One of the simplest interferometer geometries is the fibre Michelson interferometer, shown in Figure 2.5, a dual-beam, amplitude splitting configuration. Light emitted from a source travels to a directional coupler (which, like bulk beam-

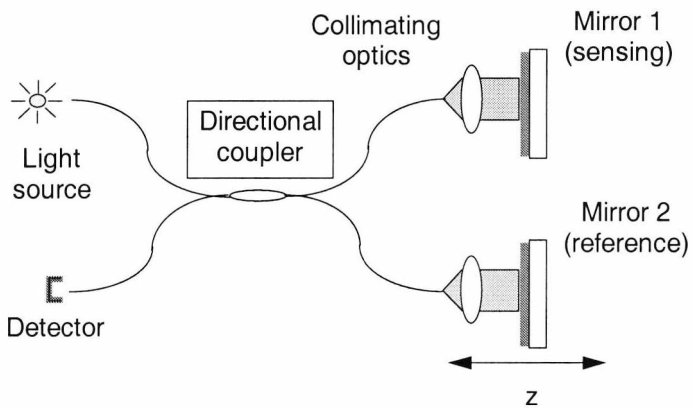

Figure 2.5 Fibre Michelson interferometer

splitters, can be manufactured at precise transmission ratios) where it is divided into two waves (sensing and reference). These waves exit the coupler arms, are collimated on the target surface and reference mirror respectively and reflected back into the coupler after which they recombine and arrive at the detector. Alternatively, a fibre-air interface obtainable by cleaving the end of the reference fibre returns about 4% of the optical power into the system without the need for a reference mirror.

The Michelson interferometer transfer function has the reference mirror position z as argument and is obtainable from (2-19):

$$I(z) = (I_1 + I_2) + \left(2\sqrt{I_1 I_2}\,|\gamma_{11}(z)|\cos(2\bar{k}z)\right) \qquad (2\text{-}29)$$

It is notable that a double optical phase shift per unit length of mirror translation distance arises as a consequence of the double pass of light through the fibre arms, hence the factor of 2 in the cosine argument in (2-29).

However, the potentially large amount of light fed back into the optical source due to the complementary output (non-existent in an all-transmitting Mach-Zehnder configuration, described below) may cause unwanted source instability. Furthermore, noise associated with reflections off the end of the fibre (maximum for right angle cleaves) may place some constraints on measurement range, limiting it to less than the distance between fibre ends and mirrors.

Interferometric investigations of transparent targets are also carried out in transmission rather than reflection (light propagates through the object). In this case it is the forward scattered light that is made to interfere with a reference beam. A suitable configuration where transmitted object probe light can be re-coupled into the system is the Mach-Zehnder interferometer, which also reduces feedback effects (see 2.1.3.3). A diagram of a hybrid fibre and bulk Mach-Zehnder is shown in Figure 2.6.

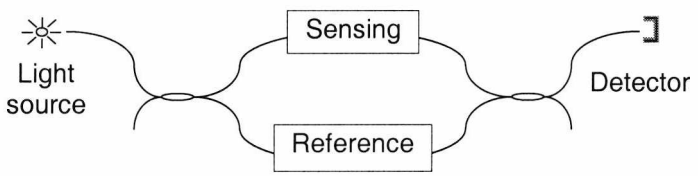

Figure 2.6 Schematic diagram of a fibre Mach Zehnder interferometer

The fibre Mach-Zehnder configuration consists of two directional couplers. The outputs from the first coupler are linked to the inputs of the second, thus forming two separate propagation paths, a reference and a sensing arm.

2.1.3.2 Path modulation

A key requirement of signal processing in low coherence systems is that the optical path (or, equivalently, phase) difference between the interfering beams is subject to a modulation, subsequently used to generate a carrier. This is usually achieved by modulating the optical length of the reference beam path. A notable exception are those situations when due to the nature of the lateral scan procedure the object arm length is subject to an inherent periodic fluctuation. The particular case of the 'Newton-rings sampling function technique', which conforms to this principle, is treated in Chapter 4.

Path length modulation can be carried out in two possible ways, either at higher frequencies by use of electrostrictive or electro-optic modulation or at lower frequencies through physical movement of reflective elements over a distance at least equal to the coherence length of the light source by means of a DC or stepper motor translation stage.

In the electrostrictive case, it is usual that a reflective optical element (mirror) is mounted on a piezoelectric element, which vibrates in the kHz range with amplitudes up to a few microns.

Another widely used technique, namely stretching the optical fibre with a piezoelectric cylinder, could be potentially superior in terms of achieving higher frequencies and greater amplitudes. Fibre stretching has a double effect: it changes the local refractive index of the strained fibre and at the same time it varies its length. Typical values for the modulation sensitivity in the range of 10...100 mrad / V·turn are commonly achieved with such devices. One issue of concern is, however, the large amount of dispersion introduced by refractive index variations, which requires dynamic compensation.

The electro-optic modulation procedure is carried out by introducing an rf modulated electro-optic crystal such as $LiNbO_3$ in the reference path of the interferometer. The optical path through the crystal varies according to the electric field modulation. This is a fast technique which allows modulation speeds of the order of tens of MHz. However, electro-optic crystal materials have rather high refractive indices (in excess of 2), which cause significant dispersion. To attenuate this dispersive effect, the introduction of a crystal in the reference arm needs to be balanced by the introduction of a similar crystal in the object arm. Bulk electro-optic elements also increase the difficulty of adjusting beam collimation. However, recently developed integrated fibre elements may alleviate this difficulty.

Finally, by scanning the axial position of the reference mirror at a constant velocity v, a Doppler shift is introduced in the reference beam light, of central wavelength λ for as long as the mirror is within the coherence interval. This results in the observation of the interferometer transfer function in the photodiode current output; the frequency f of the Doppler frequency shift is given by:

$$f = \frac{2\pi}{\lambda} v \qquad (2\text{-}30)$$

This Doppler modulation is discussed in more detail in Chapter 3.

2.1.3.3 Light sources, detectors and optical fibres

Light sources

The recent availability of high power pigtailed superluminescent diodes (SLD) [46] has made possible the injection, in single-mode optical fibre, of light with coherence length in the range 10-50 μm and with power levels in the miliwatt range.

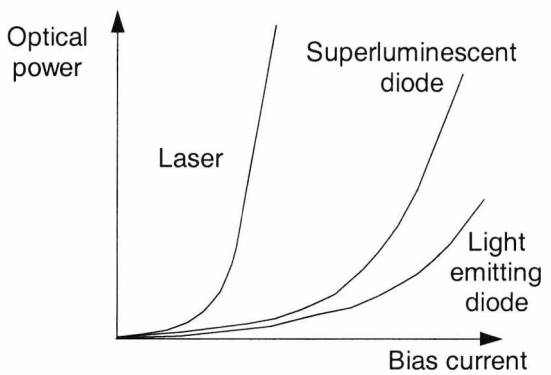

Figure 2.7. Comparison between bias current, power curves for three types of light sources

The comparatively high power exhibited by SLDs against more traditional low coherence such as laser diodes below threshold or edge-emitting diodes is generated through a mixture of stimulated and spontaneous emission. Their characteristic low coherence is due to the cavity face design which is aimed at the reduction of the level of photon recirculation inside the cavity and therefore of the coherent radiation output. Cavity gain, however, is maintained high so that stimulated emission occurs even for a single pass of light through the active medium and therefore the radiation power is comparable to single mode laser diodes above threshold. The typical power dependence on bias current for these three categories of devices is shown in Figure 2.7.

Although standard superluminescent diodes exhibit a near-Gaussian spectral profile, they tend not to reproduce the output characteristics of light-emitting diodes in that their spectrum is less smooth and exhibits what is known as spectral ripple. This partially distorting modulation of the spectrum is due to residual effects of the internal cavity caused by its basic operation as a stimulated emission source. Spectral ripple is enhanced by the backreflection of light from system optics into the cavity, such as in the case of pigtailed devices where fibre paths act as a channel guiding light back into the cavity. This effect can be minimised if fibre end reflections are reduced and / or light from reflecting elements is not allowed to re-trace a reciprocal path into the source.

Detectors

Silicon (Si) based photodiodes span a wavelength range of between 190 and 1100 μm. Available in standard packages, they are generally small, lightweight and inexpensive. Measurable optical power ranges from a few pW to 1 mW. They are characterised by very good sensitivity and ambient noise performance, stability, fast risetimes (10 ps), excellent linearity and dynamic range. For pW level applications, an operational amplifier circuit is commonly used to produce the required signal gain. Avalanche photodiodes providing internal gain currents up to a factor of 100 are used in low light level applications where noise is an issue of concern.

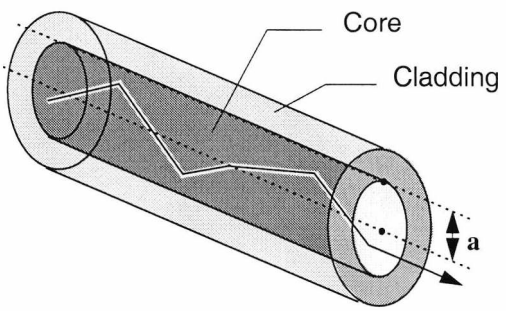

Figure 2.8. Ray propagating through a section of optical fibre

Fibres

Optical fibres are a well known transparent medium extensively used as light waveguides and / or as sensing elements in many applications. They provide easy access to geometrically difficult areas which is advantageous if the size of the instrument should be kept to a minimum.

Light propagates through an optical fibre (Figure 2.8) by undergoing successive internal reflections at the core-cladding interface. For a central core refractive index n_1, and outer cladding index n_2, the numerical aperture of the fibre, NA, is given by:

$$NA = n_1 \sqrt{2\left(1 - \frac{n_2}{n_1}\right)} \tag{2-31}$$

The normalised frequency of fibre, V, is defined as:

$$V = \frac{2\pi a}{\lambda} \sqrt{n_1^2 - n_2^2} \tag{2-32}$$

where a = core radius and λ is the wavelength of light. For values $V < 2.405$ it can be shown that only the lowest order mode (called LP_{01}) can propagate through the fibre and in this case the fibre is called single mode. The number of modes increases with V for values above 2.405, case in which the fibre is said to be multimode. Path length

differences between simultaneously propagating modes in multimode fibres substantially decrease the interference signal contrast, therefore single-mode fibre is almost always used for fibre optic interferometry.

The birefringent nature of single-mode fibres is due to the LP_{01} mode consisting of two independent orthogonal linearly polarised modes with different propagation constants [2]. This has important consequences in fibre interferometry as the division of light into modes randomly affects the state of polarisation of interfering beams as shown in paragraph 2.1.4 below.

The utilisation of optical fibres in an interferometer brings a number of advantages compared with the bulk implementation. The resulting set-up is more compact, alignment is easier, and when the power is divided into more than two beams, the optical fibre tree configuration is superior to multiple beamsplitter arrangements. In addition, the coupling of the light back into the small aperture of the fibre ensures a good confocality between the target and detector planes, which otherwise would necessitate extra bulk optic components.

However, the fiberisation has some intrinsic disadvantages such as difficulty with polarisation control, sensitivity to vibration, Rayleigh noise and lower efficiency in transferring light to and from bulk optic devices in the set-up.

2.1.4 Polarisation in fibre optic interferometric configurations

It was shown in Equation (2-13) that the complexity of the transfer function of a single mode fibre interferometer is greater when polarisation mismatch between the interfering waves is an issue.

Optical fibres and components used in interferometers often exhibit low birefringence, which results in random fluctuations in the state of polarisation of the interfering beams. Polarisation is a very important aspect of the operation of fibre interferometers since polarisation-induced signal fading can bring the visibility of the interference signal to zero.

As mentioned in 2.1.3.3, all single mode fibres are characterised by a certain degree of birefringence (the LP_{01} mode consists of two independent orthogonal linearly polarised modes). Even in the ideal case of a fibre interferometer having polarisation insensitive components and optically isotropic fibres, into which light is launched from a linearly polarised source, light will propagate through the fibre along a fast and a slow axis, each with a different refractive index, sensitive to bending.

If the phase delay between axes results in the sensing arm behaving like a $\lambda/2$ phase plate, light can be launched along the fast or slow axis and emerges from the sensing and reference arms with aligned states of polarisation. In this case the interference visibility would be 1. If, however, light is launched at 45° to the fast or slow axis, light from the sensing arm emerges at 90° relative to light in the reference arm, which brings the visibility to zero. If the fast axis refractive index is varied by fibre bending, maximum visibility may again be obtained. Polarisation fading therefore occurs due to changes in birefringence and also due to changes in the input state of polarisation of the interferometer.

To overcome polarisation-induced effects, avoid polarisation fading and maintain optimum fringe visibility, polarisation-maintaining fibre could be used, with light injected into one of the eigenmodes. This may increase the complexity throughout the entire sensor system, as it requires control of the polarisation state of light at the injection into fibre such that it is matched to fibre birefringence [47].

A common method to achieve the alignment of polarisation states is the use of a three-ring polarisation controller. Fibres in both arms of an interferometer are wrapped around a device which allows the introduction of a controlled amount of torsional stress (and therefore, birefringence) in fibre, allowing maximisation of the interference signal in a fibre set-up.

2.1.5 Dispersion

Dispersion is the variation of the refractive index of a particular medium with the wavelength of a light beam traversing the medium. Radiation at shorter wavelengths experiences a higher refractive index and travels the same geometrical length in a longer time interval than radiation at longer wavelengths.

Dispersion, together with any spectral changes suffered by the radiation on its path through the interferometric set-up (such as during propagation or at the anti-reflection coatings of bulk optics), has a significant effect on decreasing the resolution particularly in the case of systems employing low coherence light because it results in the broadening of the coherence profile (signature) of a reflected signal. This broadening is due to the fact that the time overlap of interfering radiation is extended as a result of dispersive action and therefore interference occurs between longer wavetrains.

Any optical element in one particular arm of an interferometer which does not have a corresponding element with an identical refractive index and of the same

length induces unbalanced dispersion. A common cause of unbalanced dispersion in a fibre interferometer is a length mismatch of fibres in the reference and object arms.

Moreover, in the dispersive case amplitude is no longer a reliable measure of reflectivity as any dispersion induced shape mismatch between the interfering wavepackets leads to a decrease of visibility in the interference signal [48], [49].

A study of the dispersion introduced in the system by a lithium niobate crystal is carried out in Chapter 5.

2.2 Scanning the target surface

The need for scanning the surface of the target in point measurement systems was discussed in Chapter 1. The process of surface scanning consists in pointing the investigation beam in turn at each (arbitrarily defined) pixel within an area of interest on the object surface. It is always easier to rotate a small mirror than to move the entire source together with collimating optics, the mirror being usually several orders of magnitude lighter and capable of being moved more quickly.

A surface scan is characterised by the geometrical scan limits, which essentially represent an outline of the area of interest on the object surface. A grid, or an algorithm for dividing this area into individual pixels, and a pixel scan order are usually employed

The scan limits are linked to the maximum available aperture of the system, which may be dictated by scan head geometry. The choice of pixel size depends on the size of the focused light beam, which determines the maximum lateral resolution.

2.2.1 Scanning procedures

The two most widely used scanning procedures are illustrated in Figure 2.9. In one-dimensional scanning, the beam is focused by using suitable cylindrical lenses or mirrors to a narrow slit which is deflected in only one direction, perpendicular to the slit. Fast scan rates are achievable without complex scan heads and therefore the procedure is extensively used in conventional ophthalmic instruments such as slit lamp biomicroscopes.

In the case of two-dimensional scanning, only a small spot, of roughly equal width and height, is illuminated at any instant. The beam is usually deflected in a raster fashion in two orthogonal directions (x and y, see Figure 2.9) perpendicular to the optic axis of the system. As this procedure consists of point-by-point scanning, a

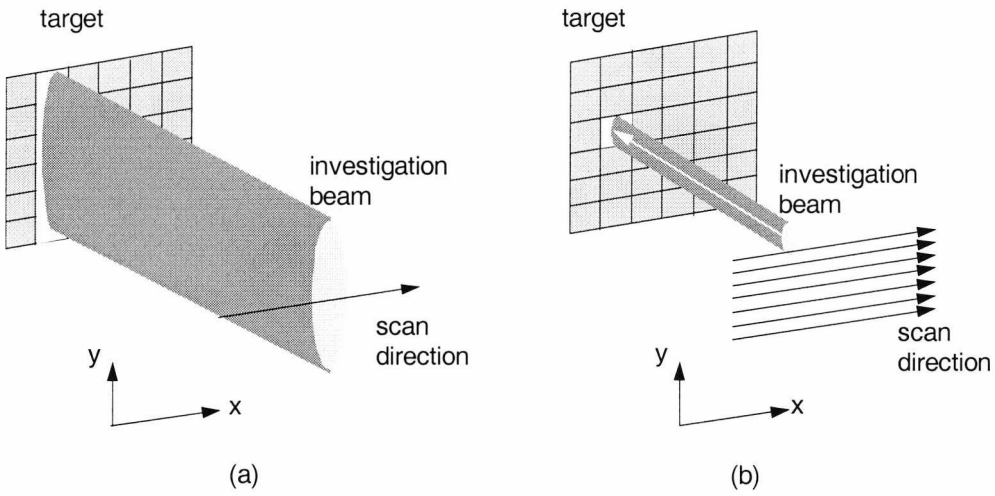

Figure 2.9 a) one-dimensional scanning; b) two-dimensional scanning

scan over successive points on the target results in an image composed of a rectangular array of pixels.

Such a procedure takes longer and places quite strict demands on the synchronisation of the x and y scans. Raster scanning can be unidirectional, case in which the x scan is a high frequency line and the y scan is incrementing an x line at a time or continuously, or bi-directional, avoiding flyback, when the x scan is a triangular waveform with the Y scan driven by a sawtooth or both scanners driven by triangular waveforms.

2.2.2 Scanning devices

Most scanning procedures associated with imaging are of an opto-mechanical nature and are reviewed in subsequent paragraphs. One of the few presenting an alternative to mechanical scanners employ acousto-optic devices.

In an acousto-optic scanning device, a travelling ultrasonic wave establishes a thick diffraction grating in an interaction medium, with grating spacing equal to the ultrasonic wavelength. The result is an angular scan, which can be converted to a linear scan by placing a lens at the exit of the acousto-optical element. The main advantage of such devices is the fast scan rates achievable (100 microseconds per line [50]). However, they are severely limited in dynamic range (the ratio between the total angular swing and the minimum separation between adjacent spots), a parameter that depends entirely on scanner properties (resolution values quoted in literature are around the value of 1000 spots per line [50]). They also exhibit a cylindrical lensing effect, which is due to the spread of acoustic frequencies across the acousto-optic element resulting in the diffraction of the optical beam at different angles.

2.2.2.1 Polygon mirrors

The facets of a polygonal body spinning around its vertical axis of symmetry constitute a polygon mirror (see Figure 2.10). Due to their unidirectional rotation these devices can provide relatively large speeds in comparison with their galvo-based counterparts (below) but in practice it is relatively difficult to control their beam positioning and beam alignment. When used in coherence systems, the curvature of the coherence plane due to path length differences between centre and extremities must be taken into account and the curvature of coherence data must be adjusted accordingly.

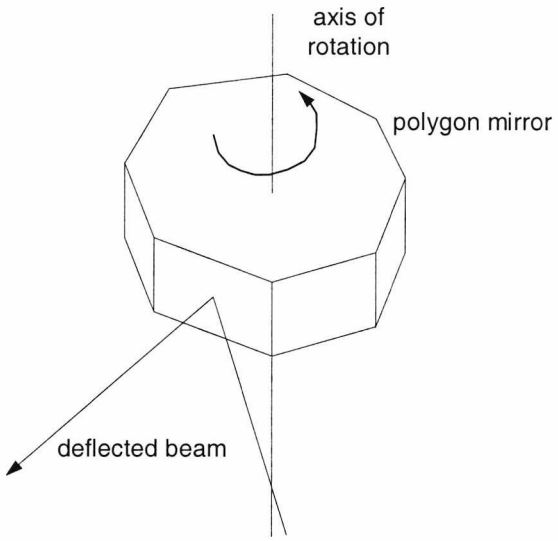

Figure 2.10 Polygon mirror

2.2.2.2 Resonant optical scanners

Mechanical resonance scanners are simple flexural or torsion bar oscillators designed to operate sinusoidally at a range of fixed frequencies (usually below 10 kHz), with adequate repeatability for video applications. To keep complexity and cost to a minimum, a position sensor to provide feedback for precise positioning is not commonly included. In order to obtain a scan at constant velocity linearisation through suitable electronic pixel clocking is required.

2.2.2.3 Galvanometer scanning mirrors

Galvanometer mirrors are essentially mirrors mounted on limited rotation rotary servo motors. These motors are specifically designed for providing a highly linear torque over a relatively large rotation angle (typically between 30 and 40 degrees mechanical). Galvanometer based optical scanners, with their high speed and good accuracy, dominate applications where these two requirements are central.

A scan head constituted by a pair of orthogonally placed galvanometer scanning mirrors can be used for deflecting optical beams in an X-Y manner and for controlled positioning of the beam on the target surface (see Figure 2.11), having been primarily developed for laser projection and vision applications. Each of the two mirrors in the scan head is designed to reflect the beam at a nominal incident angle of 45 degrees. The axis of rotation of the Y mirror is directly over the axis of rotation of the X mirror.

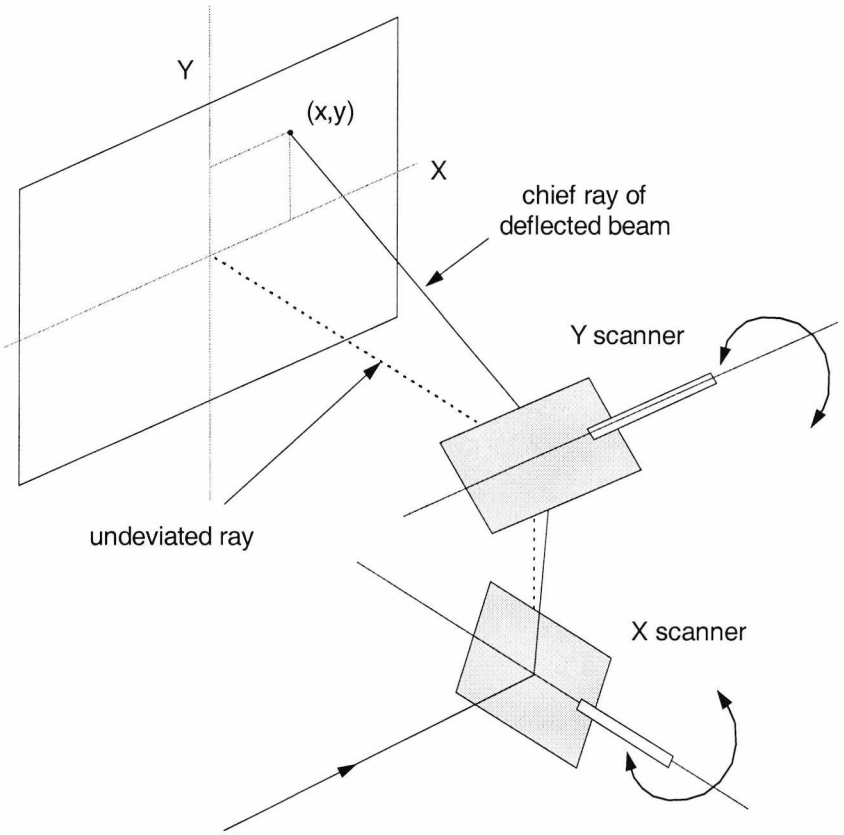

Figure 2.11 X-Y scanning mirror pair arrangement

In the choice of scan head three parameters play an important part: the optical resolution given by the size of the limiting aperture, the mechanical positioning accuracy and the scanner speed.

As the beam is reflected at each of the two mirrors, the various apertures restricting its diameter vary according to the scan angle. It is usually the case that the limiting aperture of a scanner system is given by the maximum beam diameter for a maximum 'near' deflection angle at the mirror of first incidence, as shown in Figure 2.12.

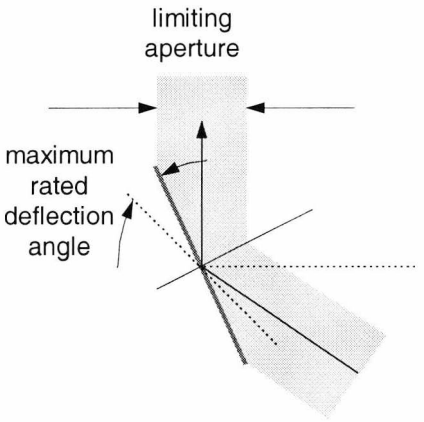

Figure 2.12 Limited aperture at shallow angle incidence

For the General Scanning GS XY 0507 scan head, the value of the limiting aperture is 5 mm. The accuracy in the angular position of the scan head at rest is ± 0.3% of the full field. For a scan of ± 20 degrees, the maximum error is ± 2 mrad in each axis. Mirror angles to mounting references are within ±10 mrad and within ± 6 mrad of each other although these values are not critical in the overall accuracy of an image.

The critical speed parameters for a raster type imaging procedure are the write and retrace line rates which give the minimum time interval during which the pixel line is scanned (write) and the minimum time between lines of pixels. These times are 5 ms and 2 ms respectively for the GS XY 0507 scan head.

Laser quality half wave flatness mirrors are an available option for mounting on the scanner pivots of GS XY 0507. Durable silver coatings are used to achieve maximum reflectivity, with values of 96% measured at 45 ± 10 degrees.

Potential limitations introduced by a line scanner in x-y imaging are the pixel positioning error along the Y direction (wobble) and along X (jitter). Typical figures achievable with GS XY 0507 are better than 0.1% for both these parameters.

3. One-dimensional depth profile measurements

A solution is presented in this chapter for the measurement of one-dimensional depth profiles, based on the application of the principles of low coherence interferometry. The method can be applied to both single and multi-layer objects and the features described here form the basis of the scanning surface topographic technique, which is analysed in Chapter 4.

The opening paragraphs contain a discussion on the characterisation of optical sources through the measurement of their auto-correlation functions. The study focuses then on the theoretical and experimental study of focusing optics and on the comparative analysis of the effect of surface roughness on the interferometric signal. At the end of the chapter a novel procedure for low coherence eye length measurement is presented.

3.1 Characterisation of optical sources

The interest for the characterisation of the coherence properties of any source used in a low coherence interferometer stems from the link between the source coherence length and the axial resolution of the interferometer. From the shape and width of the experimentally determined auto-correlation function one could subsequently find the expected resolution of the interferometric distance measurement procedure, as shown in paragraph 1.3. At the same time, a correlation can be made between the theoretical values predicted from the spectral shape characteristics provided by the manufacturer and the measured source auto-correlation function.

A number of broadband optical sources supplied by SUPERLUM Moscow, mainly super-luminescent diodes (SLD), with coherence lengths in the range 20 ... 50 μm were used throughout the series of experiments described in Chapters 3 to 6. A versatile SUPERLUM multi-electrode device, described in paragraph 3.1.2, was also used in a series of experiments.

3.1.1 Superluminescent diodes (SLD)

Spectra of a batch of pigtailed superluminescent diodes (SLD) were evaluated using an optical spectrum analyser (Hewlett-Packard 5461A) and an experimental procedure was devised to measure their auto-correlation functions. This exercise was necessary in order to select those devices exhibiting symmetric spectra with minimum ripple (see paragraph 2.1.3.3), which are best suited for use in low coherence measurements.

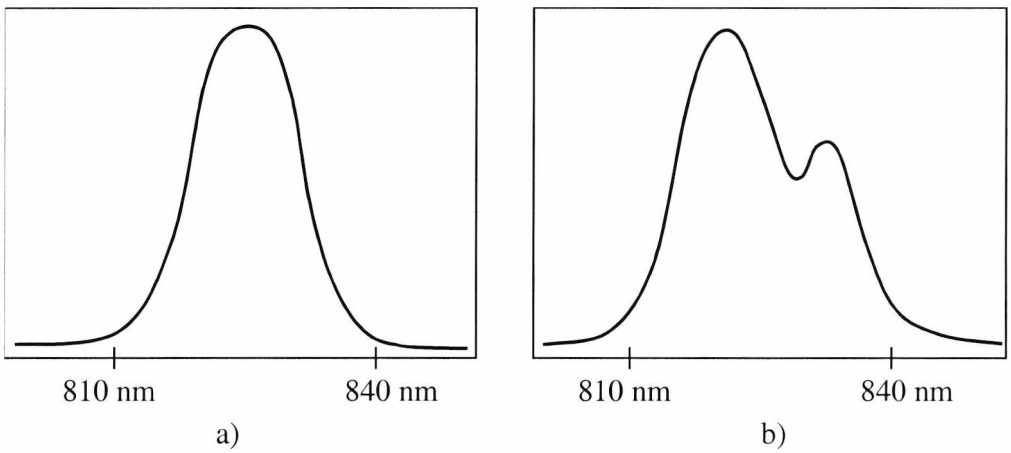

Figure 3.1 Comparison of superluminescent diode spectra:
(a) SLD-361 series; (b) SLD-371 series

In contrast with typical SLDs with Gaussian or near-Gaussian spectra, devices in the SUPERLUM SLD-371 series exhibit a 'double-peak' spectral shape. Figure 3.1(a) shows a Gaussian SLD-361 series spectrum with a corresponding Gaussian auto-correlation function. An asymmetric SLD-371 spectrum giving rise to an interference signal consisting of a central signature accompanied by satellite signatures is shown in Figure 3.1(b). Such additions to the central peak can place an unwanted limitation on the resolution of a LCR system by decreasing the system resolution from the value corresponding to the FWHM of the central peak region to one corresponding to a distance interval comprising the two satellites. In imaging applications, as will be shown later in Chapter 4, such satellites could give rise to "image doubles" detrimental to the image quality.

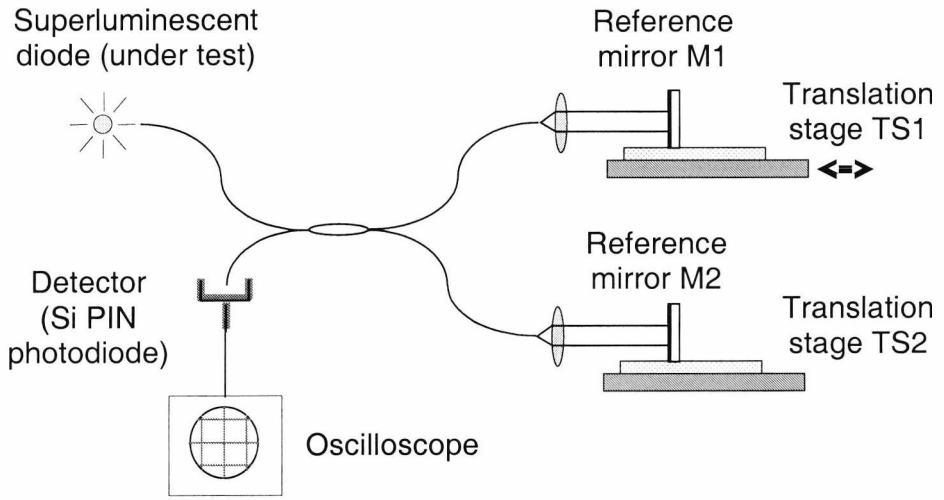

Figure 3.2 Interferometer set-up for the characterisation of the source auto-correlation function

In the experimental set-up for the measurement of the auto-correlation function, diagramatically represented in Figure 3.2, a directional fibre coupler, collimating optics and mirrors mounted on translation stages form a Michelson interferometer. The translation stages (Aerotech) allow constant velocity scans over a few centimetres. The visibility of the photodetected interference signal is maximum at the position where the two arms are equal in optical length, as demonstrated earlier in paragraph 2.1.2.

As the position of reference mirror M1 (mounted on translation stage TS1) is scanned in the longitudinal direction with mirror M1 fixed, the interference signal as a function of distance, i.e. the source auto-correlation function, is recorded with a storage oscilloscope which allows waveform storage for subsequent analysis. Interferograms such as the ones shown for comparison purposes in Figure 3.1 are produced in this fashion.

3.1.2 Multi-electrode devices (MED)

Multi-electrode devices are optical sources which can operate in various regimes, according to the electrode connection configuration. Depending on the driving electrode configuration, a three-electrode device of this type supplied by SUPERLUM and whose auto-correlation in the SLD regime is shown in Figure 3.3 can behave either as an SLD, laser, bistable optical device or Q-switched laser [46], depending on the biasing and grounding of each of the three electrodes.

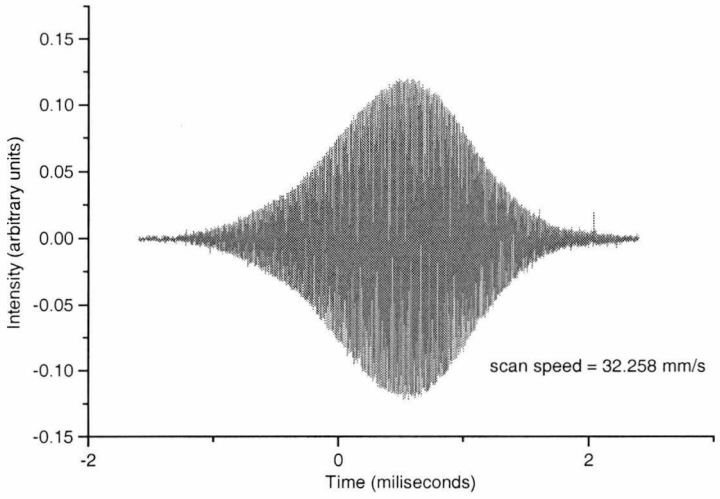

Figure 3.3 Auto-correlation of the SUPERLUM multi-electrode device (MED) in SLD regime

3.1.3 Temperature effected change in the spectral parameters

Among several environmental parameters, temperature plays a key part in the operation of the SLD devices, as mentioned earlier in paragraph 2.1.2, due to its influence on the broadening mechanisms of the optical source. Various manufacturers incorporate some form of temperature control in order to reduce the susceptibility of their products to high temperatures caused by operation at large bias currents. The cooling procedure for devices in the SUPERLUM range is discussed below in paragraph 3.1.4.

Temperature variations are found not only to affect the long-term performance of the sources but they can also induce more immediate spectral variations resulting in a change of shape for the auto-correlation profile. Notable temperature effects on the central wavelength and linewidth are of particular interest and have been investigated in order to optimise device performance while maintaining a safe operating temperature.

3.1.4 Cooling of the optical sources

Maintaining a constant source temperature for both SLD and MED through an adequate supply of cooling current to the Peltier element is the key factor in ensuring operation at the rated temperature.

The cooling of each SLD is achieved through a Peltier element, regulated by a temperature unit (Profile Gmbh) which controls the thermistor resistance through a variable supply of current. The SLD and thermistor tandem is mounted in a heat sink preventing rapid heat build-up in case of thermistor failure. The controller has proportional, integral and differential (PID) adjustments to the current feedback loop, which allow optimisation of the time taken to bring the SLD temperature to the nominal value.

Although the thermistors are identical across the set of sources used, PID settings were found to be specific for each source employed, due to each mount's particular geometry and heat-conduction properties. A series of experiments was carried out to determine the PID optimisation procedure and the ideal switch-on sequence for which the nominal cooling current value is reached with the minimum time delay.

The curves in Figure 3.4 illustrate the time variation of the cooling current over the first few seconds from switch-on for a number of combination of PID maximum, minimum and median settings on the 'Profile' controller front panel.

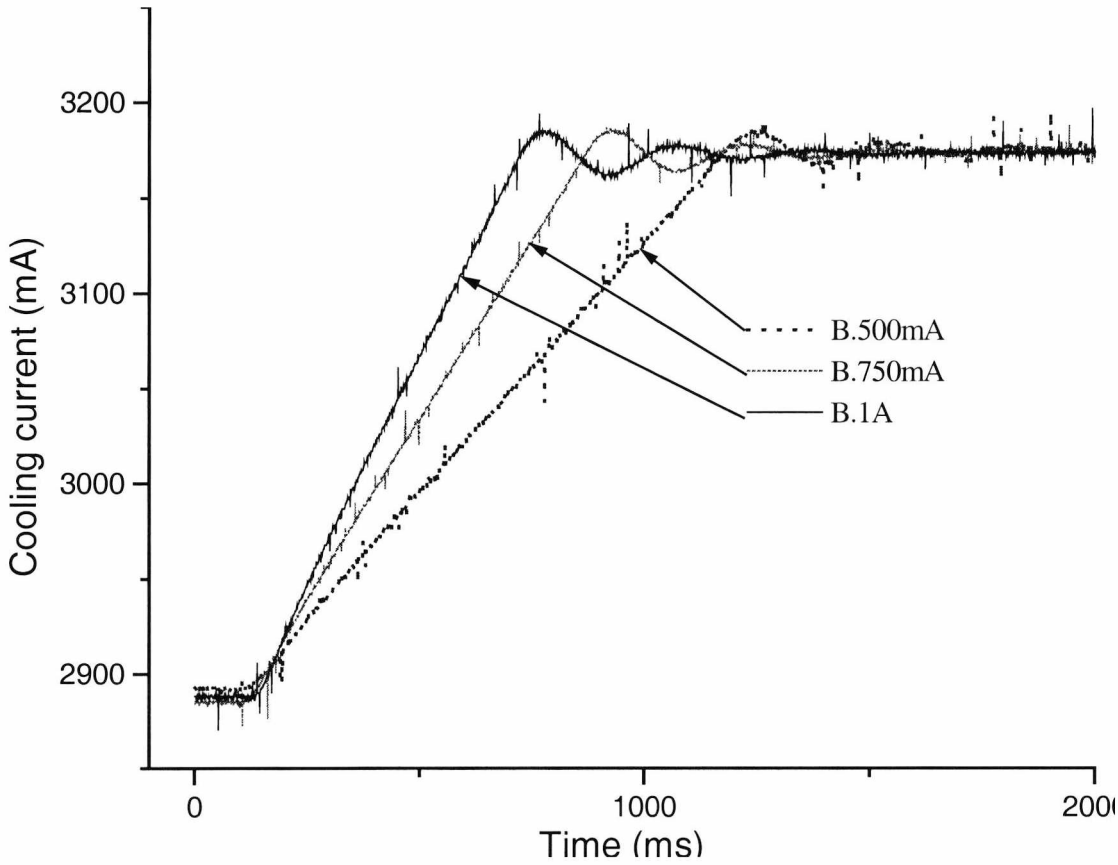

Figure 3.4 Time dependence of cooling current after temperature control unit switch-on

Ideally the cooling current should be rising fast and settling to the required level with minimum delay and oscillation after switch-on.

By monitoring its risetime (which can be done on the basis of observing the digital display, updated twice a second, on the front panel of the Profile cooling unit) this exercise can be carried out in a simple fashion for each combination of source and heatsink, thereby ensuring that the optical sources do not experience large temperature fluctuations and enabling the cooling current to be limited to a maximum value.

3.2 Initialisation of the interferometric set-up

The interferometric set-up used in source characterisation in 3.1.1 requires initialisation, like all other low coherence systems. The initialisation process consists of bringing the optical path length difference between arms (OPD) to a predetermined value, which in practice depends on the type of modulation used. This procedure is especially important after the set-up is modified with the addition or removal of components.

For Doppler induced modulation (longitudinal scan of reference mirror) the translation stage requires ramping from rest (acceleration and deceleration). The value of the OPD should therefore be of the order of the distance corresponding to accelerated stage movement in order to ensure constant mirror velocity and a sharp Doppler frequency peak in the coherence region (at OPD = 0). This distance is typically of the order of a few millimetres.

For high frequency phase modulation of the reference mirror, however, the OPD should be adjusted as close to zero as possible in order to maximise the phase modulation near the region of maximum fringe visibility.

3.2.1 Optical path difference adjustment

One novel technique [51] developed to assist in the OPD adjustment outside the coherence range relies on the channelled spectrum (CS) and microwave spectrum (MS) disturbance of the 'SUPERLUM' multi-electrode device (MED).

3.2.1.1.1 Experimental procedure

Light from a SUPERLUM multi-electrode device (MED) is split equally between the outputs of the first coupler, DC1 (Figure 3.5). The upper coupler arm delivers light towards a collimating arrangement (C1) and to a diffraction grating. The lower coupler arm directs light into a Michelson interferometer formed by the outputs of directional coupler DC2 and mirrors M1 and M2. The mirrors are mounted on

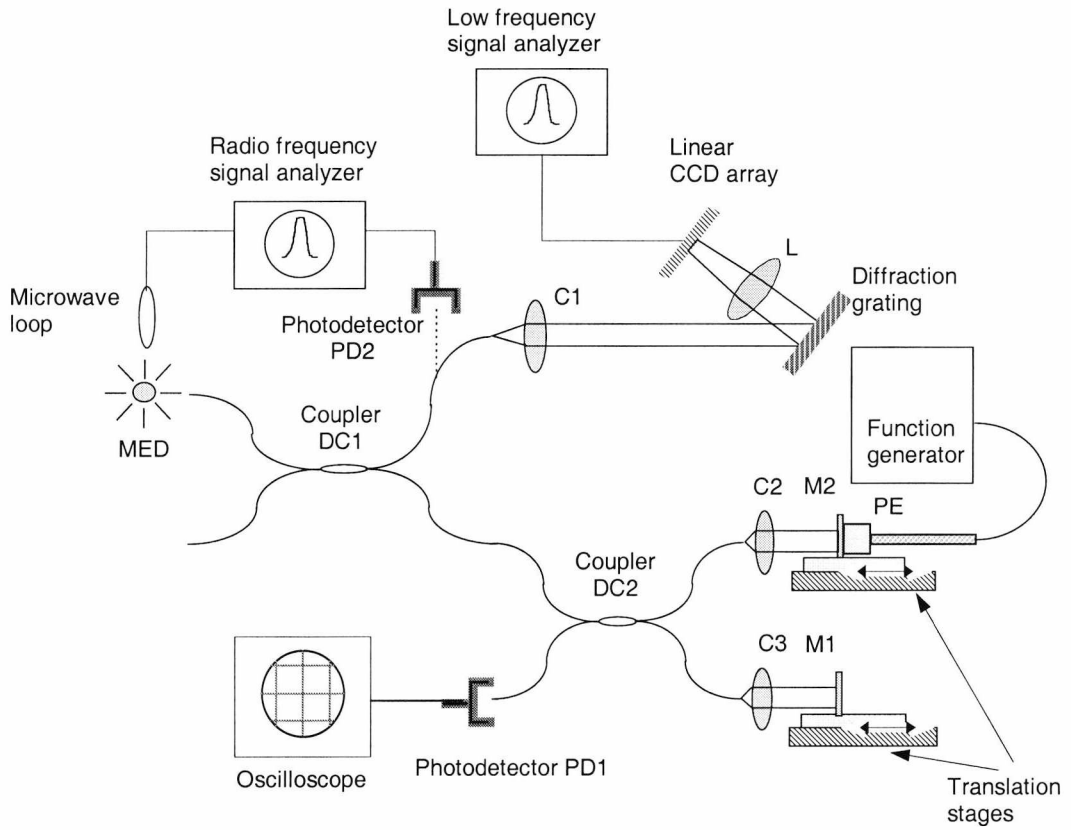

Figure 3.5 Schematic diagram of the set-up for OPD adjustment. Either PD2 or the CCD array can be used to provide a measurement of the optical path difference

computer controlled translation stages (Aerotech) capable of backward and forward translation at constant velocities of a few cm/s and whose longitudinal positioning accuracy is 1 μm.

Mirror M2 is mounted on a piezo-element PE which can be mechanically vibrated in the longitudinal direction through the application of a sinusoidal signal obtained from a function generator. When a match of the arms length corresponding to M1 and M2 is achieved (OPD = 0), an AC interference signal with components at the modulation frequency and its multiples is received by photodetector PD1 and its peak-peak value measured with the oscilloscope.

The remaining output of coupler DC1 is used for the display of the channelled spectrum of the multi-electrode device or for the measurement of the frequency spectrum of the light using a high frequency photodetector, PD2. A loop probe connected to a coaxial cable collects the RF field in the vicinity of the multi-electrode device and a radio frequency spectrum analyser is used to display the field's spectrum.

3.2.1.1.2 Microwave spectrum technique

With the OPD at zero (adjusted on the basis of maximising the fringe visibility signal at PD1), a disturbance of the RF spectrum of the field surrounding the MED and picked up by the microwave loop is noticeable when the position of mirror M2 is modulated by a low frequency signal. The linewidth Δf of the fifth harmonic (1070 MHz) of the MED pulse generated signal, present in the RF field and measured with the spectrum analyzer, changes as the OPD is increased from zero to a value below the coherence length.

The dependence of Δf on the OPD is illustrated in the graph in Figure 3.6 (b). The rms value of the signal detected using PD1 is shown in Figure 3.6 (a) for comparison. These data curves were obtained for a bias current of 113.5 mA and mirror M2 vibrated at 300 Hz with an amplitude $\approx 2\lambda$.

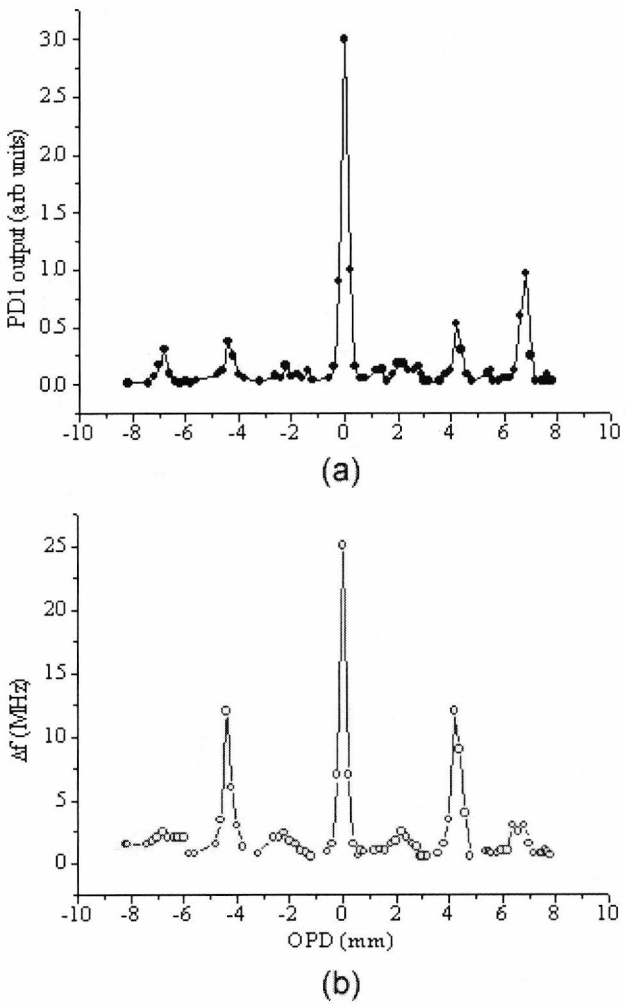

Figure 3.6 a) Fringe visibility as a function of OPD b) frequency enlargement of the linewidth of the fifth harmonic of the laser self-pulsation as a function of OPD.

Both graphs show how, in addition to the peak at OPD = 0, other maxima appear at integer multiples of the optical length of the MED cavity whose value, $(OPD)_c = 2.2$ mm, can be determined from the peak spacing. The profiles about the maxima for both the fringe visibility and the frequency enlargement signals have the same FWHM of about 270 μm. A similar dependence on OPD to that in Figure 3.6 (b) is obtained for the output of photodetector PD2.

This technique can be used to detect interference events when the OPD equals multiples of $(OPD)_c$. Only the peaks corresponding to the single, double and triple cavity round trips are shown in Figure 3.6, due to the translation stage having a limited range (100 mm), but it has been shown [52] that higher order multiples still provide sufficient amplitude for the interference signal. The comparison of the two graphs in Figure 3.6 demonstrates that the microwave spectrum technique is at least as sensitive in detecting interference events as the fringe visibility technique.

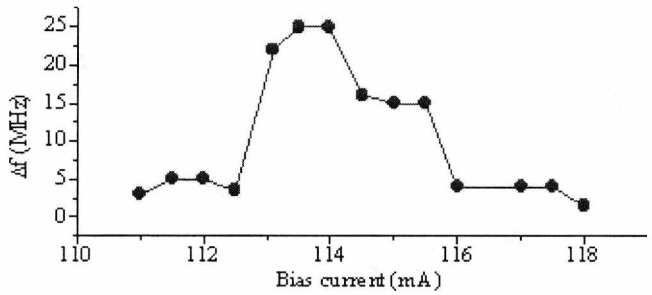

Figure 3.7 Microwave spectrum enlargement against MED bias current

The technique has been applied for different MED bias currents and has been found to produce variable results across the rated bias range. The graph in Figure 3.7 shows the bias range within which the RF bandwidth enlargement is most significant and suggests that the lower applicability limit is 112 mA, which can be correlated with the threshold in the amplifier section of the MED.

At the other end, for bias currents above 117 mA the MED becomes progressively less susceptible to the feedback signal, mostly due to the increasing role of the electrical pump compared with the optical feedback signal, therefore the useful bias range is 112 to 117 mA for the particular MED examined here.

3.2.1.1.3 Channelled spectrum technique

A spectrum of the source exhibiting peaks whose separation gives information about the cavity length (channelled spectrum) is obtained with a linear CCD array (Thomson 1728) after light emerging from the upper arm of coupler DC1 (Figure 3.5) is separated into its spectral components at the diffraction grating.

The main frequency component in the channelled spectrum, f_C, is the inverse of the peak-to-peak spacing, which in turn is inversely proportional to the cavity length, leading to a direct proportionality relationship between the channelled spectrum frequency and the value of OPD_C [53].

$$f = k \times OPD \tag{3-1}$$

The value of the constant k is found to be k = 36.2 kHz/mm, from the measurement of the channelled spectrum frequency f at different OPD values. For a CCD readout time of 1.7 ms, the frequency corresponding to the MED cavity length is found to be f_c = 86 kHz. Consequently the value for OPD_c (which is twice the cavity length, due to the double pass of light through the cavity) results as 2.2 mm, in agreement with the distances between adjacent peaks in Figure 3.6.

An estimate of how far the interferometer is from balance can be obtained by measuring the visibility of frequency components f and f - f_c, since the amplitudes of these components increase with a reduction in the OPD. The bias value does not influence the amplitude of the f_c component but it controls the amplitude of the f component. As regards the optimum bias current, Figure 3.8 shows that the channelled spectrum visibility is higher in the same bias range where the RF bandwidth is greatest (Figure 3.7).

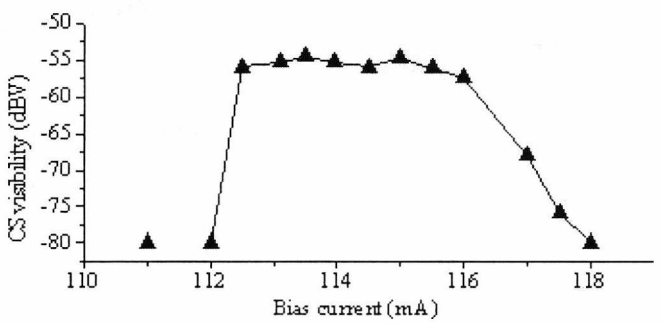

Figure 3.8 Channelled spectrum visibility against MED bias current

A combination of the two techniques allows an estimate of the OPD to be carried out for three different ranges:

1. For a large OPD multi-electrode device pulse modulation can be used. The pulses generated by the MED are 50-100 ps wide [46]. Pulses returned from each arm with a relative delay of 0.1 ns can be resolved (corresponding to an OPDs larger than 3 cm) using a 2 GHz avalanche photodiode and a 1 GHz oscilloscope. Once the actual OPD and the direction of change have been estimated, the reduction of the OPD to less than 1 cm is quite straightforward.

2. The channelled spectrum technique can be used in the range $l_c < OPD < 1$ cm. From the interference signals due to the multiple trips in the laser cavity, information can be obtained about the OPD via both microwave and channelled spectra. In the range $l_c < OPD < (OPD)_c$ the channelled spectrum method gives an absolute value of the OPD.
3. In the range $OPD < l_c$, the microwave spectrum technique can be used for fine OPD adjustment.

The application of these techniques is summarised in Table 3-1.

OPD	Estimation technique
> 3 cm	MED pulse delay measurement
$l_c < OPD < 1$ cm	Microwave or channelled spectrum
$l_c < OPD < (OPD)_c$	Channelled spectrum
$OPD < l_c$	Microwave spectrum

Table 3-1. Summary of OPD initialisation techniques

After carrying out the desired OPD adjustment in the system, the MED can be operated in the SLD regime and used in low coherence measurements by driving electrodes 1 and 2 and grounding electrode 3.

3.3 Target distance measurement

Interferometric measurement of distances is inherently relative, as shown in Chapter 2, since the only measurable quantity is the OPD between the interferometer arms. A highly stable interferometer is therefore required to produce accurate absolute measurements. Any physical changes that may occur in the non-common light propagation paths may generate errors and therefore system components in these arms must be fixed firmly with respect to each other in order to minimise OPD drifts. The use of components with moving parts such as translation stages raises the question of positioning repeatability when they are employed in a regime of cyclical repetitive longitudinal scans involving sharp acceleration and deceleration followed by a return to their original position. OPD re-initialisation may be required in cases where a consistent drift is noticeable.

Depending on the required accuracy of the interferometer in which the positioning stage is used, this re-initialisation may not be required for stages provided

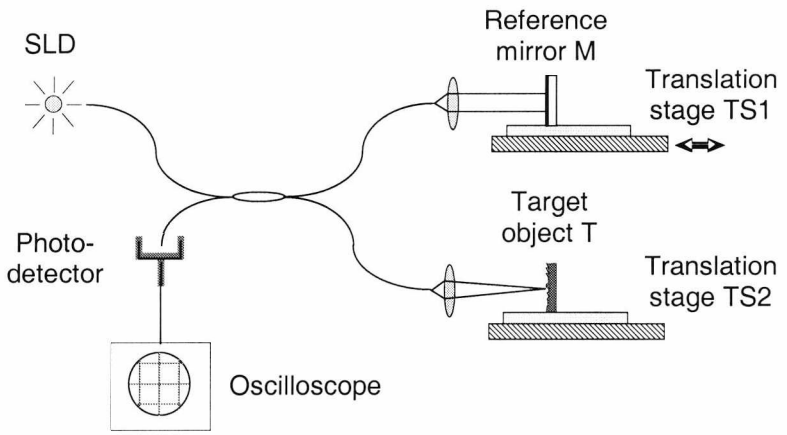

Figure 3.9 Experimental set-up for single-point measurements

with a feedback circuit that uses an in-built stage position sensor to minimise drifts and allows the repeatability value to remain in the region of 1 to 2 μm over a few hundred cycles. However, if sub-micron accuracies are required, a sub-system for monitoring the OPD between the arms should be incorporated in the interferometer.

A standard Michelson configuration similar to that used for source characterisation is represented in Figure 3.9. Light returned from mirror M and that returned from the location of the beam focused on the surface of target object T recombine and generate an interference signal at the photodetector. The reference path is modulated by longitudinally scanning translation stage TS1 and inducing a Doppler shift in the way discussed in 2.1.3.2. The object is also mounted on a translation stage mainly in order to facilitate a more convenient OPD initialisation in conditions of a limited translation range (extra OPD is available when two stages are employed). Single point surface distance measurements carried out with this set-up were principally aimed at the determination and optimisation of the achievable signal to noise ratio for targets of various reflectivity.

3.3.1 Beam collimation

Light emerging from the reference coupler arm in Figure 3.9 is directed by the reference collimating optics onto the reference mirror where it is reflected, returned and re-injected via the same optical elements into the fibre. The first requirement of the collimating optics is to minimise beam divergence along the airpath between the optics and the mirror, therefore enabling reciprocal beam propagation geometry for the return leg even when the longitudinal position of the reference mirror is changing during scanning. The second requirement is to enable beam re-focusing to the narrow fibre tip with high re-launching efficiency.

In the object arm the distance between the target surface and the collimating optics is maintained constant. Information about a single surface point is required, therefore the object light beam emerging from a single-mode optical fibre is focused to a tight spot on the object surface. A convenient way of achieving this is to use a combination of lenses readily available as a package in the form of a microscope objective. To illustrate the typical divergence of a single-mode fibre light output before and after collimation, measurements of the optical power of the beam were carried out at a series of longitudinal and transversal locations relative to the fibre end, which effectively amounts to 3-D beam profiling. A detector probe was mounted on a pair of 1 μm resolution translation stages capable of motion in the lateral and longitudinal directions and placed before the end of a standard 800 nm single-mode fibre cleaved at a right angle. A small pinhole (100 μm diameter) was placed in front

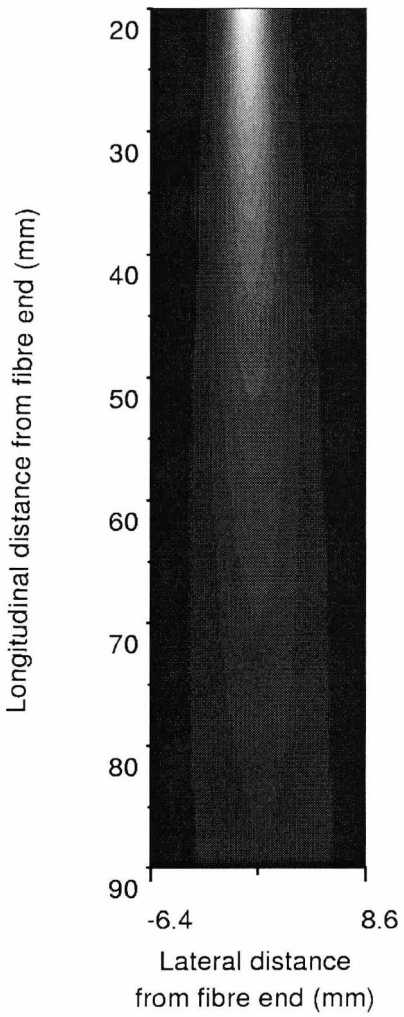

Figure 3.10 Greyscale map of the 3-D beam profile of light emerging from a single-mode optical fibre

of the detector window in order to increase lateral resolution.

The translation stages were programmed to execute a raster scan (fast lateral followed by step longitudinal) between 20 and 90 mm from the fibre end and spanning a lateral range of 15 mm. The resulting beam profile array consisting of 11,250 data points is represented in Figure 3.10 in the form of a greyscale map. The apparent non-parallelism of the axis of symmetry of the beam with the longitudinal scan direction suggests a slight fibre / translation stage misalignment, not easily identifiable on visual inspection of the fibre tip orientation due to its small physical size. Correction of such misalignments is important especially for the reference beam in a scanning interferometer configuration (see Figure 3.9) where they would contribute to an amplitude modulation, during longitudinal scanning, of the light from the reference mirror re-injected into the coupler arm.

The expected lateral beam intensity profile at any given longitudinal location is a Gaussian curve [41] in accordance with the Gaussian optics propagation model (Figure 3.11) which gives the intensity distribution I(r) as a function of the beam waist parameter w(z) and the intensity I_0 at r = 0:

$$I(r) = I_0 \exp\left(-\frac{2r^2}{w(z)^2}\right) \tag{3-2}$$

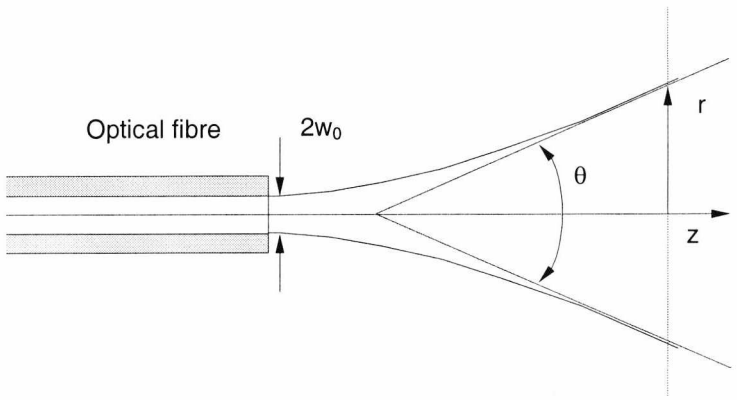

Figure 3.11 Illustration of the beam emerging from an optical fibre and its parameters

The parameter w(z) (defined as the beam radius at which the intensity has decreased to $1/e^2$ or 0.135 of its value on the z axis) can be expressed in terms of the beam divergence θ and wavelength λ as follows:

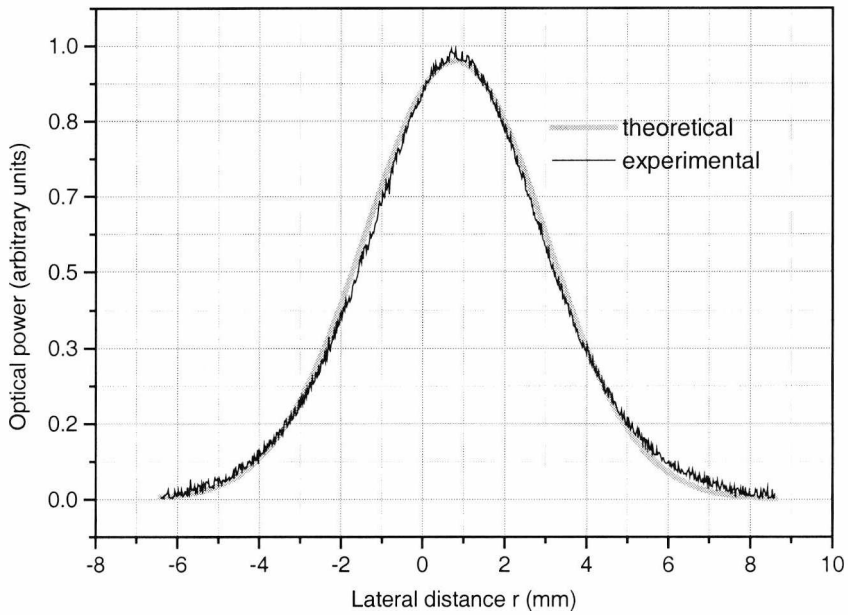

Figure 3.12 Theoretical and experimental beam intensity profile at a distance z = 50 mm from the fibre

$$w^2(z) = \left(\frac{2\lambda}{\pi\theta}\right)^2 \left[1 + \left(\frac{\pi\theta^2 z}{4\lambda}\right)^2\right] \tag{3-3}$$

For a Corning single-mode fibre of the type employed here the divergence angle, based on the fibre numerical aperture NA given by equation (2-31) is given by:

$$\sin\theta = \sqrt{n_2^{\,2} - n_1^{\,2}} \tag{3-4}$$

resulting in a divergence angle value $\theta = 0.158$ rad.

The theoretical and the experimentally determined intensity profiles at a distance z = 50 mm from the fibre are superimposed for comparison in the graph in Figure 3.12.

3.3.2 Reflection at an interface

The interdependence shared by the various electric field components of waves incident, reflected and transmitted at the interface between two media is given by the

Fresnel equations. These relations, in their general form, distinguish between the parallel and the perpendicular components on the plane of incidence. However, for the purposes of the experiments described in this chapter, the simplified form of the Fresnel equations, giving the surface reflectance R (ratio of reflected to incident power) and transmittance T (ratio of transmitted to incident power) in terms of the refractive indices of the media at normal incidence, are a useful starting point [15]:

$$R = \left(\frac{n_2 - n_1}{n_2 + n_1} \right)^2 \tag{3-5}$$

$$T = \frac{4 n_1 n_2}{(n_1 + n_2)^2} \tag{3-6}$$

3.3.2.1 Target types

Four sets of reflector samples were chosen as target surfaces: a set of transparent and a set of matt 1 mm thick glass microscope slides and three sets of transparent and matt glass microscope cover slips of thickness 90, 110 and 130 μm. This particular choice of targets facilitates the building of a stack of reflecting layers (cover glass slides are easy to handle in large quantities) of gradually increasing complexity. It also enables a direct comparison between the interferometric signatures of a reflected beam (specular reflection, optically flat target surface) and a backscattered beam (diffuse reflection, optically rough target surface).

The application of equations (3-5) and (3-6) for the particular case of normally incident light on a glass-air interface yields R = 4% and T = 96%. Glass is, however, a comparatively strong reflector. For a number of materials and surfaces the reflected / incident power ratio is much smaller and it is more convenient to express the reflectance as a logarithmic ratio of the power of light reflected (P_R) and incident (P_I):

$$R = 10 \log_{10} \left(\frac{P_R}{P_I} \right) \tag{3-7}$$

According to (3-8) the Fresnel reflection standard of a non-coated glass-air or air-glass interface reflecting 4% of the normal incident power has a corresponding reflectance value of -14.6 dB.

3.3.2.2 Single reflector measurements

A Doppler shift is introduced in an interferometric system, as explained in paragraph 2.1.3.2 by longitudinally scanning the reference mirror at constant velocity. Prior to applying this technique to the measurement of distances the accuracy of the translation stage velocity was investigated with an interferometer employing a laser source, which gives rise to an interference signal along the whole calibration range. The stage was programmed to accelerate to the set velocity, run at this velocity for a distance of 50 mm and then decelerate to rest. The stage position, and therefore its velocity, can be calibrated by recording the fringe number in the interference pattern against time.

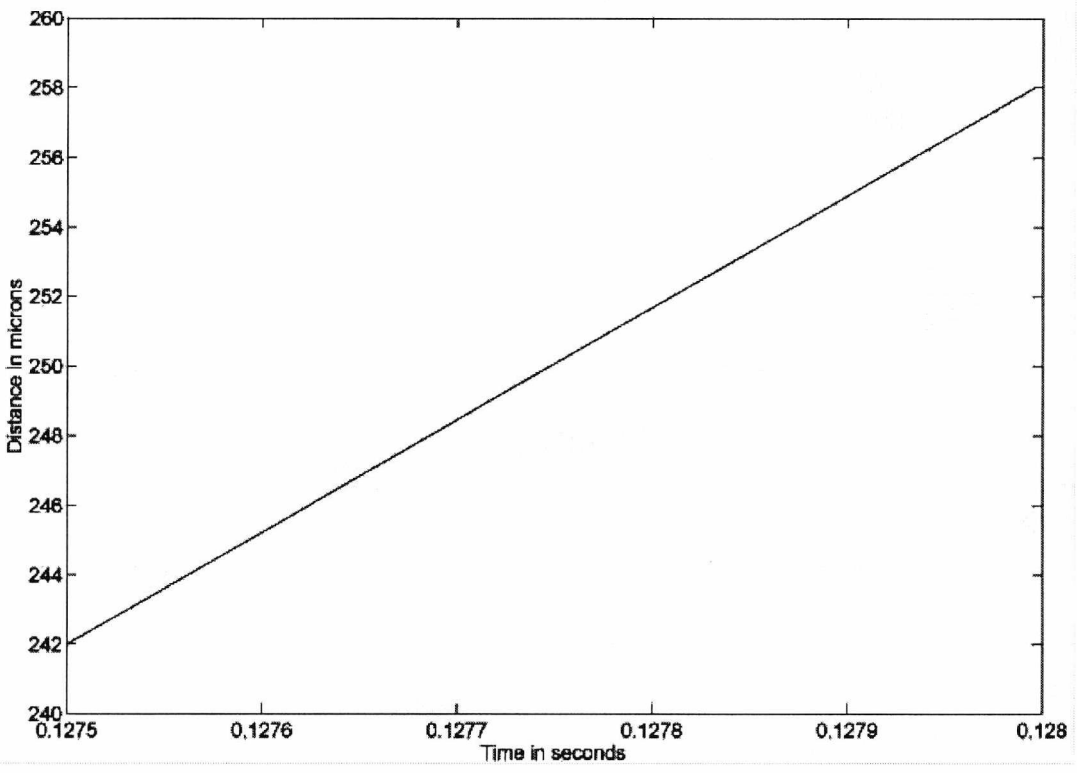

Figure 3.13 Illustration of the result of dynamic calibration of stage motion based on fringe counting

An example of the calibration curve corresponding to constant velocity motion is illustrated in Figure 3.13. Analysis of a number of similar datasets in different regions of the constant velocity range yield a value of 0.01% for the velocity mean standard deviation.

The interferogram in Figure 3.14 is a typical example of a low coherence reflectometry single point distance measurement carried out with the basic experimental set-up in Figure 3.9. In this instance, the target is a generic microscope slide. The interferogram was obtained by longitudinally scanning the reference mirror at a speed of 26.5 mm/s, which represents the factor for the conversion of the time scale of the photo-detected Doppler frequency signal to the interferogram distance scale. The resulting Doppler shift is at a frequency f = 200 kHz. The interferogram has the expected Gaussian shape, modulated by fringes at the Doppler frequency in the time domain or at the spatial frequency corresponding to the mean wavelength λ in the spatial domain. Furthermore, it is fairly straightforward to fit a Gaussian envelope to the interferometric signature in most cases where a strong reflection is detected from

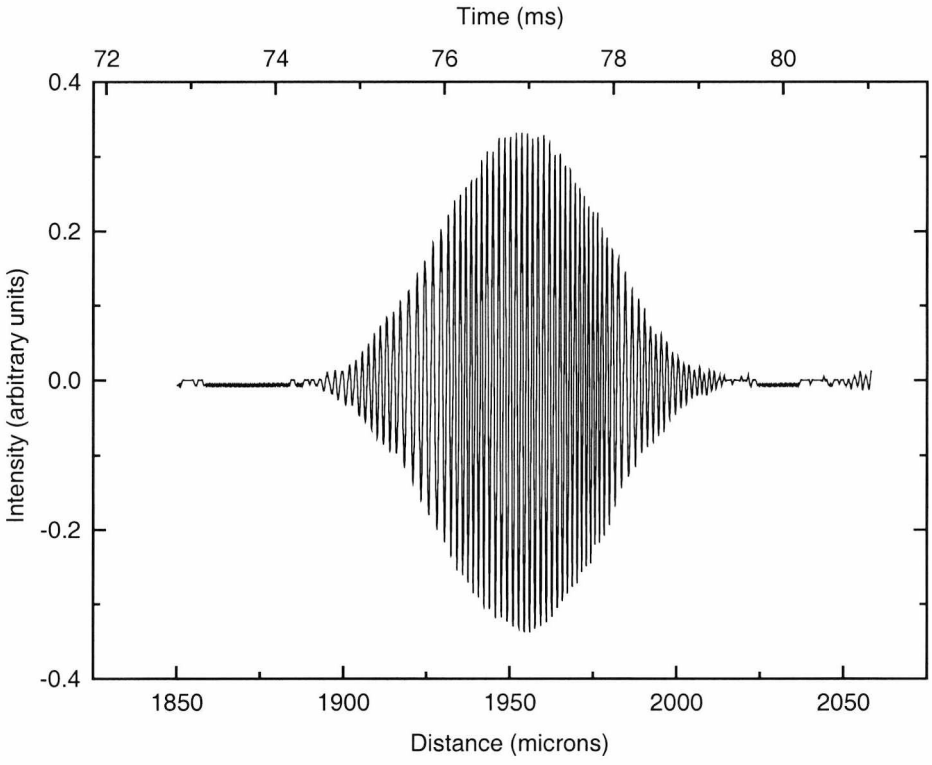

Figure 3.14 Raw photo-detector output interferogram obtained from the surface of a microscope slide (air-glass interface). The time scale is converted to a distance scale by multiplication through the stage velocity. Optical power incident on the target is 200 μW

an isolated interface. A fast computer curve-fitting algorithm was developed in order to make this process simultaneous with data acquisition.

3.3.2.3 Distance between two reflectors

The accuracy of the centroid determination procedure can be assessed by repetitively measuring the distance between two fixed identical reflectors (the back and the front of the microscope slide) and performing a statistical analysis on the set. In a run consisting of 100 longitudinal scans, the distance between the peaks of the two Gaussian fit curves was found to be 1012.5 ± 0.138 μm (the actual dataset is plotted in the graph in Figure 3.15).

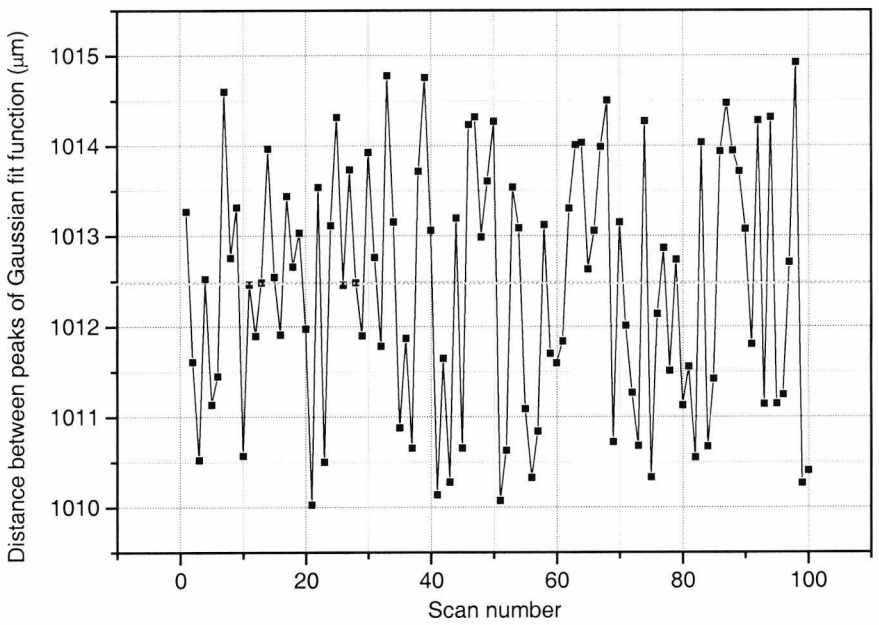

Figure 3.15 Statistical dataset of the distance between two reflectors obtained over 100 runs

The technique was successfully applied for the measurement of two reflectors whose separation is sufficiently large compared with the coherence length. In many cases of multi-layered structures, however, separations can be in the range of a few tens of microns, which raises the question of the minimum resolvable separation of two interfaces.

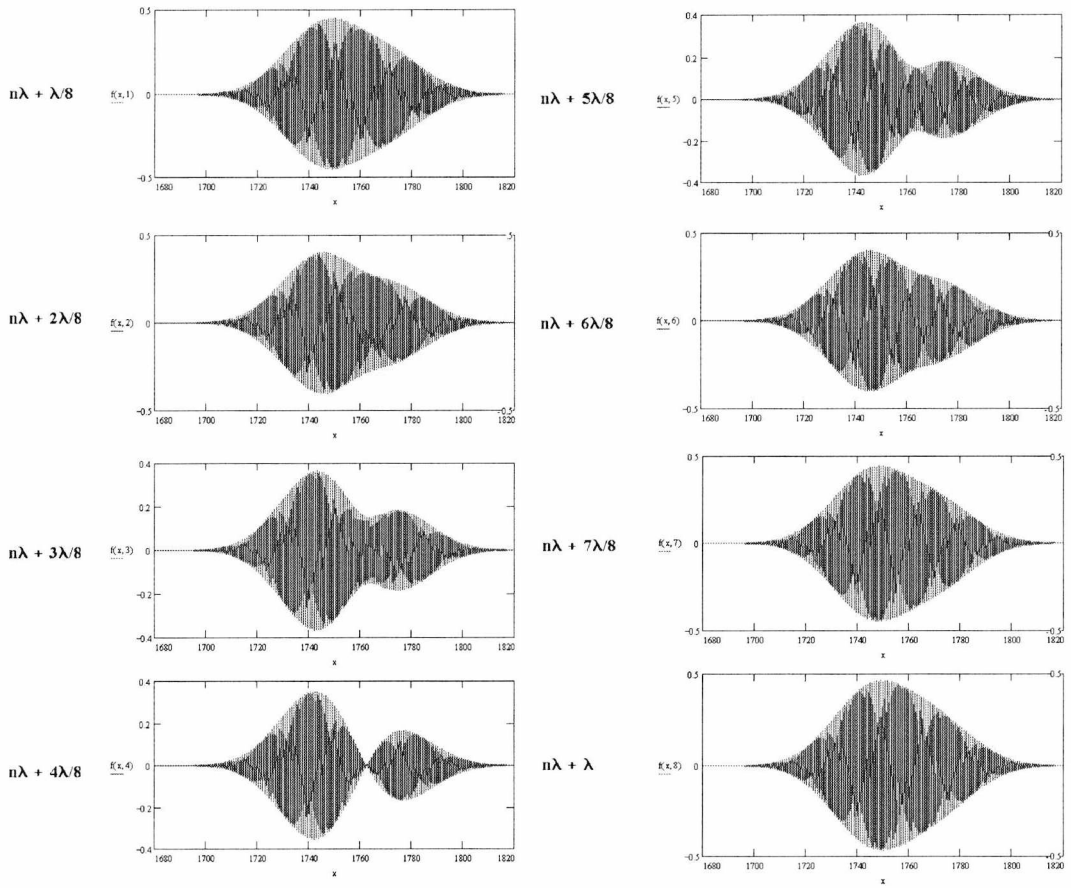

Figure 3.16 Effect of the mutual influence of coherence signatures from two reflectors (theoretical simulation). The distance between reflectors is varied in multiples of λ/8 between nλ and (n+1)λ

The effect of superimposing the interference signatures of two closely spaced reflectors was investigated in a theoretical simulation (graphs shown in Figure 3.16). The separation between two reflectors returning signals of different amplitudes is set to a value equal to half of the source coherence length. The shape of the expected interference patterns is seen to change considerably as the interface separation is increased in steps of λ/8, from nλ through to (n+1)λ (n integer). The two extreme cases, i.e. a node separating the two signatures, and one signature hidden in the wings of the other, correspond to reflector separations of nλ and (n+1)λ + λ /2.

This suggests that occasionally the interfaces can be resolved for separations smaller than the coherence length, but in general an aggregated indistinguishable signature is likely to be obtained for both reflectors. The minimum resolvable separation is therefore given by the interval at which there is a minimum mutual influence between the two signatures, i.e. at the source coherence length. Curve fitting

of the aggregate signature is likely to yield better accuracy, even for a considerable degree of mutual interference, but necessitates additional computing time.

To illustrate this effect, the signal returned from a thin layer of clear PVC film (Clingfilm) placed before a sheet of standard writing paper is shown in Figure 3.17. It can be noticed that the front and back reflections from the air-PVC and PVC-air interfaces are just resolved whereas the air-paper and paper-air ones are clearly resolved due to the greater thickness of the paper layer.

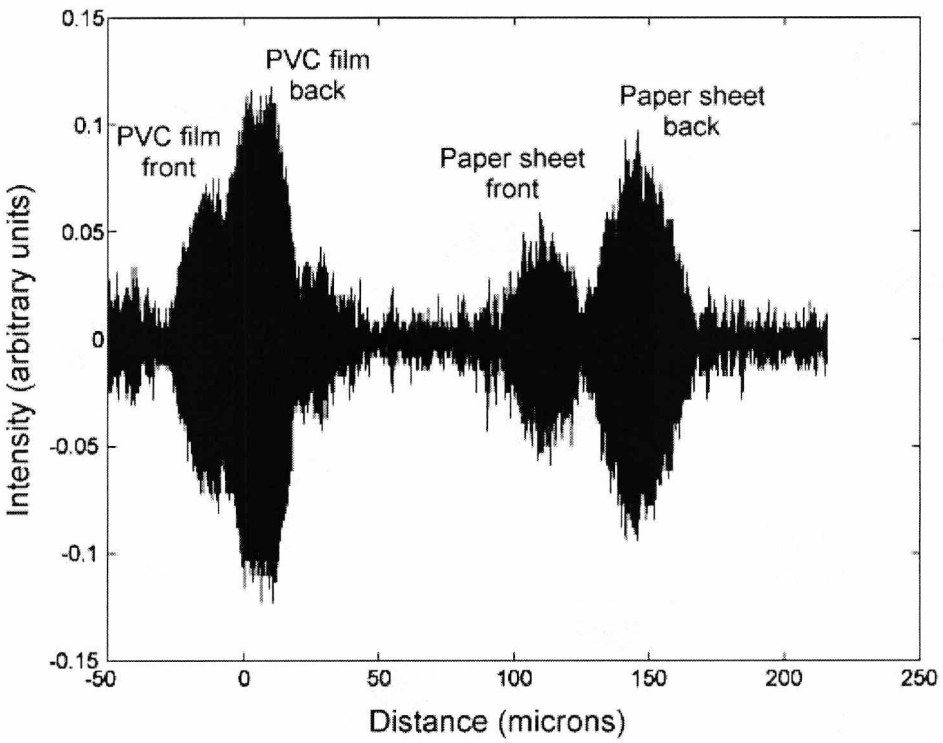

Figure 3.17 Coherence signatures of a PVC film and paper sheet

3.3.2.4 Multiple reflector measurements

A set of multiple reflectors formed by a stack of equally spaced microscope cover slips provides a convenient multi-layer target. The glass slips are arranged between two glass blocks, in such a way that air gaps of a thickness equal to twice the slip thickness are separating them.

The interferogram obtained from this type of target is shown in Figure 3.18. As expected, physically equidistant air-gap interfaces result in optical paths of different lengths, corresponding to the different refractive indices of air and glass. The last

element in the series is a glass block sufficiently thick not to provide a coherence signature from its back face for the limited reference stage run. Instead, additional 'ghost' reflections are noticeable, which correspond to multiple reflections in the cavities formed by the first eight interfaces. The inset shows an expanded version of the coherence signature corresponding to the first interface.

The surface reflectance of the inner interfaces was subsequently reduced by filling the air gaps with two liquids, water and diffusion pump oil, of refractive indices $n_{water} = 1.33$ and $n_{oil} = 1.45$ which are closer to the value of the refractive index of glass ($n_{glass} = 1.51$) and result in reflectance figures of $R_{water\text{-}glass} = 0.402\%$ and $R_{oil\text{-}glass} = 0.041\%$. The signal returned by the oil filled target is shown for comparison in Figure 3.19.

The reduction in surface reflectance is accompanied by a reduction in the amplitude of the coherence signatures. The optical path lengths of the spaces between glass blocks are also different in each case as a consequence of the change in refractive index.

Another parameter that is different in each of the three situations is the depth of focus, which is largest for the oil filled target and smallest for the air filled one. The change in the depth of focus leads to a 5% reduction in the amplitude of the signal reflected from the back end of the last cover slip.

The relative amplitude mismatch between the first and last signature in the series on one hand and the intermediary signatures on the other hand apparent in Figure 3.19 is due to a change in the relative alignment of the intermediary cover slips with respect to the front and end glass blocks. This alignment mismatch results in the front and end surfaces returning more light than the intermediary ones.

A comparison of the physical and optical distance from the first interface to every other interface in the set is represented in the graph in Figure 3.20, which shows clearly that absolute depth profiling of multi-layered structures is only possible if the refractive indices of the constituent layers are known. However, even if the refractive index is not known, the number of reflections can be determined, which may be important for industrial applications.

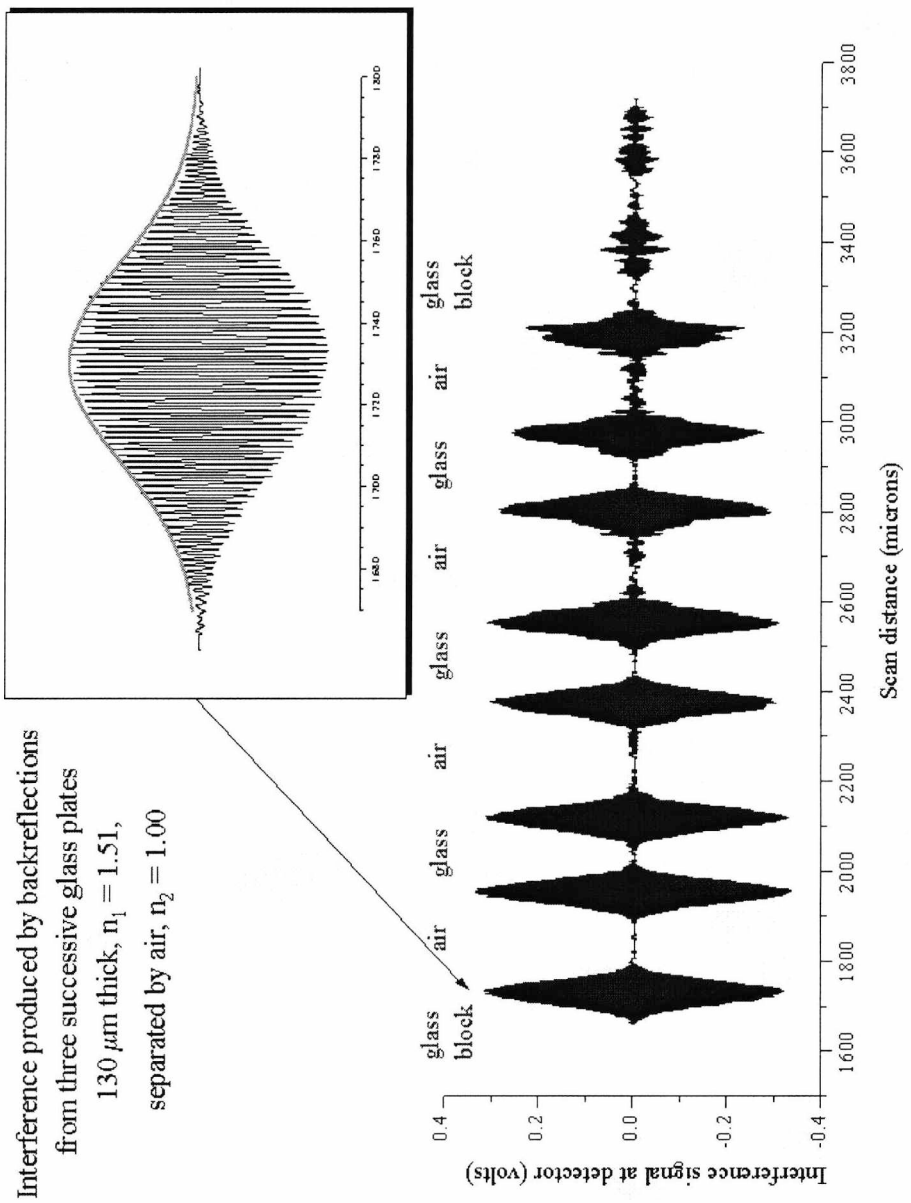

Figure 3.18 Illustration of multiple reflector distance measurement. The target consists of a series of microscope glass slides separated by air gaps.

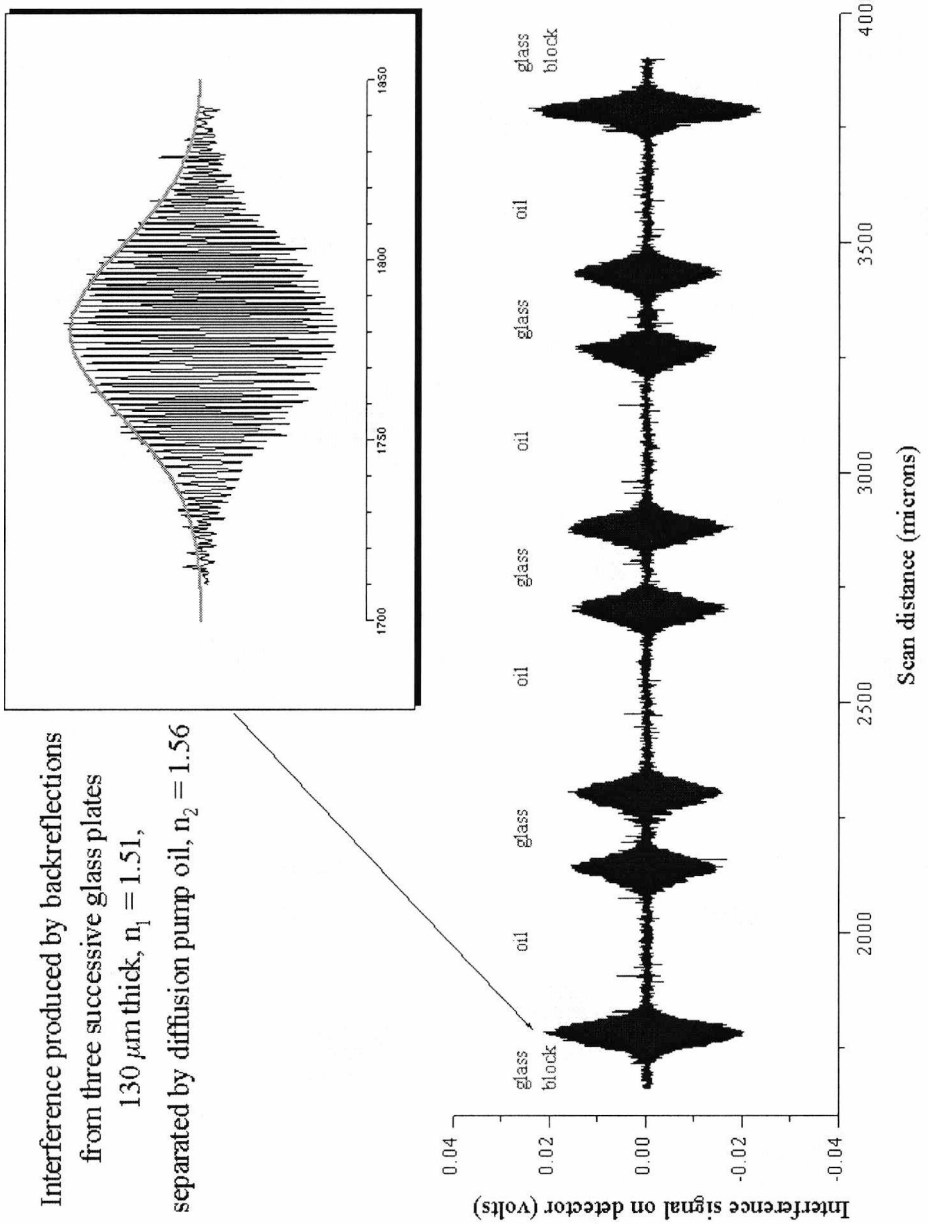

Figure 3.19 Illustration of multiple reflector distance measurement. The target consists of a series of microscope glass slides separated by gaps filled with diffusion pump oil.

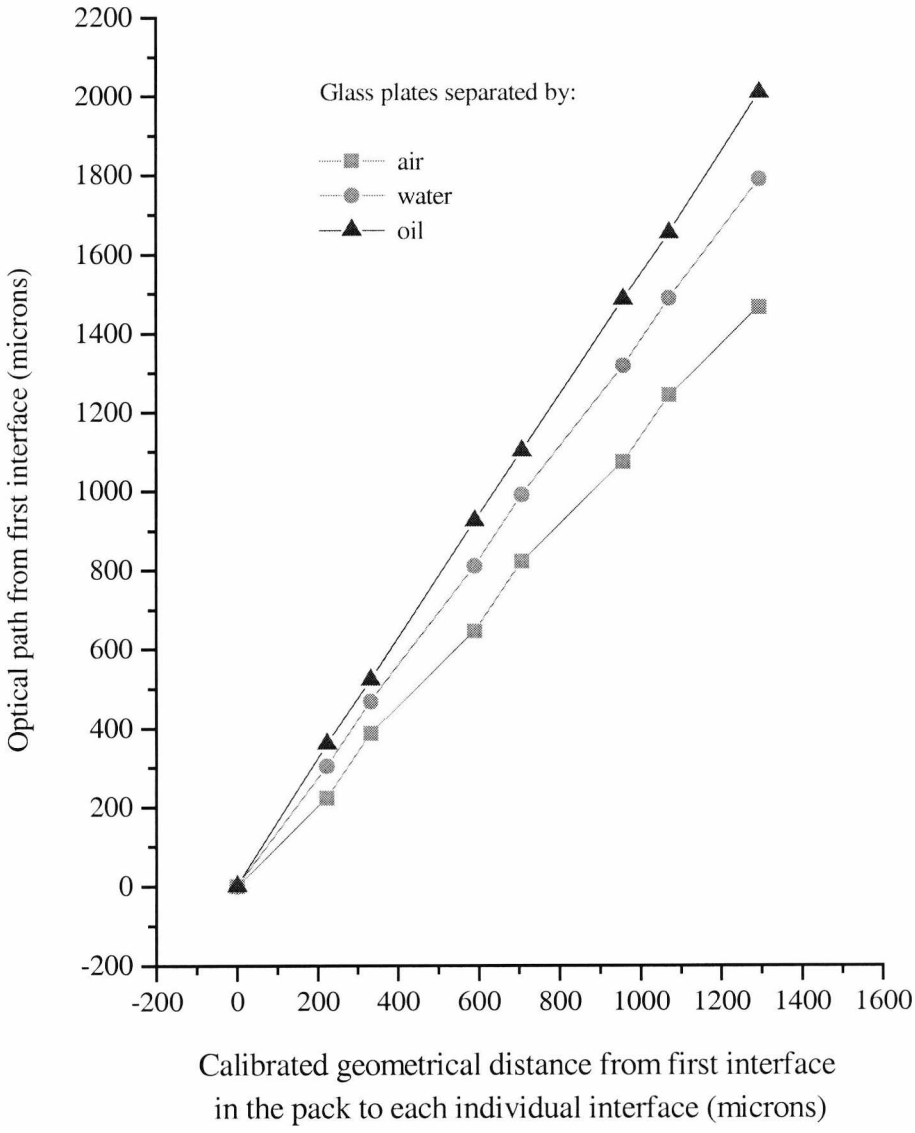

Figure 3.20 Optical distance vs. geometrical distance for each interface in the series

In many applications, however, comprehensive information about the refractive indices of the component layers of the structure under examination is not available with the exception perhaps of the fact that variation of the refractive index across layers is known to be small. For example, the refractive index variation across the layers forming the human retina is less than 0.05. In such a situation, as suggested by the line-up of points on the curve in Figure 3.20 representing the oil-filled case, physical dimensions are proportional to optical ones and information about the relative thicknesses of layers can be satisfactory for imaging purposes since the relative dimensions are preserved. In the other extreme case, that of air-filled gaps, the "skewed" line suggests a more pronounced departure of the optically measured intervals from the physical ones.

The minimum detectable object reflectance in this proof of principle set-up (and therefore not optimized for reducing noise) can be evaluated from the coherence signal corresponding to the first interface in each of the three cases. The smallest value corresponds to the oil filled case and for $R_{oil\text{-}glass} = 4.1\times10^{-4} = -33.9$ dB, $(S/N)_{oil\text{-}glass} = 20$ suggesting that for S/N = 1 the minimum surface reflectance detectable with the system operating in these conditions is -47 dB. However, improvement of the noise figures is essential in order to accommodate the anticipated reflectance of retinal backscatter, which is less than -90 dB in some portions.

3.4 Intra-ocular distance measurements on an eye model

A technique to measure the internal dimensions of multi-reflector targets was demonstrated in the previous section of this chapter. The targets investigated were static and any possible errors due to relative target motion during the measurement time span were minimal.

This section is concerned with extending the technique to the measurement of moving targets, with a view to providing a method of measuring intra-ocular distances in the living human eye. Such a method should enable simultaneous measurement of the position of two reflectors situated along the longitudinal system axis at a distance equal to approximately the length of the human eye, i.e. between 3 and 4 cm, thereby reducing the sensitivity of the apparatus to the inadvertent movements of the eye.

Previously demonstrated ways of measuring the eye length with a reduced sensitivity to axial eye movement either use 1) the interference between optical signals returned from the cornea and from the retina resulting in a poor signal to noise ratio, as both interfering signals come from the target and have relatively low amplitudes

[54] or 2) use two interferometers, one for each surface; the eye length is then obtained as the difference of the two OPDs, with the disadvantage that the interferometers are not independent.

In bulk optical arrangements it is possible to prevent light reflected from the reference arm of the first interferometer (closer to the eye) from reaching the photodetector in the second interferometer by fractionally tilting the mirror in the first interferometer. Consequently, the reference and the object beams form a non-zero angle and are only partially superposed on the first photodetector, with a corresponding loss in the visibility. A tilt angle of 5° for instance will result in a reduction in visibility by a factor of 25%.

Following the argument developed above, if the primary concern in the design of the experimental set-up is making the two interferometers independent, it is of interest to explore the possibility of constructing a symmetric non-reciprocal configuration where the photodetector in each interferometer would only receive the object signal and the reference signal of its own interferometer.

3.4.1 Asymmetric and symmetric configurations

In a two-interferometer set-up such as the one shown in Figure 3.21, light is delivered to the target (T) by means of two cascading directional couplers, DC1 and DC2. There are three available output ports: the object arm and the two reference arms.

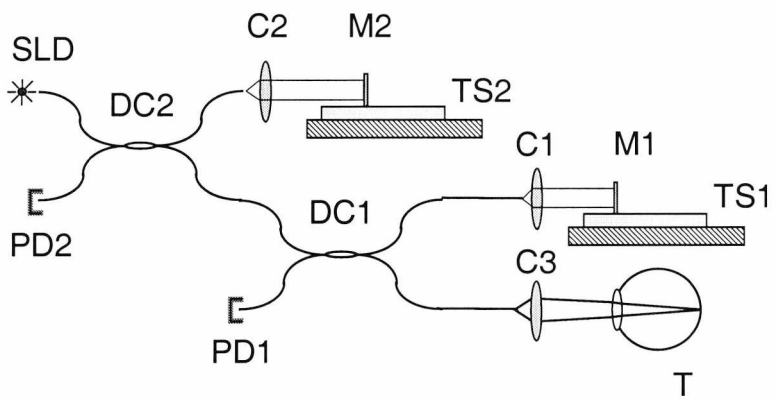

Figure 3.21 Arrangement of non-independent interferometers

In a fiberised version of this set-up, the Michelson interferometer formed by the M1 and T arms is referred to as interferometer 1 and that formed by the M2 and T

arms as interferometer 2. For the analysis of the power management in the system, the following notation applies: the power in fibre from the superluminescent diode (SLD) is P_0, the reflectivity of mirrors M1 and M2 are R_1 and R_2 respectively, and both the front and back interfaces of the object under test (T) are assumed to return a fraction U of the incident power; γ stands for the modulus of the optical field correlation function, d_{T1} is the OPD in interferometer 1, d_{T2} is the OPD in interferometer 2, d_{12} is the OPD between arms 1 and 2 measured from the split at DC2 and λ is the central wavelength of the SLD source. Using relation (2-19) (the Michelson interferometer transfer function) the powers of signals received by photodetectors, PD1, PD2 can be expressed as:

$$P_1 = \frac{P_0}{8}\left[U + R_1 + 2\sqrt{UR_1}\gamma(d_{T1})\cos\left(\frac{2\pi}{\lambda}d_{T1} + \varphi_{T1}\right)\right] \tag{3-9}$$

$$\begin{aligned} P_2 = \frac{P_0}{8}\Bigg[&\frac{U}{2} + 2R_2 + \frac{R_1}{2} + \\ &+2\sqrt{UR_2}\gamma(d_{T2})\cos\left(\frac{2\pi}{\lambda}d_{T2} + \varphi_{T2}\right) \\ &+\sqrt{UR_1}\gamma(d_{T1})\cos\left(\frac{2\pi}{\lambda}d_{T1} + \varphi_{T1}\right) \\ &+2\sqrt{R_1R_2}\gamma(d_{12})\cos\left(\frac{2\pi}{\lambda}d_{12} + \varphi_{12}\right)\Bigg] \end{aligned} \tag{3-10}$$

In the above equations the phase arguments denoted by φ_{T1}, φ_{T2} and φ_{12} represent the appropriate aggregate phase gains or losses introduced between corresponding arms by couplers and reflections. Specifically, φ_{T1} denotes the phase term between the target arm (T) and arm 1, φ_{T2} denotes the phase term between arm T and arm 2, and φ_{12} denotes the phase term arising between arms 1 and 2.

As shown by equation (3-10), the two interferometers are not independent. Whereas photodetector PD1 receives the coherence signal from interferometer 1 only, photodetector PD2 registers both the coherence signal from interferometer 1 (containing the factor $\gamma(d_{T1})$) and that from interferometer 2 (containing the factor $\gamma(d_{T2})$).

Due to the large discrepancy between the eye length and the coherence length mutual interference does not occur between light reflected from the front and back interfaces of the eye. The presence of light from the second, unwanted, interface at each photodetector does not therefore give rise to an interference signal but results in

an increase in the overall noise level (either shot noise or amplitude noise, depending on the aggregate optical power at the detector).

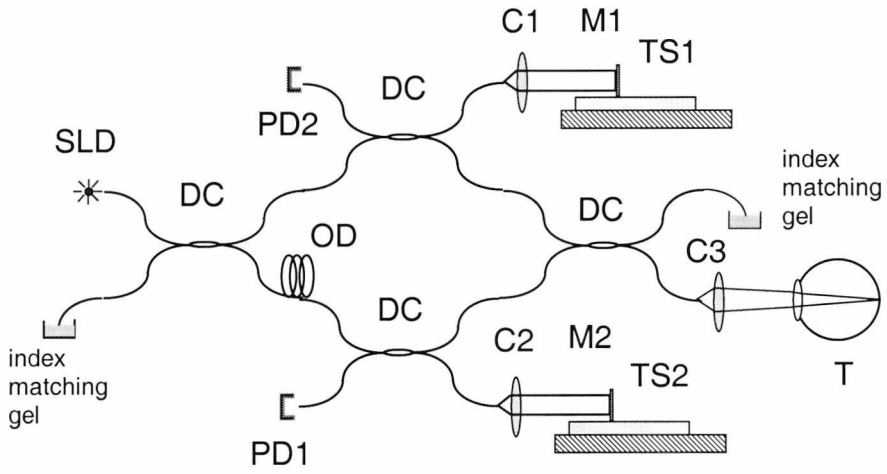

Figure 3.22 Arrangement with independent interferometers (symmetrical configuration)

The removal of this unwanted crosstalk can be achieved with a fiberised version of completely independent interferometers, shown in Figure 3.22, which is a combination of Mach-Zehnder and Michelson interferometers and represents a symmetrical configuration in comparison with the set-up in Figure 3.21 which is asymmetrical. The Mach-Zehnder interferometer, geometrically central to the configuration, has a path imbalance equal to the length of the optical delay line (OD). The photodetected power levels in this case, P_1 and P_2, are given by the following equations, which use, in addition to some of the symbols in (3-9) and (3-10), the following notation: d_D is the path imbalance introduced between arms 1 and 2 by the optical delay line OD, and φ_D is its corresponding aggregate phase term.

$$P_1 = \frac{P_0}{16}\left\{U + 2R_1 + 2\sqrt{UR_1}\left[\gamma(d_{T1})\cos\left(\frac{2\pi}{\lambda}d_{T1} + \varphi_{T1}\right)\right.\right.$$
$$\left. + \gamma(d_{T1} + d_D)\cos\left(\frac{2\pi}{\lambda}(d_{T1} + d_D) + \varphi_{T1} + \varphi_D\right)\right] \qquad (3\text{-}11)$$
$$\left. + U\gamma(d_D)\cos\left(\frac{2\pi}{\lambda}d_D + \varphi_D\right)\right\}$$

and

$$P_2 = \frac{P_0}{16}\left\{U + 2R_2 - 2\sqrt{UR_2}\left[\gamma(d_{T2})\cos\left(\frac{2\pi}{\lambda}d_{T2} + \varphi_{T2}\right)\right.\right.$$
$$\left. + \gamma(d_{T2} + d_D)\cos\left(\frac{2\pi}{\lambda}(d_{T2} + d_D) + \varphi_{T2} + \varphi_D\right)\right] \qquad (3\text{-}12)$$
$$\left. + U\gamma(d_D)\cos\left(\frac{2\pi}{\lambda}d_D + \varphi_D\right)\right\}$$

When the value of d_D is much larger than the investigation depth range, the Mach-Zehnder interferometer at the centre of the configuration in Figure 3.22 is imbalanced and the last two terms in (3-11) and (3-12) have negligible values because of a very small $\gamma(x)$ when $x \geq d_D$. By comparing equations (3-9) and (3-10) with (3-11) and (3-12), the coherence signals returned in the asymmetrical configuration are found to be larger than the coherence signals in the symmetrical configuration. The symmetrical configuration would ensure the independence of interferometers, but at the expense of reducing the optical power returned from the target. In the case of an *in vivo* eye measurement, however, any loss should be avoided.

Consequently, despite the advantage that the symmetrical configuration brings, attention is focused in the following section on the asymmetrical configuration.

3.4.2 Path modulation

In order to prevent the reference signal returned from mirror M1 from reaching photodetector PD2 in the asymmetric configuration (Figure 3.21), polarisation maintaining fibre elements should be used, with a view to control the polarisation of light from M1 which is reinjected into the system. However, due to polarisation coupling, only a limited value of the extinction of the orthogonal signal, stable in long run, can be achieved.

Alternatively, the signal reflected by piezo-mirror M2 can be sinusoidally phase modulated at a frequency f_c. After photodetection, the f_c carrier is demodulated to recover the Doppler beat signal from interferometer 2. For values of f_c much higher than the Doppler beat frequency, a good extinction of the coherent signal from the other interferometer may be achieved. Phase modulation can be carried out with an electro-optic modulator (for MHz modulation) or with a fibre wrapped piezo-cylinder which can support modulation rates up to 40 kHz [55]. However, this will involve the addition of some other components, which will inevitably increase the dispersion and complicate the experimental arrangement.

3.4.3 Signal processing

A reduction in the amount of cross-talk between interferometers 1 and 2 in Figure 3.21 can be achieved using a signal processing scheme combined with an optical balanced detection technique. A longitudinal scan of each of the two reference mirrors mounted on translation stages TS1 and TS2, at different speeds, results in Doppler beat signals of different frequencies. By choosing the translation speeds such that the resulting Doppler frequencies are not multiples of each other and by appropriate band-pass filtering a significant attenuation of the coherence signal from M1 processed by PD2 can be achieved.

The optical path differences (OPDs) in (3-9) and (3-10) can be written in terms of the velocity v_1 of mirror M1 and velocity v_2 of mirror M2 as:

$$d_{T1} = d_{T1}^{i} + v_1 t \tag{3-13}$$

$$d_{T2} = d_{T2}^{i} + v_2 t \tag{3-14}$$

$$d_{12} = d_{T1} - d_{T2} \tag{3-15}$$

where d_{T1}^{i} and d_{T2}^{i} represent the initial OPDs between arms T and 1 and arms T and 2, respectively. Consequently, the ac component received at photodetector PD1 has a frequency f_{T1} given by:

$$f_{T1} = \frac{2v_1}{\lambda} \tag{3-16}$$

The frequency of the ac component at the output of PD2 when the path of the second interferometer is blocked (for instance when $R_2 = 0$) is also given by (3-16). However, when $R_2 > 0$ the output of PD2 contains, in addition to the component at f_{T1}, frequency components at f_{T2} and f_{12} given by:

$$f_{T2} = \frac{2v_2}{\lambda} \tag{3-17}$$

$$f_{12} = \frac{2|v_1 \pm v_2|}{\lambda} \tag{3-18}$$

where f_{T1} and f_{T2} are the frequencies of the desired signals.
Furthermore, the line widths of these frequency components can then be expressed in terms of the spectral bandwidth properties of the low coherence source since its amplitude is modulated by a Gaussian-like function:

$$\delta f_{1,2} = \frac{2v_{1,2}}{l_c} \tag{3-19}$$

where l_c is the source coherence length.

Consequently, the necessary quality factor Q of the bandpass filter processing the signal is:

$$Q = \frac{f}{\delta f} = \frac{l_c}{\lambda} \tag{3-20}$$

For the particulars of the experimental set-up implemented here ($l_c \approx 31$ μm , $\lambda = 830$ nm), the numerical value for the quality factor Q is 37 which is commonly achievable with fairly inexpensive electronics.

3.4.3.1 Model eye

A model eye is constructed by attaching a 1 cm diameter convergent lens to a 29 mm diameter spherical flask made of clear glass (see Figure 3.23). The focal length of the lens is chosen to be also 29 mm in order to make it similar to the average crystalline lens in the human eye. The model eye was positioned in the object mount such that its equatorial plane intersected the optic axis of the object beam, thereby maximising the signal reflected in the longitudinal direction along the optical axis. For illustration purposes the diagram indicates the target volume as a series of concentric

spherical segments situated at the distal end of the sphere, although this model provides only two interfaces at the back of the flask, i.e. the inner and outer flask walls.

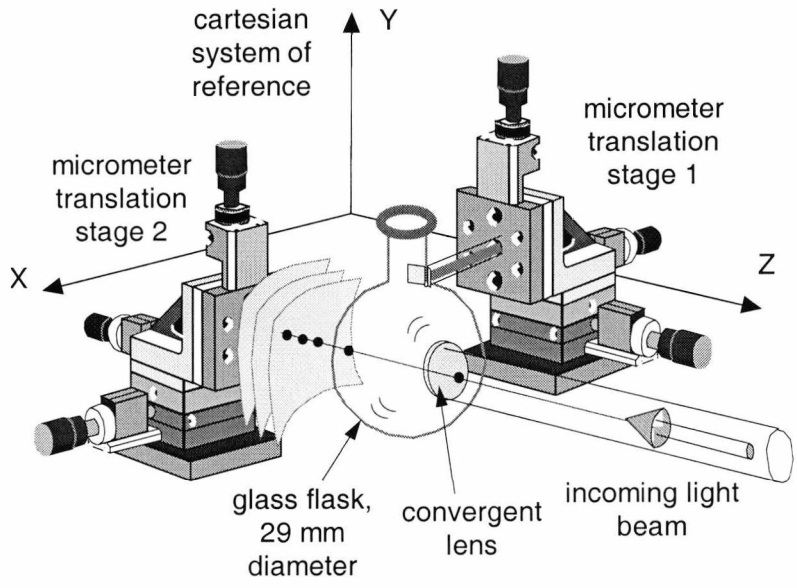

Figure 3.23 Model eye

Although a fairly basic model, the flask offers the advantage of easy access to its contents thereby allowing the use and interchangeability of liquids of various refractive indices, which can simulate a variety of optical "eye" lengths.

3.4.4 Experimental arrangement

The experimental set-up shown in Figure 3.24 is based on the asymmetric two-Michelson configuration in Figure 3.21 [56]. Light from a pigtailed superluminescent diode, SLD, is injected into a single mode directional coupler, DC2. Transmitted light from one of the output ports is fed into a second coupler, DC1, whilst the light from the other port is directed to mirror M2.

In each interferometer one arm (the reference), consists of a microscope objective, C1 (C2), mirror, M1 (M2) and computer controlled translation stage, TS1 (TS2). The other arm (sensing), consists of microscope objective C3 and the model eye ME. Light returned from the front (F) and back (B) of the model eye interferes with light returned from M1 and M2.

Interference events between the signal returned by M1 and the signals returned by F and B, respectively, are denoted (F,M1) and (B,M1). Similarly, when the other reference path is considered, these notations change to (F,M2) and (B,M2). Interference events corresponding to signals returned by the two mirrors are denoted (M1,M2).

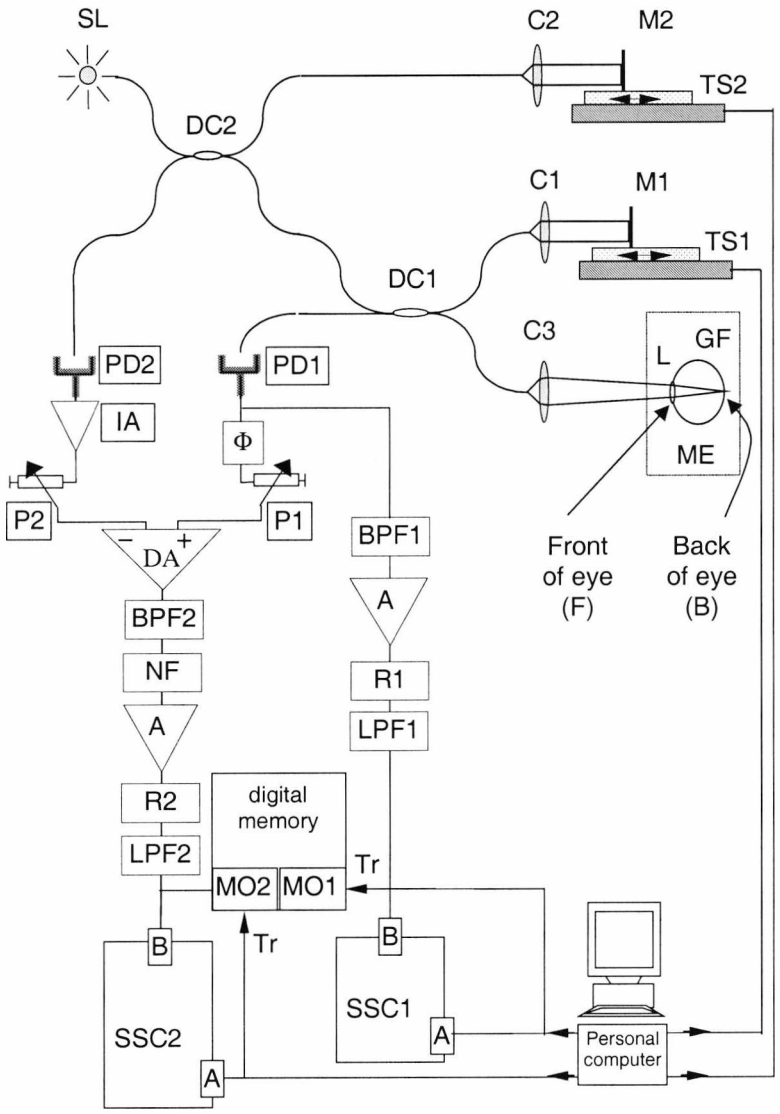

Figure 3.24 Experimental arrangement for the length measurement of the model eye.

SLD: Superluminescent diode (Superlum SLD-361); C1, C2, C3: microscope objectives; DC1, DC2: directional couplers; M1, M2: mirrors; PD1, PD2: photodetectors; IA: inverting amplifier; BPF1, BPF2: bandpass filters; NF: notch filter tuned to f1; R1, R2: rectifiers; TS1, TS2: computer controlled translation stages; ME: model eye consisting of L: lens and GF: glass flask; SSC1, SSC2: start (A input) - stop (B input) counters; P1, P2: potentiometers; MO1, MO2: memory oscilloscopes; Tr: oscilloscope trigger input.

3.4.5 Electronic circuitry

The signals are collected by two photodetectors, PD1 and PD2. For interferometer 1, the signal photodetected by PD1 is band pass filtered in BPF1 (all filters are commercially available units from Barr & Stroud or Kemo Electronics). Filter BPF1 is tuned to a frequency value f_1. The signal is then amplified, rectified in R1 and low pass filtered in LPF1.

In order to process the signal photodetected by PD2, a summing arrangement with the signal from PD1 is used to attenuate the interference signal coming from interferometer 1, i.e. to attenuate the signal of frequency f_1. The output signal from PD2 is inverted in IA and applied to the inverting input of the differential amplifier DA, whilst the signal from PD1 is applied to the noninverting input of DA. The attenuation set by potentiometers P1, P2 and the gain in IA are adjusted such that the gain for the PD2 signal is twice the gain for the PD1 signal, in order to balance out the "weight" of the $\cos(2\pi d_{T1}/\lambda)$ terms in (3-9) and (3-10). In order to implement a good rejection factor for the f_1 signal it is necessary that a correct balance of amplitudes is achieved as well as phase matching with phase shifter Φ. In this way, an attenuation of more than 16 dB has been obtained for the f_1 signal at the output of the differential amplifier.

Additional attenuation of the f_1 signal is introduced by the notch filter NF (tuned to f_1) and by the band pass filter BPF2 tuned to f_2, with the resulting signal subsequently rectified in R2 and low pass filtered in LPF2, which leads to a good extinction of the f_1 signal.

Signals of frequencies $| f_1 - f_2 |$ and $f_1 + f_2$, resulting from (M1,M2) interference events, experience attenuation from BPF2 only. This attenuation is much smaller than the attenuation of the f_1 component and may be thought of as potentially presenting a problem. However, this is not an issue for our set of conditions since the scan ranges covered by TS1 and TS2 are less than half of the initial OPD between the two mirrors, and therefore light returning from mirror M1 is never coherent with light returning from mirror M2 ($d_{12} \neq 0$ at all times).

Two storage oscilloscopes, MO1 and MO2 and two counters SSC1 and SSC2 are used to assist in interpreting and measuring the coherent reflectograms returned by each interferometer. The counters are triggered by the leading edge of the incoming pulses (interference events) and provide an immediately available estimation of pulse separation in the time domain, which is converted into the spatial interval between the corresponding interfaces.

3.4.6 Experimental results

Figure 3.25 shows the result of performing a long scan of translation stage TS1 with mirror M1 attached. Within the same scanning movement (i.e. without stopping or changing direction), mirror M1 coherently matches the positions of the front and back of the eye model. This permits a straightforward determination of the eye length, which is illustrated by the annotations of Figure 3.25. The horizontal time scale of the oscilloscope display was converted to a distance scale using the known 10 mm/s velocity of the TS1 translation stage. In order to simplify the interferogram, the model eye was misaligned on purpose so that only one pulse is reflected from its front face.

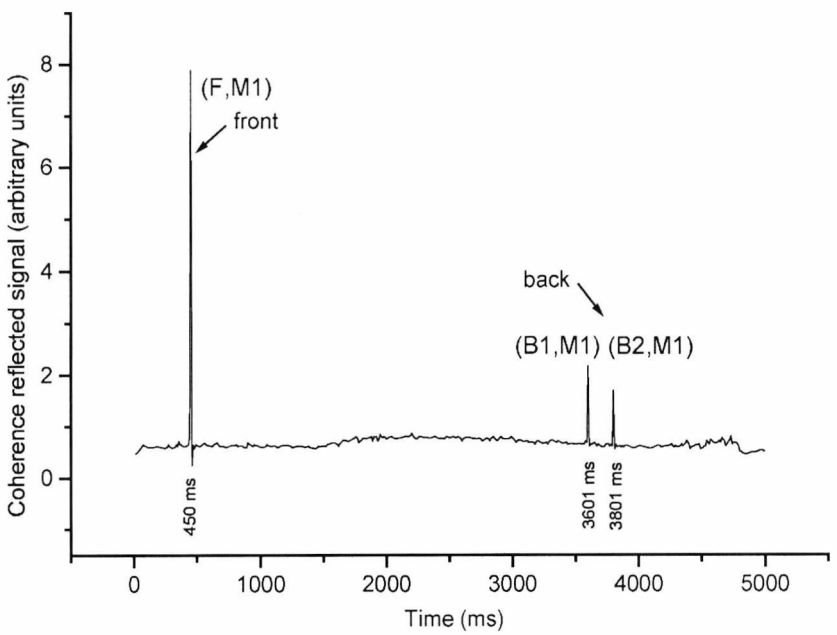

Figure 3.25 PD1 reflectogram obtained by moving mirror M1 for 5 cm at 10 mm/s speed.

The starting point of mirror M1 is chosen such that during the scan the reference arm OPD matches both the OPD corresponding to the front and the back of the flask. The MO1 timebase was triggered by the synchro software generated spike.

The first peak, (F,M1), corresponds to the air-lens interface with all other contributions from lens-air, air-flask, flask-air (air in the flask) having been suppressed intentionally through careful alignment. However, the back wall of the flask provides two reflection events, denoted B1 and B2. B1 corresponds to the anterior surface and B2 to the posterior surface of the flask wall. By adjusting the trigger thresholds for the A and B counter inputs, the time interval between (F,M1) and the first peak from the back, (B1,M1) was found to be 3151.5 ± 1.2 ms, corresponding to 31515 ± 12 μm.

The profile in Figure 3.25 was generated in a scan lasting longer than 5 s. It should be noted that a long time is spent scanning over a length which has no particular relevance for the eye length since the only areas of interest are the front and the back of the model eye.

In an attempt to reduce the measurement time, the range corresponding to the entire eye length was divided into two smaller ranges overlapping the regions of interest with translation stage TS1 covering one range and TS2 the other. With a shorter scanning time, the errors introduced by the eye movement would be smaller. In addition, when the signal is weak, a lower bandwidth is needed in order to improve the signal to noise ratio, and taking into account the proportionality between velocity and bandwidth stated in equations (3-16) and (3-17), the speed should be accordingly reduced which illustrates the trade-off between the measurement speed and the signal to noise ratio. Consequently, range division brings a second advantage: it allows reducing the scanning time without the need to increase the bandwidth.

A range of a few mm for each scan should suffice but the translation stages require time to reach the set velocity and then to come to rest, which translates into extra movement outside the useful range.

A software generated voltage spike at the beginning of each translation stage movement was used to provide the synchronising signal acting as reference for time measurements. Translation stage TS1 was set to travel at 10 mm/s and TS2 at 26.7 mm/s. The model eye was replaced with a mirror M3 and the time interval $t_{1\,exp}$ ($t_{2\,exp}$) between the synchronisation pulse and coherence event (M3,M1) ((M3,M2)) was measured as a function of the M3 position. The translation stages execute scans consisting of an away and a return journey, with the stages always returning to rest at their starting point. Coherence events such as (F,M1),..., (B,M2) etc. are only registered during the away journey when the stages are moving away from the fibre ends.

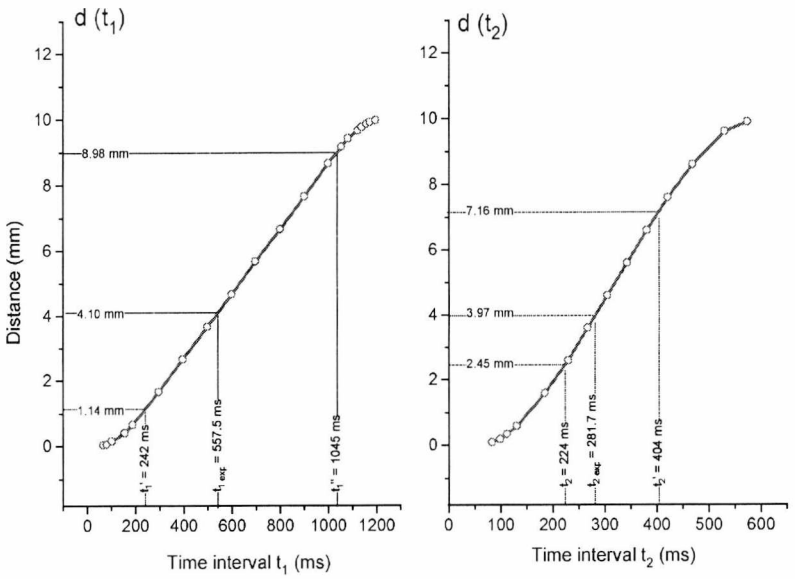

Figure 3.26 Position of translation stage vs. time when the speed is set at 10 mm/s (left) and at 26.7 mm/s (right). In both cases, the translation stages move over 10 mm.

The positions of the stages against time, $d(t_1)$ and $d(t_2)$ were then inferred, as shown in Figure 3.26. Performing the differentiation of $d(t_1)$ and $d(t_2)$, the dependence

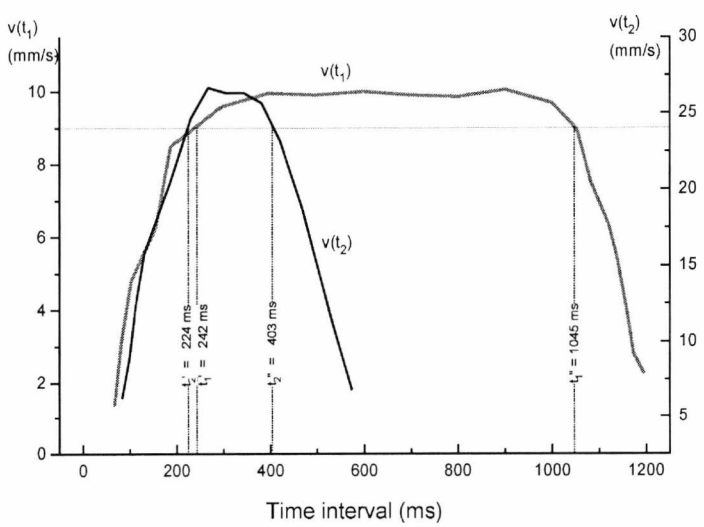

Figure 3.27 Translation stage speed dependence on time. The curves represent the differentiation of the graphs in Figure 3.27.

of translation stage velocity with time, $v(t_1)$ and $v(t_2)$, shown in Figure 3.27, was obtained. As seen in Figure 3.26 and Figure 3.27, both sets of graphs exhibit non-linear dependence.

The data in Figure 3.27 shows that a time interval $t_1' = 242$ ms is taken at the beginning (and a similar time interval at the end of the scan) for the speed to build up to 90% of a 10 mm/s set velocity. Similarly, for a velocity of 26.7 mm/s, a ramp time $t_2' = 224$ ms is needed. This means that in order to obtain a linear dependence of position with speed, the features of interest should be placed within the central part of the scan, avoiding a subdivision of $d_1' = 1.14$ mm for a stage velocity of 10 mm/s (maximum of 1.14 and 1.02 from the graph in Figure 3.26 left) and $d_2' = 2.84$ mm (maximum of 2.45 and 2.84 from the graph in Figure 3.26 right) for a stage velocity of 26.7 mm/s at both ends of the scan. Consequently, for a scan of length L = 10 mm, the useful range, in which the speed is at least 90% of the steady state value, is approximately $r_1 = L - 2d_1' = 7.72$ mm for the 10 mm/s speed and only $r_2 = L - 2d_2' = 4.32$ mm for 26.7 mm/s (Figure 3.26).

The region corresponding to the back of the model eye was scanned with TS1 at $v_1 = 10$ mm/s and the one corresponding to its front with TS2 at $v_2 = 26.7$ mm/s giving $f_1 = 24$ kHz and $f_2 = 64.3$ kHz. The higher the difference between f_1 and f_2, the higher the attenuation of the signal at f_1, introduced by BPF2. With the quality factors of NF and BPF2 set on Q = 5 and Q = 20, respectively, an overall attenuation of more than 60 dB was achieved for the signal at f_1. This was evaluated in comparison with the signal at f_2, by measuring the amplitudes of the two signals of frequencies f_1 and f_2 at the IA output and R2 input.

Data shown in Figure 3.26 and Figure 3.27 is obtained for a 10 mm long scan with each stage. With the model eye back in the object arm, the following operations were carried out.

(1) the starting point of TS2 was adjusted to make the (F,M2) coherence event occur anywhere in the linear region of the TS2 scan range, preferably in its middle section;

(2) scanning TS1 with TS2 at rest, coherence event (M1,M2) was found at position p_2. The value of p_2 was obtained from the digital driver display of TS1;

(3) the starting point of TS1 was adjusted to make the (B1,M1) coherence event occur anywhere in the linear region of the TS2 scan range, again preferably in its middle section. Then, with TS1 at rest, position p_1 was obtained from the digital driver display of TS1. The path imbalance between mirrors M1 and M2 at rest was found to be $d_{12} = p_1 - p_2 = 31390$ μm.

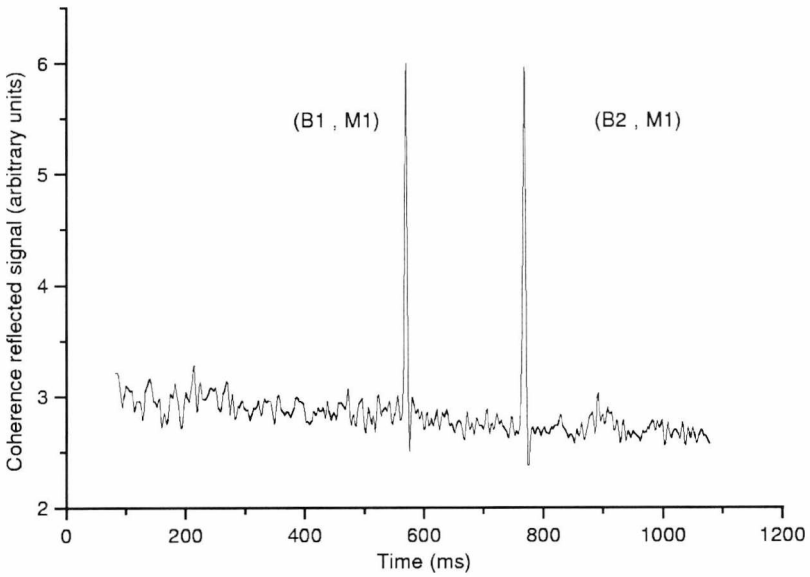

Figure 3.28 PD1 reflectogram obtained by moving mirror M1 for 1 cm at speed 10 mm/s. The start point of the mirror M1 is such that, during the scan, the reference arm OPD1 matches the back of the flask only. The MO1 timebase was triggered by the synchro spike.

The profile in Figure 3.28 was obtained by scanning TS1. The time interval between the synchronising spike and peak (B1,M1) was determined using counter SSC1 as $t_{1exp} = 557.5 \pm 0.8$ ms.

Figure 3.29 shows the reflectogram obtained by scanning TS2, where event (F,M2) represents the front part of the reflectogram in Figure 3.25, this time obtained at a different speed. The time interval between the synchronising spike and the peak was found to be $t_{2\,exp} = 281.7 \pm 0.5$ ms, using counter SSC2. The positions of the two interfaces corresponding to peaks (F,M2) and (B,M1) are determined from Figure 3.26 as $d(t_{1\,exp}) = 4101 \pm 8$ μm and $d(t_{2\,exp}) = 3972 \pm 9$ μm. The desired distance d is then:

$$d = d_{12} + d(t_1) - d(t_2) = 31390 + 4101 - 3972 = 31519\ \mu m \qquad (3\text{-}21)$$

which is in good agreement with the value d = 31515 μm obtained from Figure 3.25.

However, if the time non-linearity exhibited by the translation stage velocity is ignored, a rough estimate gives: $d(t_1) \approx (\text{steady state velocity})_1 \times t_{1\,exp} = 5.575$ mm and $d(t_2) \approx (\text{steady state velocity})_2 \times t_{2\,exp} = 7.520$ mm. This would introduce an error of about 2 mm in comparison with the distances obtained from the graphs in Figure 3.26 as above.

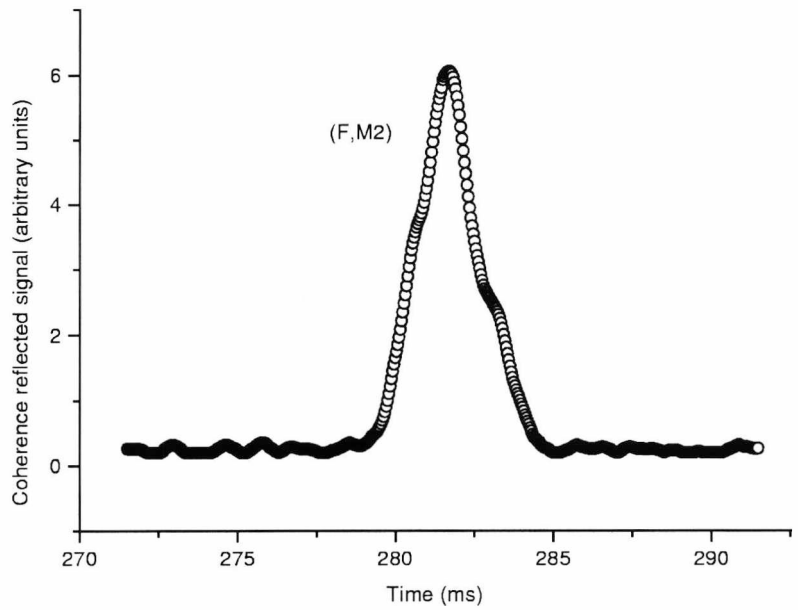

Figure 3.29 PD2 reflectogram obtained by moving the mirror M2 for 1 cm at 26.7 mm/s speed. The start point of the mirror M2 is such as, during the scan, the reference arm OPD2 matches the front of the flask only. The MO2 timebase was triggered by the synchro software generated spike.

These errors should be comparable with the minimum theoretical error achievable when determining the position of the peak of the envelope of the correlation function in white light interferometry (ignoring the information in the fringe pattern), as is the case with the method presented here. Individual measurements can in principle be made using the displayed position of the translation stages TS1 and TS2, accurate up to 1 μm. Assuming that a variation of 10% from the peak of the correlation function supposedly of Gaussian profile (with FWHM = 31 μm) could be detected, each interface can be measured with an error $\varepsilon = 7.9$ μm either side. As the number of interfaces considered in (3-19) is 3, the minimum eye length error is $\varepsilon_{min} = \sqrt{3}\varepsilon = 13.7$ μm.

Obviously, the errors in the set-up may be higher than the value above. Additional errors may arise from the following sources:

1) Pulse amplitude variations relative to the fixed level of the thresholding circuits used in the time difference measurements and the width of reflected pulses. In the most unfavourable case, this cumulative error cannot be larger than $\varepsilon 1 = \sqrt{2}(lc/2) = 21.86$ μm ($\sqrt{2}$ is the consequence of the calculation based on two pulses);

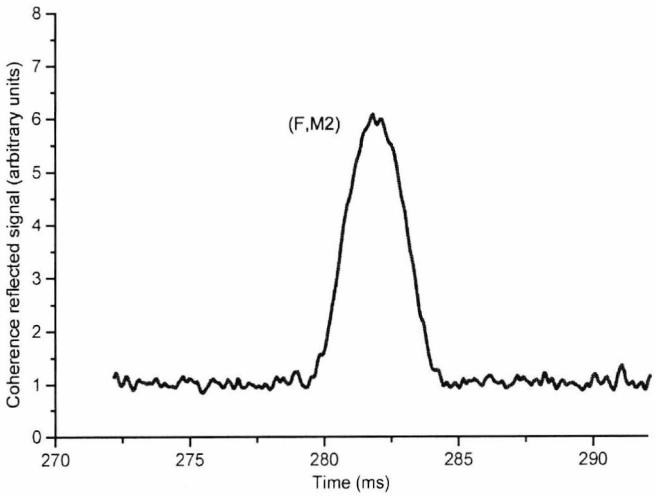

Figure 3.30 Superposition of the reflectogram in Figure 3.29 for 100 repetitions.

2) Conversion errors from time to distance via the calibration graphs in Figure 3.26. In principle, using 1 μm steps, a good accuracy in distance is ensured. When measuring the time interval for calibration, an error of magnitude ε_1 should again be considered. Consequently, a maximum experimental overall error of $\varepsilon_{max} = \sqrt{2\varepsilon_1^2} =$ 30.9 μm results.

Figure 3.30 shows the same profile as Figure 3.29, where the peak (F,M2) was superimposed onto itself for 100 repetitions. This demonstrates a good reproducibility of the interval measurement between the software generated spike and any coherence signal received from the test object.

3.4.7 Measurements of various eye lengths

For a given range L and positions p1 and p2, the retina will return a coherent signal only when placed in the range [p1 + d1', p1 + L - d1'] and the cornea will return a coherent signal only when placed in the range [p2 + d2', p2 + L - d2']. Consequently, the minimum measurable eye length is:

$$d_{min} = d_{12} - L + d_1' + d_2' = d_{12} - \frac{r}{2} \qquad (3\text{-}22)$$

and the maximum measurable eye length is:

$$d_{max} = d_{12} + L - d_1' - d_2' = d_{12} + \frac{r}{2} \qquad (3\text{-}23)$$

where r represents the variation in measurable eye length acceptable by the set-up within which the stage velocity is at least 90% of the steady state value:

$$r = d_{max} - d_{min} = r_1 + r_2 = 12.04 \text{ mm} \qquad (3\text{-}24)$$

The operator should ensure that the two time intervals, $t_{1\,exp}$ and $t_{2\,exp}$ are within the interval $t_{1,2}' < t_{1,2\,exp} < t_{1,2}''$ (Figure 3.27). If, however, at least one of the experimental values falls outside this interval, position p_1 or p_2 or both should be altered. This is also the case when no signal is obtained (eye too short or too long, such that retina, cornea or both are outside the L range). A number of pre-set values of p_1, p_2 and consequently d_{12} can be provided to cover different eye length ranges.

3.4.8 Remarks

A solution for electronic processing has been presented to attenuate the signal corresponding to the coherence signal from the first interferometer by more than 60 dB at the output of the channel processing the signal from the second interferometer. Although the set-up has not completely separated the eye length measurement from the eye movement (also a drawback of its bulk counterpart [54]), it has reduced the weight of this type of measurement error by significantly reducing the time needed to locate the positions of the front and the back of the eye. For a 10 mm scan, the non-linear characteristic of the displacement versus time of the translation stages limits the range of eye lengths to $d_{12} \pm 6.02$ mm. However, by changing d_{12} (the path imbalance between the mirrors), any eye length can in principle be accommodated.

The configuration presented in detail in paragraph 3.4 gives the possibility of simultaneously displaying reflectograms for two regions in the eye. The technique is not restricted to the eye and may equally be applied to investigate features inside the volume of any multi-layer object. Taking into account the inaccuracies in measuring time intervals with the counters, when the start and stop pulses have finite widths determined by the correlation function profile, an eye length measurement accuracy of 30.8 μm results.

The procedure may prove useful in the process of optical adjustment to ensure that both signals have sufficient amplitude, as the adjustment may enhance one signal at the expense of the other. In order to make this adjustment in one long scan covering

the entire eye length, too high a speed for the translation stage would be needed to ensure that the front and the back of the eye are seen at an interval less than 1 s. When a more complex method is sought, like that involving the interference of the signals from the back and the front, the method presented here represents a necessary preliminary step.

4. The Newton rings sampling function technique

4.1 Introduction

The principles and practical implementation of low coherence depth profiling at a single point on the surface of an object were examined in the previous chapter. A simple way of extending the profiling to three dimensions and essentially produce a surface (topographic) or volume (tomographic) depth profile is to repetitively apply the one dimensional distance measurement for a number of locations on the target surface. In order to build a depth map, the investigation beam must be directed to each of these locations, sequentially, with the aid of a scanning device.

The previous chapter has examined how the linear modulation, or scanning of the interferometer's optical path difference (OPD) generates an interference signal whose maximum is uniquely associated with a target reflector's longitudinal position. In the opening paragraph of this chapter the focus will be on how a periodic modulation of the OPD with amplitude on the scale of the wavelength of light has a similar effect, in that it produces a Gaussian profile of the rectified interferogram.

4.2 Micron amplitude phase modulation

The procedures employed in the depth profiling of multi-layer structures described in Chapter 3 are all based on a continuous longitudinal scan that explores the entire coherence region. Aside from the fact that this type of scanning necessitates specialised and often costly equipment (translation stages with optimised linear movement) there are situations when a continuous scan is not practicable and / or it would be advantageous to explore the coherence in discrete steps or to measure the coherence signal over a narrower depth interval.

As demonstrated earlier, a variation of the optical path difference over a range comparable to the extent of the coherence region is the key to obtaining a variation of the interference signal at the interferometer output. Path modulation in the form of a

continuous longitudinal scan leads to an output which can be described by the auto-correlation profile of the source modulated by a sinusoidal signal. This signal can be processed in real time with a bandpass filter to extract the Gaussian envelope and its maximum, i.e. the position of maximum coherence. To obtain the spatial coordinate of the interference location, knowledge about the spatial encoder of the scanning device is required.

The interferometer output should theoretically be the interferometer transfer function (shown in Figure 2.2) under any circumstances, regardless of the speed at which the fringe pattern is sampled. For reduced speeds, as the time span necessary to complete a scan through the coherence region increases, the temporal frequency of fringes in the interferometer's output decreases, but the fringes' spatial frequency remains constant and therefore a step by step longitudinal scan carried out in sufficiently small steps, with pauses between steps, should theoretically yield the same DC spatial fringe pattern output as a fast scan, despite the longer acquisition time.

However, due to the difficulty in maintaining a good interferometer stability for a fiberised set-up subject to slowly varying environmental parameters (of which temperature and moving currents of air are the most frequently encountered in laboratory conditions) slower or stepped OPD variations lead to patterns affected by significant levels of noise.

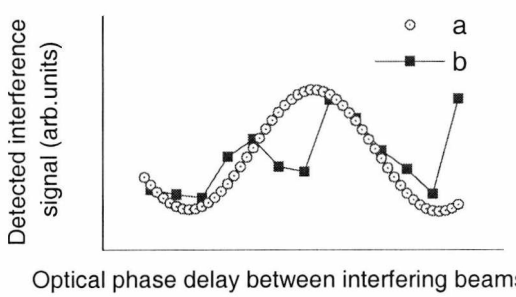

Figure 4.1 Fringe detail in the transfer function (a) fast scanning case (b) fine stepped positioning case

Figure 4.1 shows a comparison between the aspect of a fringe detail in the experimentally measured transfer function for a) continuous sampling at a scan speed of 2 cm/s and for b) discrete sampling in the case of longitudinal positioning followed by a measurement of the DC signal level corresponding to each discrete position (a PZT device was used to achieve steps of 100 nm). It is noticeable that the noise introduced in the recovered signal is significantly increased by DC level detection.

Since the DC measurement of the interference signal level at an arbitrary longitudinal position is not by itself sufficient to gauge the fringe amplitude, a simple and widely used procedure for obtaining fringe amplitude information at a desired longitudinal location is to apply a dither to the interferometer path difference. The dither, whose amplitude is roughly equal to the wavelength of light used, would take the signal through at least a minimum and a maximum. The fringe amplitude is simply recorded as the peak - peak value of the resulting AC signal. The entire fringe pattern can be measured through such a combination of stepped longitudinal positioning accompanied by phase dither. A fringe pattern can be measured by applying this procedure at a number of locations and building up a table of correspondence between the fringe amplitude and the longitudinal position, the resulting output being identical with the one obtained through the scan and rectification procedure.

Operation in a stepped longitudinal positioning mode can be important in short range depth profiling operations and offers the possibility of bandpass filtering the output signal at chosen frequencies. Dithering is commonly achieved by vibrating the reference mirror with a longitudinal scan amplitude comparable to the wavelength of light used.

4.3 Path modulation through axis-centred lateral beam scanning. Non-displaced beam case

The discussion above with respect to the possibilities of carrying out path modulation is solely with regard to the case of modulation in interferometers used in one-dimensional imaging.

For the case of two or three-dimensional imaging, the use of beam deflection instruments in the object arm opens up the possibility of using lateral beam positioning to generate path modulation. This procedure is investigated in the rest of this chapter.

4.3.1 Dynamic beam deflection

The operation of beam deflection instruments such as polygon and galvanometer scanning mirrors has been briefly reviewed in paragraphs 2.2.1 and 2.2.2.

Such devices are essentially transducers that enable some form of angular deflection in response to an applied electrical signal. In general the angular deflection is a linear function with applied voltage and this is the case of the galvanometer

scanning mirror pair type GS 120 T which, as well as enabling static positioning of the object beam, can produce a dynamic beam scan on the target surface.

4.3.2 Coherence surface arising from beam deflection

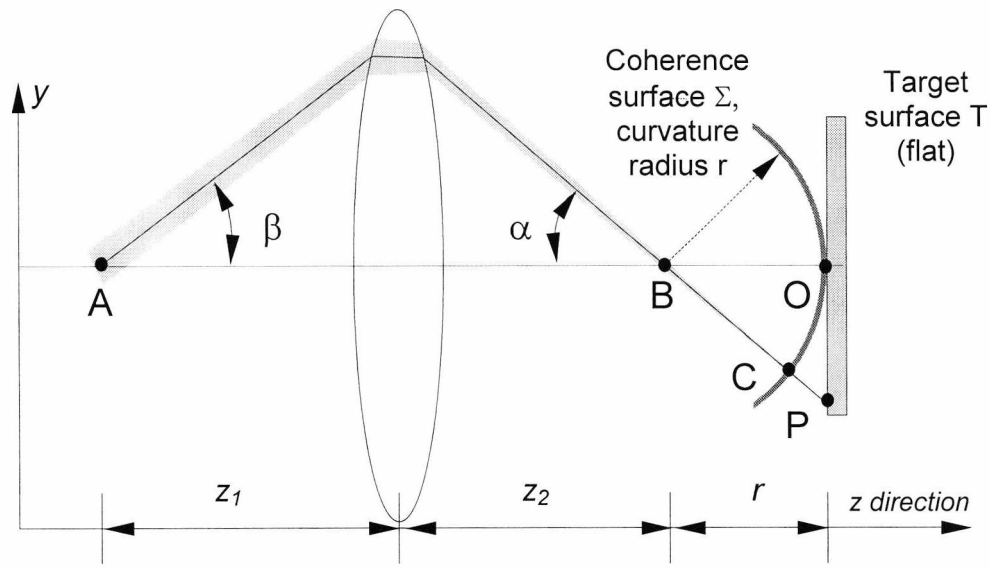

Figure 4.2 Object arm. A: beam deflection point, B: conjugate point to A and centre of curvature of the coherence surface Σ

The geometry of a ray fan directed at a flat target is depicted in the diagram in Figure 4.2. The beam is assumed to have arrived at A after having emerged from an optical component set which in combination with lens L causes it to be focused on the target surface T. The cross section of the object arm contains the deflection point A where the beam is incident on the mirror, the optic axis of the system (z) and a section of the target object. Beam deflection is assumed to be caused only by rotating the Y mirror and therefore restricted to the y-z plane (of the diagram). In this geometry the beam is incident on the deflecting mirror on its axis of rotation and to distinguish this situation from a different case treated further in this chapter, this configuration is referred to as the Non-Displaced Beam geometry (NDB).

For simplicity, the portion of the beam prior to point A and the deflection mechanism are not represented in the diagram. The grey representation of the beam is its section contained in the plane of the diagram. The beam is focused onto the plane of the target.

The coherence phenomena resulting from the deflection of the beam by up to an angle β measured either side of the optic axis of the system are examined. The simplest case of a collimating arrangement consisting of a single collimating lens L

(convergent) is considered first. The lens is assumed wide enough to accommodate the entire optical deflection field generated by the galvanometer scanner.

4.3.3 Fringe pattern arising from beam deflection

With reference to the diagram in Figure 4.2, from the necessary condition that the conjugate point of A is B one can deduce that the optical path lengths of all the reflected rays measured between A and B are equal [57].

A coherence surface Σ can be defined as the three dimensional locus of those points situated at an optical distance from A equal to the optical length of the reference arm. The assumption is made here that this length is set such that the target surface, the coherence surface and the optic axis intersect in point O.

The coherence surface Σ has the shape of a sphere of radius r, centred in B. For an angle β for which the target is intersected in P, the beam undergoes a partial specular reflection and backscatter towards B with the reflected light directed towards A in a reciprocal manner such that the combined onward and return journey is along the route A-B-P-B-A.

This arrangement is implemented in the object arm of a standard Michelson interferometer. As the deflection angle β changes, the position of the mirror in the interferometer's reference arm is kept constant, such that at any instant the reference beam travels the equivalent of an optical distance equal to A-B-O-B-A (in a straight line along the optic axis).

If the target beam intersects the coherence surface in C, the optical path difference (OPD) between the target and the reference beams can be expressed as:

$$\mathrm{OPD} = 2(\mathrm{BP} - \mathrm{BC}) = 2\left[\frac{r}{\cos\alpha} - r\right] \tag{4-1}$$

For small values of α, $\cos\alpha$ can be approximated with:

$$\cos\alpha = 1 - \frac{\alpha^2}{2} \tag{4-2}$$

By retaining the first two terms from its series expansion, and since $1/(1-\alpha^2/2)$ can be written as:

$$\frac{1}{1-\frac{\alpha^2}{2}} = 1+\frac{\alpha^2}{2}+\frac{\alpha^4}{4}+\frac{\alpha^6}{8}+\ldots \tag{4-3}$$

we have:

$$\frac{r}{\cos\alpha} = \frac{r}{1-\frac{\alpha^2}{2}} = r\left(1+\frac{\alpha^2}{2}+\frac{\alpha^4}{4}+\frac{\alpha^6}{8}+\ldots\right) \cong r\left(1+\frac{\alpha^2}{2}\right) \tag{4-4}$$

therefore

$$OPD(\alpha) \cong 2\left[r\left(1+\frac{\alpha^2}{2}\right)-r\right] = r\alpha^2 \tag{4-5}$$

From the geometry of rays in Figure 4.2 it is apparent that

$$z_1 \tan\beta = z_2 \tan\alpha \tag{4-6}$$

and if the approximations $\tan\alpha \cong \alpha$ and $\tan\beta \cong \beta$ are used (scan angles α and β assumed small),

$$z_1 \beta = z_2 \alpha \tag{4-7}$$

which leads to the following expression for the OPD in terms of β and the distances z_1 and z_2:

$$OPD(\beta) = r\frac{z_1^2}{z_2^2}\beta^2 \tag{4-8}$$

The detected signal registers maxima and minima as the angle β (and implicitly α) is varied. Maxima are obtained when

$$\Delta OPD = 2k\frac{\lambda}{2} \tag{4-9}$$

where k is an integer. From (4-1) and (4-9), the angle $\delta\beta$ measured between two adjacent rays passing through A and corresponding to two interference maxima can be expressed in terms of the angle $\delta\alpha$ measured between the same rays passing through B as:

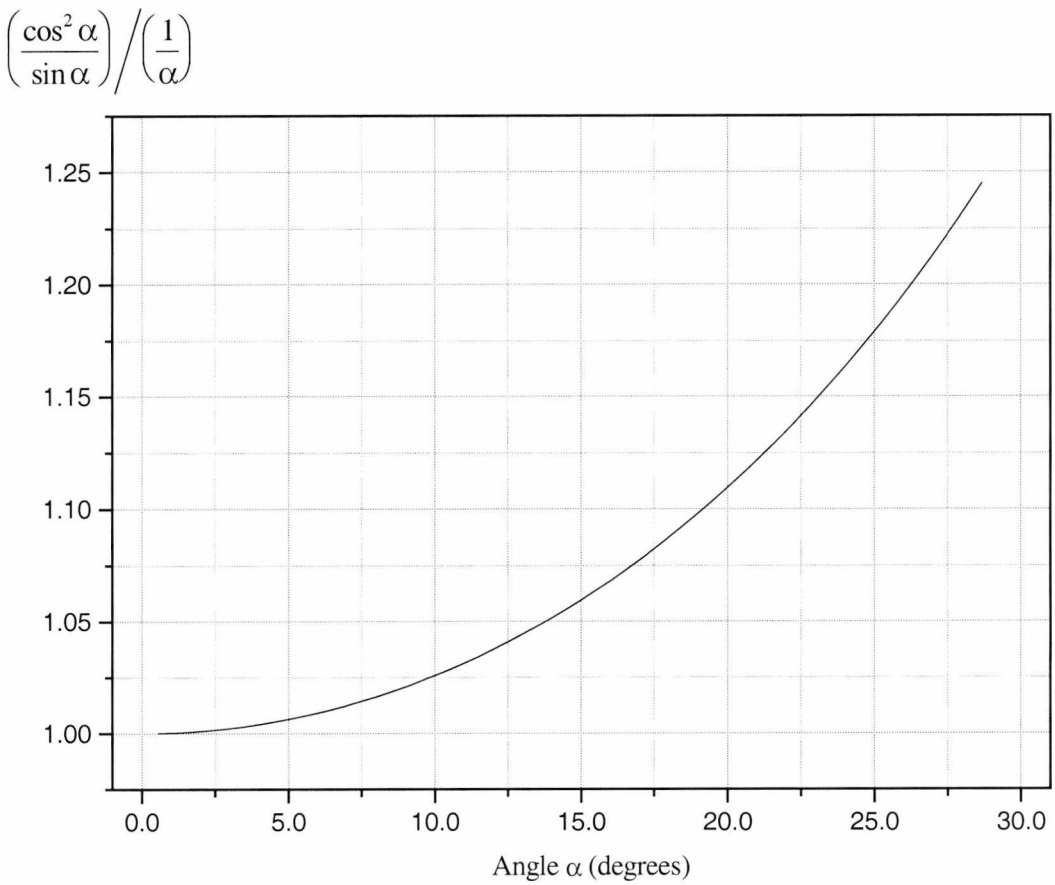

Figure 4.3 Illustration of the domain for the angle α where $\left(\frac{\cos^2\alpha}{\sin\alpha}\right)$ can be approximated with $1/\alpha$

$$\delta\beta = \frac{z_2}{z_1}\delta\alpha = \frac{z_2}{z_1}\frac{\lambda\cos^2\alpha}{2\,r\sin\alpha} \approx \frac{z_2}{z_1}\frac{\lambda}{2\,r\,\alpha} \qquad (4\text{-}10)$$

It is important to note that the final approximation in equation (4-10) is only valid for small angles, as are the previous two approximations in equations (4-4) and (4-8). The value of the ratio between the function $\cos^2\alpha$ / $\sin\alpha$ and its approximation $1/\alpha$ is plotted against α in Figure 4.3 to show the extent of the domain where the approximation holds. It can be seen from the graph that for values of α smaller than 14 degrees the error introduced is below 5% but it should be noted that as the limits of

the angular scan are increased the spacing between maxima would be larger than the theoretically predicted value based on the approximation discussed above.

4.3.4 Modulation of the beam deflection angle

It is clear that some form of variation of the fringe pattern can be expected when the two beams, target and reference, recombine, due solely to the path difference introduced in the process of lateral scanning. Particular interest presents the case when the angle β is modulated in a controlled fashion, thereby giving rise to a modulated interference signal.

This case can be examined by applying a triangular waveform to either one of the mirrors MX or MY, which produces a deflection β linear with time, t, within the waveform period T:

$$\beta(t) = \beta_{max}\left(-1+\frac{2t}{T}\right) \tag{4-11}$$

The time span δt elapsed between the detection of two maxima can be obtained from equations (4-1) to (4-11). The corresponding fringe frequency f will be:

$$f = \frac{1}{\delta t} = 2\beta_{max}\frac{z_1}{z_2}\frac{r\,\alpha}{\lambda}F \tag{4-12}$$

where F is the frequency of the waveform applied to the galvanometer scanning mirror.

4.3.5 Comparison with longitudinal scan path modulation

It is instructive to compare this relation to the one obtained for the fringe frequency in the case of a longitudinal scan set-up for one-dimensional measurements in which the reference mirror is moved at a constant speed, v. In this case, the frequency of the Doppler signal amounts to:

$$f = 2\frac{v}{\lambda} \tag{4-13}$$

which in the case of *en face* scanning leads to a speed equivalent value v given by:

$$v = \beta_{max} \frac{z_1}{z_2} r \alpha F \tag{4-14}$$

The presence of the angle α in the above formula is significant since α is the angle subtended by the target point from the optic axis and therefore the speed equivalent value v will depend on the position of the beam spot on the target. The constant is not an invariant and locations wide of the optic axis can therefore be expected to produce fringes of a different spacing compared to those near the axis. Because the angle α is actually a measure of the divergence of the target surface from that of the coherence surface, it is correct to say that the frequency of lateral-scanning-induced modulation is dependent on the angle of incidence of the probing beam to the target surface.

4.3.6 Newton's rings on the surface of a flat target

The geometrical locus of the points on the target surface T fulfilling the condition for interference maxima (condition expressed in (4-9)) consists of rings of radius R_k. In the diagram in Figure 4.2 the segment OP coincides with the radius of such a ring:

$$R_k = \frac{2r + k\lambda}{2} \sqrt{1 - \left(\frac{2r}{2r + k\lambda}\right)^2} \tag{4-15}$$

For small angles and a low ring order k, (4-15) becomes:

$$R_k \approx \sqrt{k\, r\, \lambda} \tag{4-16}$$

which shows that the locus of interference maxima is given by a similar relation to that describing Newton rings (usually observed when beams reflected from a hemisphere resting on a flat surface and from the flat surface interfere).

The coherence length of the source used for illumination limits the extent of the Newton rings obtained by lateral scanning. For a source coherence length l_c, the target area covered by rings is a disk of an area A given by:

$$A \approx \frac{\pi}{2} l_c r \tag{4-17}$$

As opposed to the classic Newton rings experiment, the interfering rays producing Newton rings in the lateral scanning arrangement originate in two different arms of the interferometer. If the reference arm length is though of as the equivalent of the distance to the surface Σ for any scan angle β, the interfering rays are coincident in direction (PBA and CBA). However, Newton's rings are treated in various Optics textbooks as obtainable from rays not necessarily superimposed throughout their trajectories [57], [58]. In addition this experiment does not produce the phase difference of π encountered in the classic Newton's rings situation. In the classic experiment the phase difference between rays reflected off the plane and hemisphere is π due to the phase change of 0 at the hemisphere and the phase change of π for light reflected off the flat surface.

4.3.7 The set of Newton rings as a sampling function

The previous paragraphs show how the flat target is essentially "sampled" by a sampling function which consists of concentric rings of variable thickness and of finite extent (in the case of low coherence illumination), centred on the optic axis. The origin of the sampling function is the interference-related effect of the ever increasing deviation with the scan angle of the optical path difference between the (imaginary) coherence surface Σ and the target surface T.

The interferometric arrangement can therefore be reduced to just the sampling function superimposed on the target surface. An image can be created in the form of a plot of intensity along the spatial co-ordinates as the object beam maps across the sampling function, returning an intensity modulated fringe pattern of frequency f given by (4-12).

4.3.8 Effect of a rough target surface

For the case when irregularities are present on the target surface, a scattering surface feature situated in the coherence region will produce a well defined fringe only if its size is sufficiently large to give rise to two consecutive maxima, i.e. if its angular size measured from point B is larger than $\delta\alpha$. From an imaging point of view this sets the minimum feature size which can be resolved with this particular device.

The effect of a non-negligible target roughness is to add a further modulation to the ac signal. A scattering feature located at a certain angular position α gives rise to a

signal peaking at frequency f. The peak can be enlarged due to: (a) the rough profile of the target which acts as a random modulation factor and (b) to the extension $\Delta\alpha$ of the scatterer, according to relation (4-12) (the frequency spread Δf increases in proportion to the spatial extent $\Delta\alpha$).

In order to reduce the relative frequency spread $\Delta f/f$ it is recommended that the sampling function regions of lower frequencies are not used, i.e. the features to be scanned should be placed within regions where the rings are closely spaced.

This however results in a lower image contrast, as explained in the following paragraph, so this adjustment involves a trade-off between the contrast and the bandwidth of the photodetection circuit.

4.3.9 Experimental arrangement

The experimental set-up used to investigate path modulation through lateral scanning is shown in Figure 4.4.

Light from a pigtailed superluminescent diode SLD enters a single mode directional coupler DC. The output fibres of the coupler form a Michelson interferometer. One arm (the reference) consists of a microscope objective C1 and a mirror M mounted on a micrometer translation stage TS. The other arm (sensing) consists of the microscope objective C2, scanner SXY, the lens L1 and the object under test (OUT).

Two triangle waveform generators TX and TY are used to drive the two mirrors MX and MY of the scanner block SXY. The value of the galvanometer scale factor for the two mirrors is $\gamma = 4°/V = 69.81$ mrad/V.

The signal arriving at photodetector PD is amplified and band-pass filtered in the circuit BPF before being applied to the input of a high voltage amplifier and subsequently to the "z modulation" input of the analogue storage oscilloscope ASO.

The oscilloscope is effectively used as an imaging system. An intensity image of a size proportional to that of the illuminated target area appears on the oscilloscope screen as the luminous spot is deflected along the vertical and horizontal directions by signals proportional to those driving mirrors MX and MY. The brightness of the luminous spot is proportional to the z input of the oscilloscope.

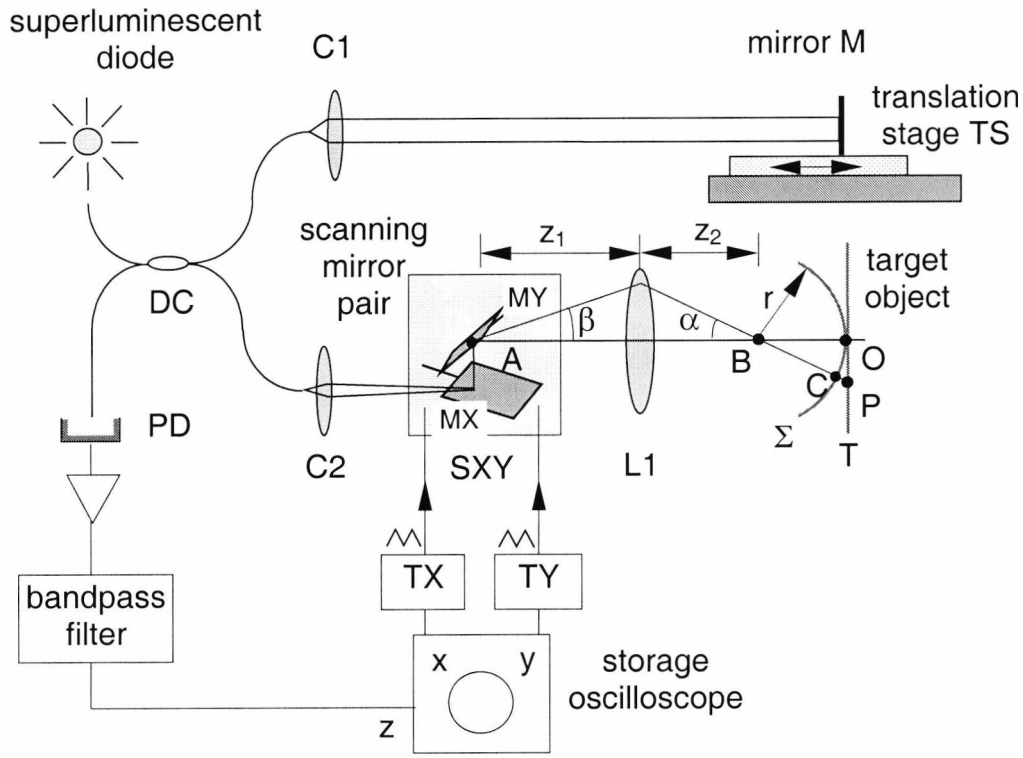

Figure 4.4 Experimental arrangement for *en face* OCT [59]: C1, C2: collimators; DC: directional coupler; L1: lens; PD: photodetector; SXY: galvanometer scanning mirror system; MX, MY: scanner mirrors; TX, TY waveform generators;

The triangle waveform modulation applied to mirror MX, combined with a triangle waveform modulation of a smaller frequency applied to mirror MY, produces a beam scan in a pattern similar to a raster of a zigzag type (stepping MY would result in a true parallel raster pattern). These scan patterns are illustrated in Figure 4.5.

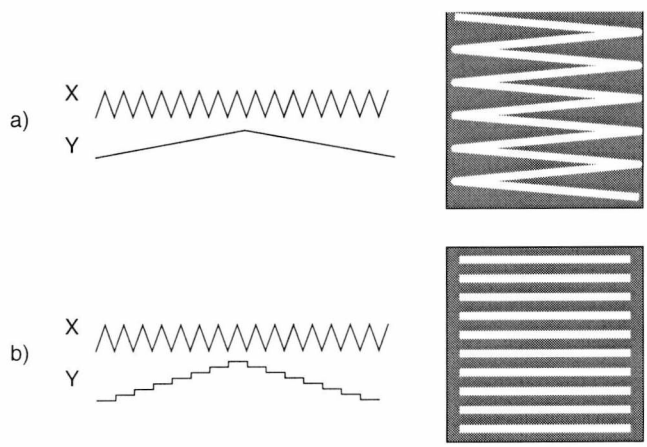

Figure 4.5 Illustration of the scanning pattern generated by the application of the triangle waveform to the X mirror accompanied by a Y mirror movement generated by a) a triangle waveform and b) a step waveform

Since mirror MY is moving typically 1-2 orders of magnitude slower than mirror MX, for practical purposes the relations deduced in earlier paragraphs need not take into account the frequency of oscillation of the slower mirror.

Taking advantage of the long persistence screen memory capability of the oscilloscope, a complete raster may be obtained even when the generators TX and TY are not fully synchronised. The collection of images can be carried out in two modes, either as one shot or dynamically. One shot imaging requires the freezing of the display after a complete raster is obtained (with the memory set on infinite persistence); dynamic imaging requires adjusting the rate of screen memory loss to a value which allows a complete raster to be covered; in this manner *en face* coherence images are obtained and are being refreshed continuously as the depth of the object is explored (by adjusting the position of TS).

4.3.10 Experimental results

The assumption was made in the earlier theoretical treatment that the diameter of the focused spot on the target surface is much smaller than the separation of two consecutive maxima. In order to ensure that this is the case and to improve the transversal resolution, another lens, L2, of 2.5 cm focal length, is placed at point B. The previously obtained relations are still valid but r needs to be replaced by L_2, the focal length of lens L2. The frequency of the signal driving the horizontal scanner is kept constant at F_x = 20 Hz (waveform generator TX) and the frequency of the signal applied to the vertical scanner (waveform generator TY) is F_y = 0.5 Hz. The amplitude of both signals is 0.8 V, which ensures the spot covers a 3×3 mm area in the zigzag fashion indicated in Figure 4.5a.

The Newton rings pattern seen on the oscilloscope display may be centred on the display grid by adjusting the positions of the collimator C2, lens L1 and L2. The centred pattern obtained from a plane mirror target, with the reference arm coherence matched with the sensing arm and no band pass filter after the photodetector is shown in Figure 4.6.

The centre of the rings can subsequently be moved outside the displayed area by slightly shifting collimator C2 vertically or horizontally. This will obviously increase the astigmatism, however the relative spread of frequencies Δf will be smaller and this aspect is more important for obtaining a better signal to noise ratio.

The superluminescent diode used in this experiment has a 20 nm source line width centred at λ = 830 nm. The experimentally determined coherence length is found from the analysis of the visibility of the interferogram in Figure 4.6 to be 70

μm. This is significantly longer than the theoretical prediction and is due to the effects of imbalanced dispersion (one fibre arm of the fibre directional coupler is 8 cm longer than the other).

The same image suggests that the minimum feature size that can be determined using the rings pattern as a sampling function is less than 80 μm, based on the separation of adjacent fringes situated at the pattern extremities.

For a voltage of 0.4 V applied to the X-scanner and in the absence of scanning along Y, the photodetected signal's main component observed on a spectrum analyser peaks at 5 kHz. This is in accordance with the value of 5.4 kHz obtained from (4-12) where z_1 = 14.5 cm, z_2 = 10.2 cm and α = 1.6°. Adjustment of the bandpass filter is therefore carried out to make it operate at this frequency with a Q-factor of 10.

A convenient way to evaluate the technique on a real target is to look at the standard, easily identifiable surface features of a 1 penny coin mounted on the micrometer translation stage.

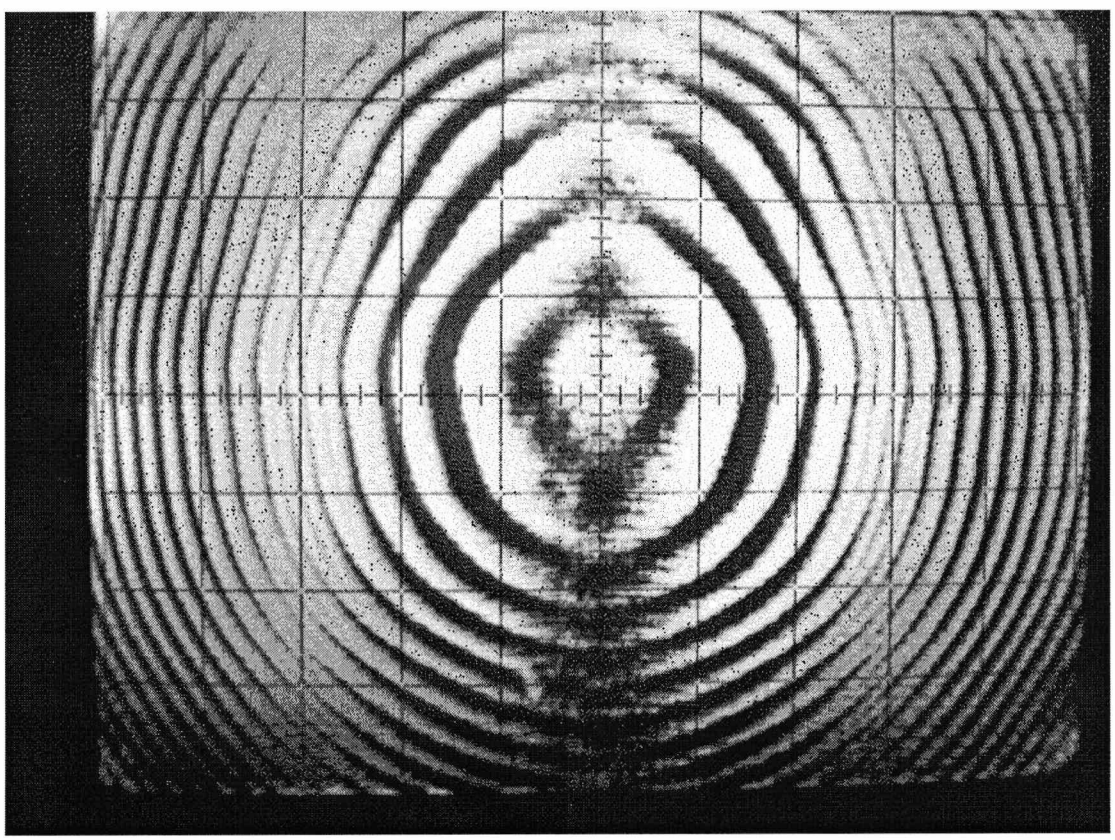

Figure 4.6 Newton's rings from a plane mirror

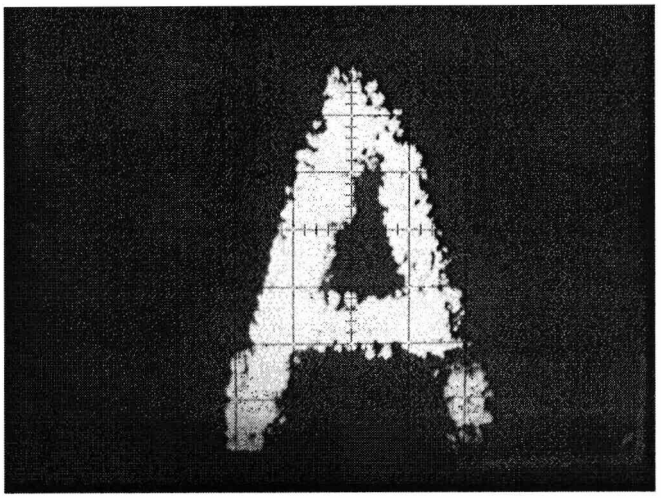

Figure 4.7 Photograph of the oscilloscope screen showing an image of letter A embossed on a 1 penny coin. The bright zones correspond to the region of coherence.

The image in Figure 4.7 was obtained as the upper face of the embossed letter A on the coin was intersected by the coherence surface. As the length of the reference arm is increased by 60 μm, the coin "background", or recessed area, enters the coherence surface, as shown in Figure 4.8.

The technique has the disadvantage that no modulation arises when the target surface coincides with the coherence surface Σ. In this case, a very smooth surface with curved profile matching exactly the shape of Σ will register as just one continuous fringe and will not allow the formation of an image. However, this is a relatively unlikely case for an arbitrarily shaped non-specular object.

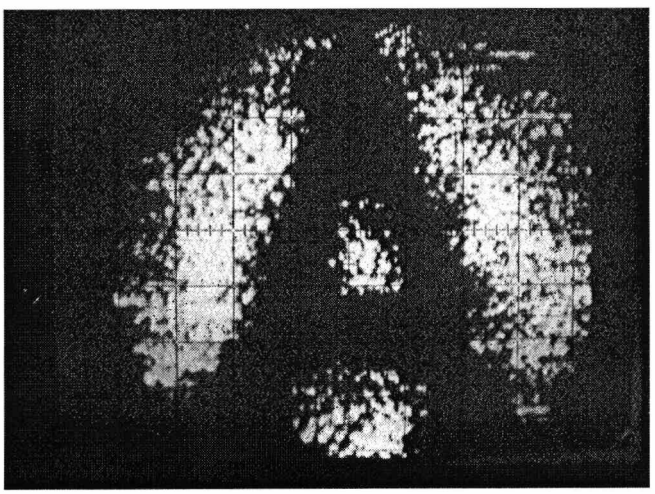

Figure 4.8 A "negative" of the image in Figure 4.7, this photograph of the oscilloscope output shows a bright coin background, when the reference arm path was increased by 60 μm compared with the situation in Figure 4.7.

Finally, the frequency spread of the Doppler-like signal depends on target particularities. In some cases the frequency spread may require a larger bandwidth with consequences in terms of the S/N ratio.

4.4 Elimination of lower frequencies. Displaced beam case

The *en face* imaging procedure demonstrated in the previous paragraphs does not rely on conventional path modulation methods, is relatively simple to implement, offers a quick display capability and is ideally suited for surface or volume imaging.

Equation (4-8) shows that, for a flat target, when the object beam is incident on the axis of rotation of the X mirror the OPD between the object and reference arms is proportional with the square of the deflection angle of the scanning mirror. Consequently, when the target arm is coherence matched with the reference arm, the object is sampled by a sampling function in the form of Newton rings. In this non-displaced beam case, the frequency spectrum of the photodetected signal contains components from 0 Hz in the centre up to a maximum frequency f at the extremities, when the beam samples the maximum concentration of Newton rings.

For signal processing and imaging purposes it is desirable to make the fringe separation more constant across the sampling function. This would mean generating a Newton's rings sampling function with the centre somewhere outside the image area, whose higher order rings can be approximated with parallel equidistant fringes. To this end, the effect of laterally displacing the target beam by a certain distance away from the axis of rotation of the Y-mirror is examined in the following paragraphs.

4.4.1 Linearisation of the OPD with deflection angle. Displaced beam

For imaging applications, such as retinal scanning, which demand that all the rays in the fan to pass through the centre of the eye pupil, the scanning angles required to produce a scan size of a few millimetres across are quite small, and in this approximation it is found that the path imbalance OPD introduced between the central ray (along the optic axis) and the ray deflected by an angle β from the optic axis can be written as:

$$OPD = -2\delta\beta + f_2 \frac{z_1^2}{z_2^2}\beta^2 \qquad (4\text{-}18)$$

Distances z_1 between the axis of rotation of MY and L1 and z_2 between L1 and L2 (see Figure 4.9) are measured along the optic axis of the eye collimation arrangement and L_1 and L_2 are the focal lengths of lenses L1 and L2 respectively.

A shift of the axis of rotation of the MY galvanometer scanning mirror is introduced by displacing SXY towards C2 by a distance δ and the support holding the fibre and collimator C2 laterally by δ. In this way, for $\beta = 0$, the incoming ray intersects mirror MX at a location on the optical axis situated at $z_1 - \delta$ away from lens L1.

The displacement of the beam by a distance δ results in an optical path change of $\delta\beta$, which leads to the first term in (4-18) accounting for the double pass of light (to and from the object). The second term gives the path imbalance responsible for Newton rings imaging whose formula was deduced in paragraph 4.3.4. The frequency due to scanning a mirror perpendicular to the optical axis, located in the focal plane of lens L2, is given by:

$$f = \frac{8\gamma F_x U}{\lambda}[\delta - 4kUL_2\frac{z_1^2}{z_2^2}t] \qquad (4\text{-}19)$$

where γ is the scanner responsivity, U the scan amplitude, F_x the frequency of the triangular wave modulation signal applied to the galvanometer mirror and λ the central source wavelength. During a scan, the frequency f varies between:

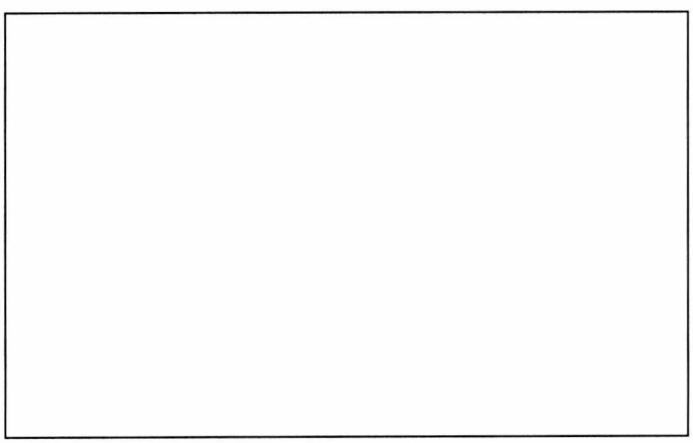

Figure 4.9 Geometry of the reflected ray for a lateral beam displacement δ and ray deflection angle β; MX = galvanometer scanning mirror, L1 = lens

$$f_{min,max} = f_c \pm f_n = \frac{8\gamma F_x U}{\lambda}[\delta \pm L_2 \frac{z_1^2}{z_2^2}\beta_m] \qquad (4\text{-}20)$$

where f_c is the central frequency and f_n the frequency spread owing to the non-linear OPD dependence on β in (4-18) (this is also the maximum component in the spectrum when the beam is centred, which is the Newton rings sampling function case). The interference signals are produced when $|P| < l_c$, where l_c is the coherence length of the source, and the maximum angle $|\beta|$ for which $|OPD| = l_c$ is β_c. For $|\beta| > \beta_c$, $\beta_m = \beta_c$ and for $|\beta| < \beta_c$, $\beta_m = kU$.

The enlargement $\Delta\nu_o$ due to the optical linewidth is much smaller than that due to the second term in (4-20) and can be neglected for the purpose of this first approximation treatment. However, for most applications, the information bandwidth B_i is larger than f_n. Working from the size of a pixel on the target situated a distance L_2 behind lens L2, from the focused beam diameter D and from the number of pixels within the transversal scan excursion ΔY across the target, the image bandwidth results as:

$$B_i = 0.82\frac{F_x D}{\lambda}\frac{\Delta Y}{L_2} \qquad (4\text{-}21)$$

The linear term in (4-19) becomes dominant when the shift δ is large enough, providing a first condition for the minimum value of δ. A second condition results from restricting the minimum value of the sampling function bandwidth to the value of the information bandwidth:

$$f_c - f_n > B_i \qquad (4\text{-}22)$$

The second condition (4-22) prevails and it can be rewritten as:

$$\delta > \frac{z_1}{z_2}\sqrt{L_2 l_c + 0.04D^2} \qquad (4\text{-}23)$$

During scanning, as the carrier frequency f is variable, the bandwidth of the band pass filter needs to be large enough to accept signals at the minimum frequency f_{min}-B_i and at the maximum frequency f_{max}+B_i, i.e. a bandwidth $2(B_i+f_n)$ (this is only an

approximate evaluation). In terms of noise, therefore, the method presented here is inferior to the conventional technique for larger scan angles.

4.4.2 Experimental arrangement

The experimental arrangement is similar to the one described in paragraph 4.3.9. Light from a pigtailed superluminescent diode, SLD, is injected into a single mode directional coupler, DC2. The transmitted light from one of the output ports is fed into a second coupler, DC1, whilst light from the other port is inserted into a liquid matching gel cell, LMG. The arms of DC1 form a Michelson interferometer. The reference arm consists of microscope objective C1, mirror M1 and computer controlled translation stage TS. The other arm (sensing), consists of microscope objective C2, scanner SXY, lens L1 and object under test (OUT). The fibre lengths were cut to a 1 mm difference to keep differential dispersion low and the fibre ends were polished at 10° to reduce the amount of returned light.

The signal detected by PD2 is amplified by a factor of 2 more than the signal from PD1. Balanced detection is introduced, with the signals being applied to a differential amplifier DA to enhance the interference signal and cancel out the intensity modulation caused by the variation in target reflectivity.

The resulting output is amplified, band-pass filtered in BPF and then applied to a high voltage amplifier used to drive the "z modulation" input of an analogue storage oscilloscope, ASO. Alternatively, a digitised image can be obtained with the aid of a variable scan frame grabber, VSG, which can save its output as a graphic file.

Two triangle (or ramp) waveform generators, TX and TY, are used to drive the two mirrors, MX and MY, of the scanner block, SXY.

The quantities which determine the value of B_i = 5.27 kHz from equation (4-21) are set as follows:

F_x = 20 Hz

λ = 0.83 μm

D = 2 mm

L_2 = 3 cm

ΔY = 2 mm.

To produce a scan of width ΔX = 2 mm for z_1 = 14.5 cm and z_2 = 10.2 cm, the X mirror drive voltage is set to U = 0.34 V.

From equation (4-23), where $l_c = 31.89$ μm, the lower limit for the value of the mirror shift δ results as 2.1 mm.

Mirror MX was translated by a distance $\delta = 3$ mm, resulting in $f_c = 13.73$ kHz and $f_n = 6.4$ kHz. In comparison, for an optical bandwidth $\Delta\lambda = 20$ nm of the superluminescent diode, the calculated value of the peak enlargement is $\Delta f_0 = f(\Delta\lambda)/\lambda = 0.33$ kHz.

4.4.3 Experimental results

With mirror MY driven by a triangular signal of amplitude U = 0.17 V and frequency $F_y = 20$ Hz, an optically flat target (a mirror was used in this case) produces fringes whose corresponding spectra (left) and time evolution (right) are shown in Figure 4.10. In order to restrict the detected signal to only a cross section of the fringe pattern, mirror MY is kept stationary.

The graphs in the upper row correspond to the centred beam case and the ones in the lower row to the case when the beam displaced by $\delta = 3$ mm. The displaced beam case produces, as it can be seen from the frequency spectrum, a very distinguishable carrier peak.

A good correlation exists between the theoretically predicted frequency values given by equation (4-13) ($f_c = 6.86$ kHz and $f_n = 1.6$ kHz) and the values suggested by the graph in Figure 4.10 bottom left [60].

The time evolution for the centred beam case is practically a cross section of the Newton rings fringe pattern shown in Figure 4.6 along the rings' diameter. The very low values for the frequency f, present in the spectrum of this pattern, are due to the ever increasing fringe spacing towards the centre of the rings.

An X-Y screen image is subsequently generated by applying a triangular wave modulation of frequency $F_y = 0.2$ Hz and amplitude U = 0.17 V both to mirror Y and to the Y input of the oscilloscope display. Synchronisation of the X and Y modulating waveforms with the oscilloscope screen spot deflection leads to the formation on the screen of an X-Y raster image proportional in size with the waveform amplitude in each direction.

A magnifying zooming effect can be achieved in either or both directions by controlling the X or Y settings of the oscilloscope display. This allows the restriction of the display to a selected area which fills the entire screen.

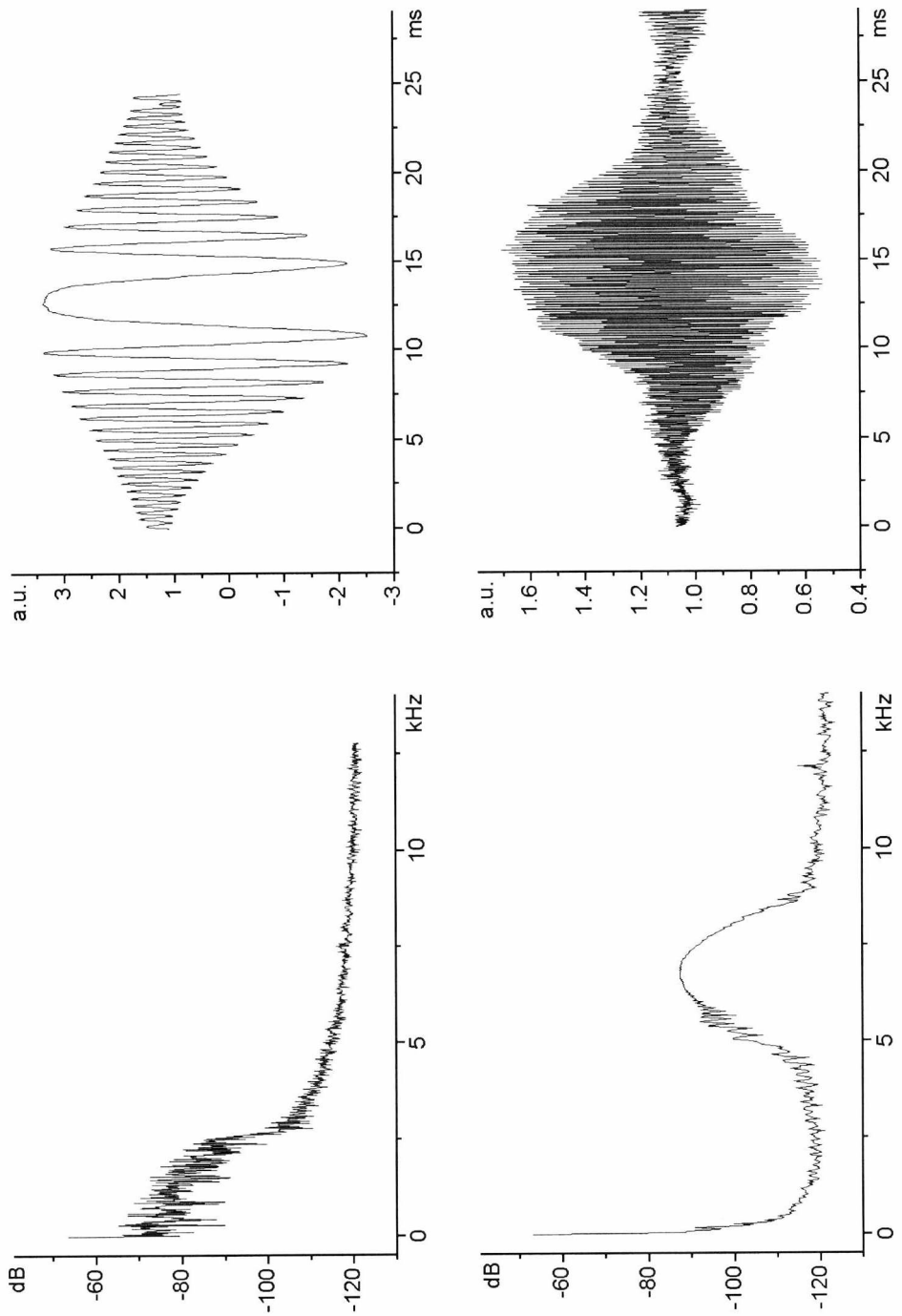

Figure 4.10 Frequency spectra (left) and the temporal evolution (right) for spot centred (top) and spot shifted by δ = 3 mm (bottom). z_1 = 14.5 cm, z_2 = 10.2 cm, triangular signal applied to the Y-scanner of amplitude U = 0.17 V and frequency F=20 Hz, Y mirror not driven.

The aspect of the field of view corresponding to an area slightly larger than the entire illuminated target area is shown in Figure 4.11. It can be seen that the fine structure of the rings is not apparent with this choice of display settings and the illuminated area is rendered as an indiscriminate luminous patch.

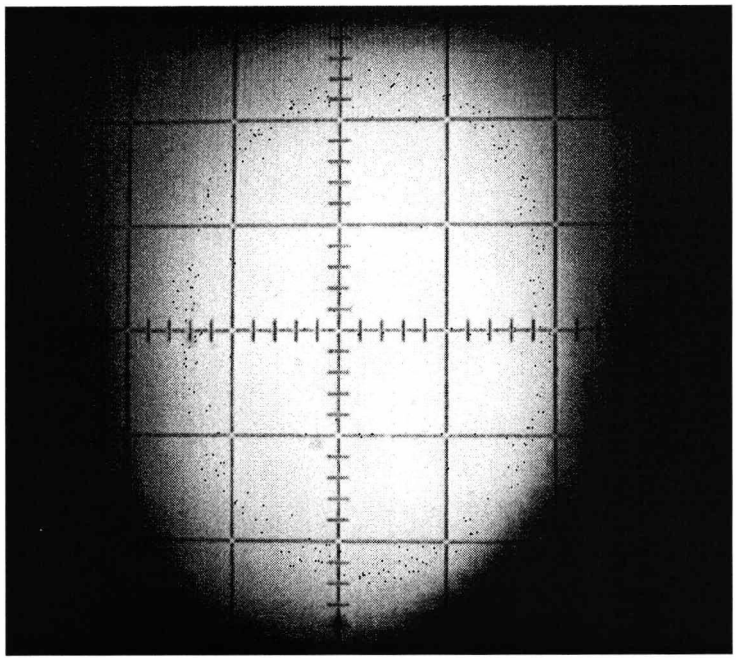

Figure 4.11 Photograph of the oscilloscope output showing the appearance of the rings from a mirror target. Both scanners are driven by triangular signals of amplitude U = 0.17 V, F_x = 20 Hz, F_y = 0.2 Hz, δ = 3 mm, horizontal and vertical scale 50 mV/div

The fine sampling function characteristics become apparent when only part of the area is made to fill the screen by effectively zooming in on the sampling function details (Figure 4.12).

Geometrical optics considerations and the value of the waveform amplitude result in a conversion factor of 29 μm/mV between the target size and the oscilloscope display, which in turn gives a value of 6 μm for the spatial period of the fringes. The minimum feature, which can be sampled and displayed using this sampling function, is therefore the double of the fringe spacing, i.e. 12 μm.

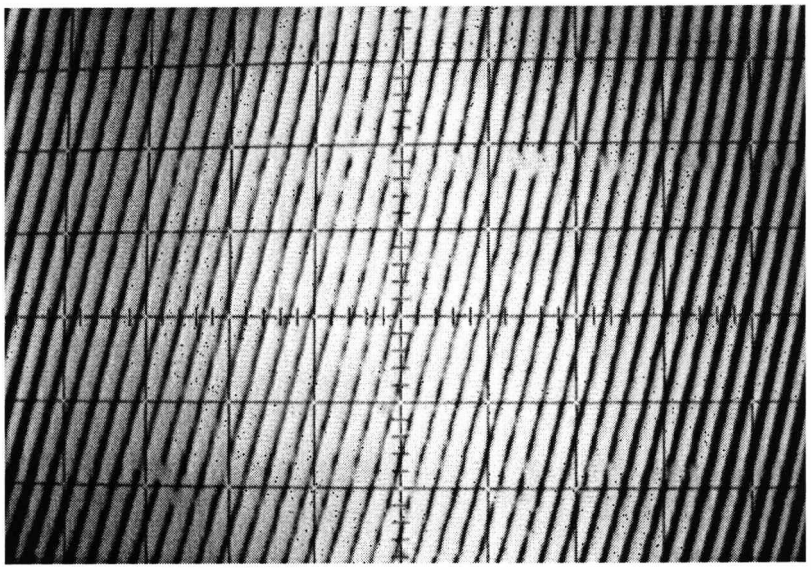

Figure 4.12 Photograph of the oscilloscope output showing the appearance of the rings from a mirror target. Both scanners are driven by triangular signals of amplitude U = 0.17 V, F_x = 20 Hz, F_y = 0.2 Hz, δ = 3 mm, 10 mV/div horizontal and vertical oscilloscope display scale.

A resolution of 12 μm is considerably better than the minimum detectable separation deduced in paragraph 4.3.10, and in addition is quite constant across the area displayed.

In the case examined here it is the scan of mirror MX that leads to the generation of a fringe pattern whereas the slower scan of mirror MY is merely incrementing the lateral position of the beam on the target. The resulting fringe pattern resembles a set of parallel lines whose inclination changes in proportion to the angle φ, measured in the y-z plane, made by the target surface with the x-y plane (see Figure 4.13). If the

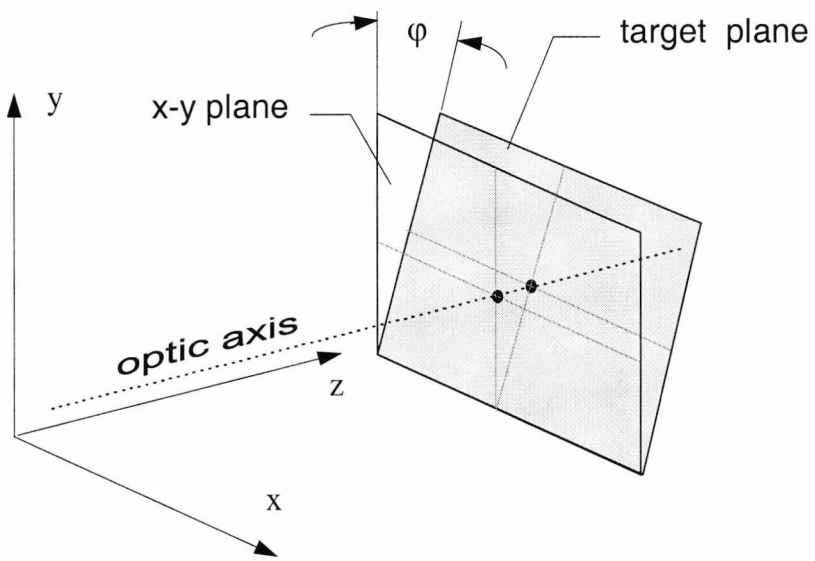

Figure 4.13 Inclination of the target plane with respect to the x-y plane

functions of MX and MY were to be reversed such as the MY scan is the fringe generating scan, the angle φ would need to be measured in the x-z plane.

If the target plane coincides with the x-y plane, the inclination of the fringe pattern is not necessarily zero, due to the asymmetric character of the displaced beam geometry. The fringe pattern angle can be used as an estimate of the differential target angle in applications requiring a measurement of the target angle.

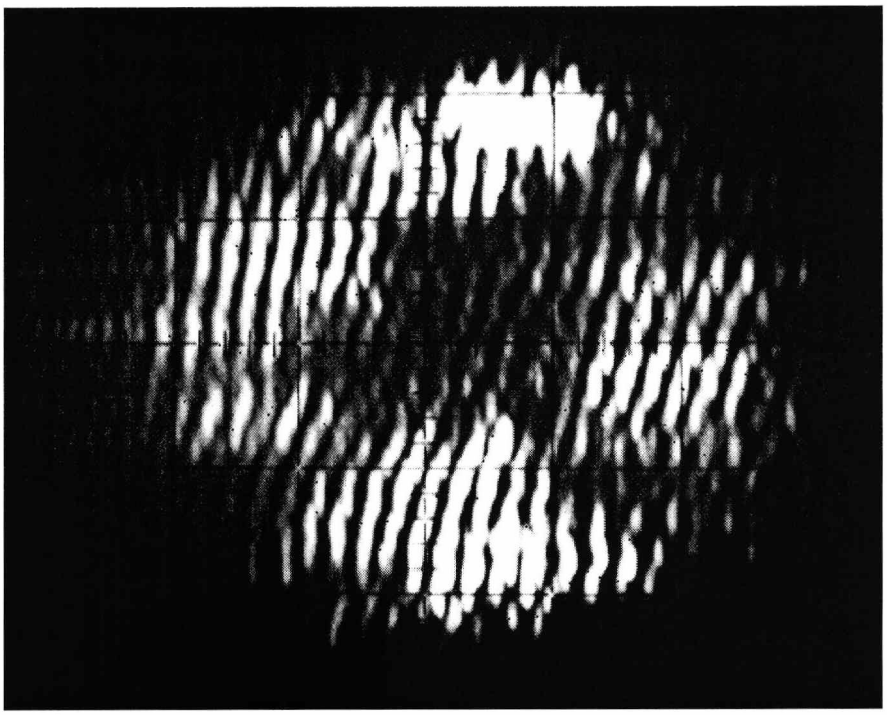

Figure 4.14 Image of the cleaved end face of a single mode fibre, rendered by the Newton rings sampling function

In order to assess the capability of displaying very small target features with this method, images were collected from the end face of a single mode fibre, cleaved to provide a flat surface. Figure 4.14 shows one such image, obtained with the same drive and display parameters as those producing the pattern in Figure 4.12.

The outline of the fibre end's 125 μm diameter disk is clearly distinguishable, with the modulating effect of the sampling function superimposed on it. Irregularities in the target depth profile are suggested by the presence of interruptions in the fringe pattern, notably in the centre of the disk.

4.4.4 1/f noise

One of the potential disadvantages of the Newton rings sampling function method is that in order to process the coherence image, a bandwidth down to 0 Hz is required. This allows through noise whose level is inversely proportional to the frequency of the signal (1/f noise). Effective suppression of 1/f noise can be achieved with a high pass filter and it is desirable, therefore, to generate a high carrier frequency in the spectrum of the detected signal.

The galvanometer scanning system can be operated at rates which lead to the generation of a modulation frequency in the region of a few hundred kHz. As shown by equation (4-20), the temporal fringe frequency increases with the off-axis beam displacement δ. An upper limit for δ (in this case 3 mm) is set by the size of the scanning mirror since increasing δ further would result in part of the beam falling outside the mirror aperture.

At maximum displacement, with a 2 V, 300 Hz driving ramp, a value in excess of 200 kHz was obtained for f_c, which compares favourably with the frequencies obtained with continuous Doppler longitudinal scanning (described in previous chapter) and with modulation frequencies of piezo-elements described in literature [4], [61], [62].

In the case of non-displaced beam scanning resulting in a circular Newton rings pattern, the process of filtering out low frequencies has the effect of "erasing" the centre of the pattern. Uneven sampling between the centre and the periphery is avoided by the beam displacement procedure which ensures that object features right across the illuminated area are sampled at the same rate and therefore appear equally sharp in the high pass filtered image.

4.4.5 Shape of the coherence surface

Compared to the case of the non-displaced beam, the coherence surface changes in the displaced beam case from spherical to conical. For small angles β, the conical surface can be approximated with a plane forming an angle $90° - \varphi$ with the y-z plane and intersecting it in O (Figure 4.13).

The relationship linking the tilt angle φ, the beam displacement δ and the focal length L_2 is:

$$\tan \varphi \approx \frac{\delta}{L_2} \qquad (4\text{-}24)$$

An increase in the beam displacement δ results therefore in a larger tilt angle φ. A tilt of the coherence surface can be compensated by a suitable tilt of the object if possible. However, the images in Figure 4.11, Figure 4.12 and Figure 4.14 were generated without deliberately introducing an object tilt, which shows that for a small angle β the distortion of the coherence surface can be tolerated.

4.4.6 *En face* retinal images

A 3×3 mm^2 area of the retina of a volunteer is shown in Figure 4.15. This slice contains identifiable details and offers a good idea about the imaging capability of the *en face* technique. The image was produced with a variable scan frame grabber (DataRaptor). The X and Y galvanometer scanners were driven by ramps of amplitude 1V and frequencies $F_x = 300$ Hz and $F_y = 0.5$ Hz.

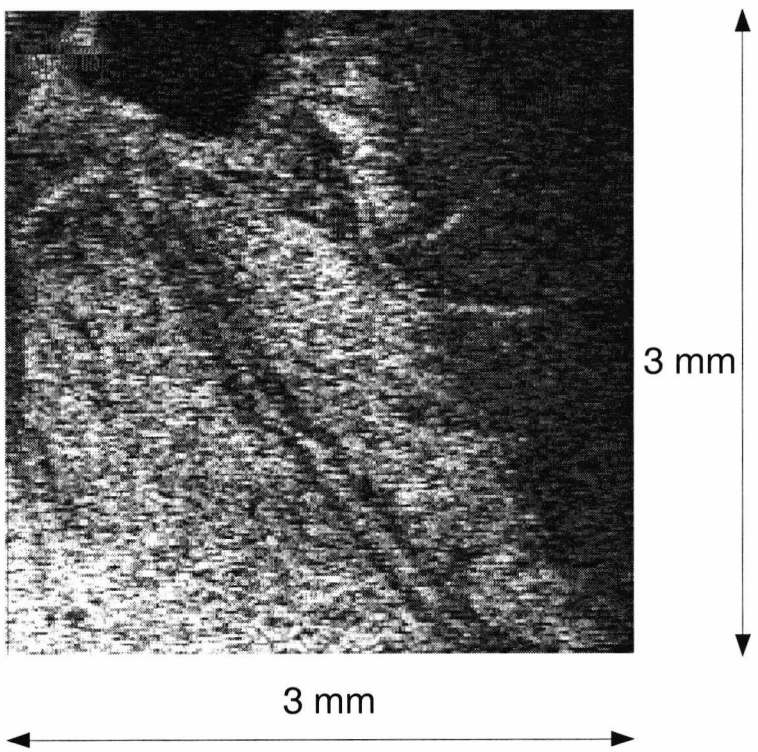

Figure 4.15 In vivo retinal image obtained with the Newton rings technique

The image shows several blood vessels (of which the one running diagonally exhibits two clearly visible boundaries), and the dark area appearing at the top edge, which is the optic nerve head. Since this image is merely a section, a "slice" in volume, details of the entire optic nerve head structure would not be visible as they lie at different depths, i.e. outside the range of just one slice. A number of such images

are required to build a 3-D profile of a reasonably large retinal structure such as the optic nerve head.

This task has been undertaken using both the centered and the non-centered arrangements in order to compare their performance for retinal imaging. Transversal (*en face*) (x,y) as well as longitudinal OCT (x,z) slices were produced using the phase modulation generated by the galvanometer scanner alone or using the modulation introduced by the galvo-scanner in addition to that of a piezo-cylinder in the reference arm. The revised optical set-up is shown in Figure 4.16 below:

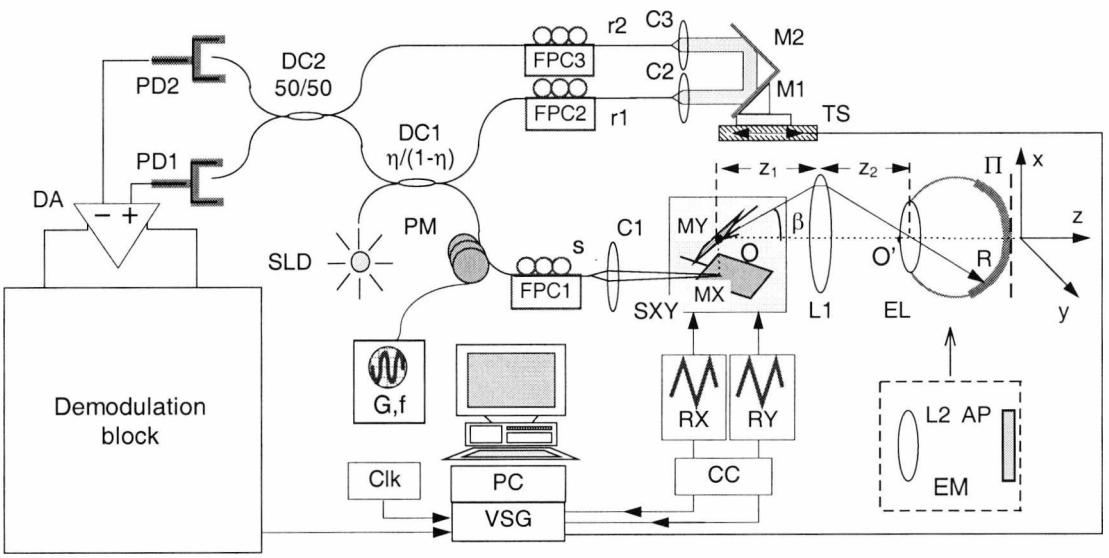

Figure 4.16 Advanced *en face* OCT imaging set-up. SLD: Superluminescent diode (Superlum SLD-361); C1, C2, C3: microscope objectives; DC1, DC2: directional couplers; PM: 5 cm diameter piezo-cylinder with 2 turns of fibre acting as a phase modulator; G: sinusoidal generator, f = 30 kHz; M1, M2: mirrors; L1: convergent lens; FPC1,2,3: polarization controllers; SXY: orthogonal scanning mirror pair; MX(MY): mirror of the X(Y) scanner; DM: demodulation block; RX, RY: ramp generators; PD1, PD2: photodetectors; DH: CC: controlling circuitry; Clk: VSG clock generator; EL: eye lens; R: human retina; EM: eye model; L2: convergent lens; AP: aluminium plate; TS: computer controlled translation stage; PC: personal computer.

For reasons of simplicity the target eye model (EM) is assumed to consist of a smooth plane, AP, perpendicular to the optical axis. When *in vivo* measurements are carried out, a volunteer's eye is brought into the target area such that the eye lens EL replaces lens L2 and the subject's retina R replaces the planar target AP. To assist volunteers with the positioning of their heads, a chin rest was attached to the instrument.

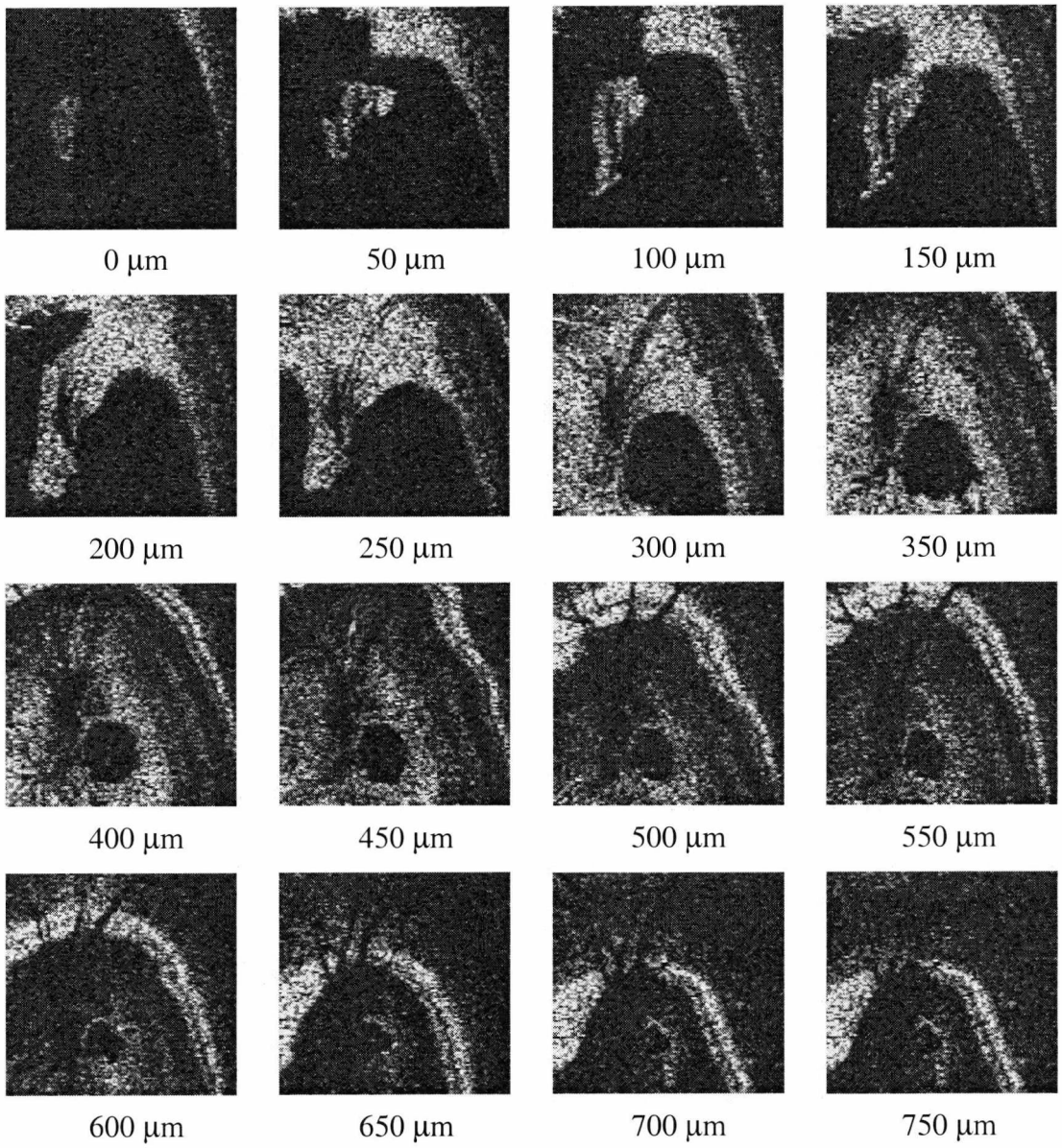

Figure 4.17 *En face* OCT slices of an *in vivo* retina. Depth intervals between successive images are 50 microns

A set of OCT transversal images of the optic nerve area, obtained at different depths by successively incrementing the reference arm length 50 μm at a time, is shown in Figure 4.17. Each frame is 3mm by 3 mm and is obtained in 1 s. The top of the retinal nerve layer is seen in the 0 μm image. The central parts of the 450 μm - 600 μm images correspond to the photodetector fibre layer while the high intensity areas in the 600-700 μm images show the retinal pigment layer.

Figure 4.18 shows four other 3 mm by 3 mm images from the foveal region of a different volunteer's eye, where structures such as the Retinal Nerve Fibre Layer (RNFL) and the foveal pit can be identified. The images are also acquired in 1 s.

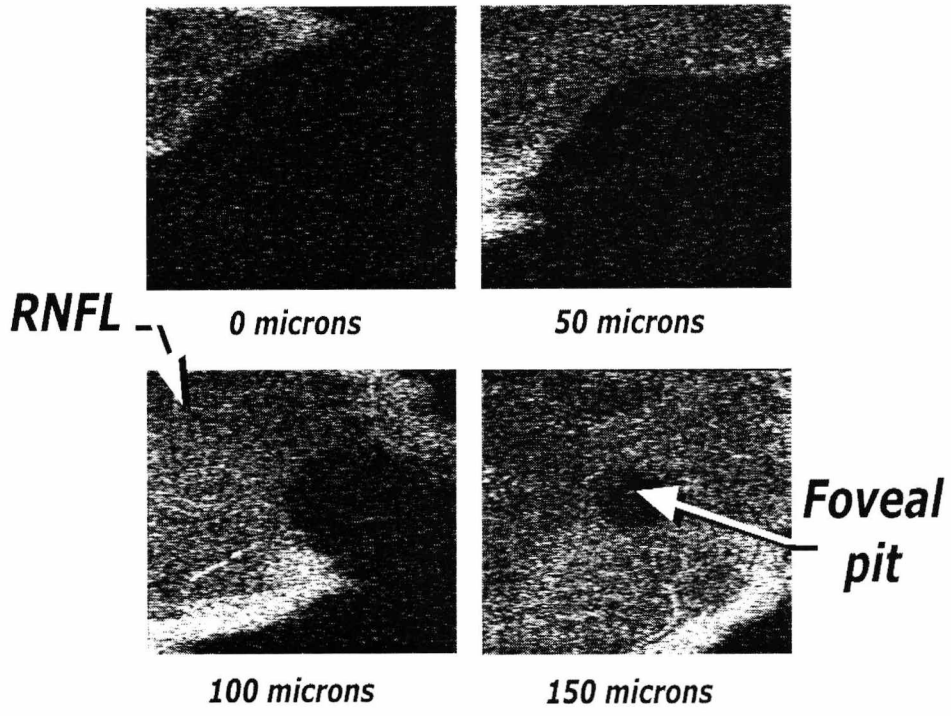

Figure 4.18 OCT images of the foveal region at different depths

All eye images presented so far have been of the *en face* type, generated by executing an x-y scan (with the z direction being the optic axis of the eye). The instrument, however, is flexible enough to allow longitudinal (x-z or y-z type) images to be produced without any hardware modifications. For instance, by driving only the X galvo-scanner and translating the reference mirror at a speed of 1 mm/s the longitudinal OCT

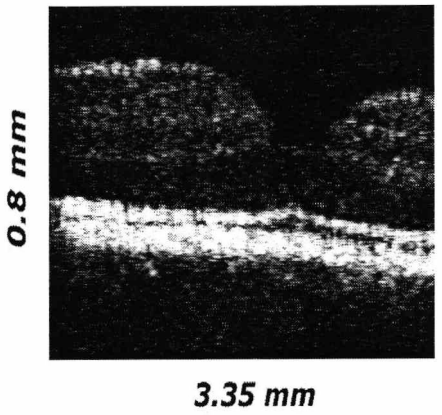

Figure 4.19 In vivo cross-section image obtained by en face OCT of the human retina showing the foveal pit. Angular extent of 6.8° corresponds to a span Δx = 3.35 mm on the retina.

image in Figure 4.19 was generated.

All images were obtained with a power of 90 μW incident on the eye; no averaging was applied.

The difference in quality was found to be minimal between the images shown in Figure 4.17 to Figure 4.19 on one hand and those produced with the conventional technique presented in chapter 5 (phase modulation in reference arm followed by detection and demodulation at the same frequency).

Little difference was also observed between the images obtained from the living retina in the centered beam case and the ones obtained in the off-centred beam case (within, of course, the limitations imposed by the performance of our devices: X-scanning rate up to 1000 Hz, maximum angular image size of 10°, frame rates from 1 to 5 Hz and processing bandwidth of about 150 kHz).

4.4.7 Concluding remarks

Images of similar quality are obtained with those using the conventional technique, where the optical beam is centered on the galvo-scanning mirror, i.e. $\delta = 0$, and a separate device is used in the reference path for modulation.

The modulation spectrum is different in each of the two cases. In the centered case, the spectrum is almost flat up to a maximum frequency value. In the off-centered case, the spectrum is centered about a carrier with side bands. The larger the horizontal image size, the higher the values of the carrier, sidebands and the image bandwidth. In the off-centered case, in order to avoid superpositions of spectra, a minimum carrier frequency must be achieved to accommodate the signal bandwidth. Obviously in this case the sampling function is better for imaging reasons because of a higher achievable transversal resolution. In the off-centered case, for a sufficiently large offset δ, the sampling is homogeneous across the entire target.

In the centered case details in the center of the image are sampled at a lower spatial rate. Consequently, the image pixel size depends on the path modulation method used and for the centered case is variable across the target.

The disadvantages of the Newton rings method applied to imaging are several but neither poses significant problems that could not be overcome:

(i) no modulation arises when the object and the coherence surfaces coincide and the target becomes "invisible" - this is actually an extremely rare occurrence;

(ii) the pixel size varies across the target area but this can be compensated for with relatively simple digital signal processing;

(iii) the modulation frequency and consequently the central frequency of the demodulation block are dependent on the image size; this requires a tunable filter and operator assistance;

(iv) the sampling function modulating the image intensity can be visible when fine details of size comparable with its periodicity are investigated [60]. Moreover, the sampling function is visible when imaging surfaces that exhibit specular reflection, as shown in paragraph 4.3.10. However, most surfaces will not be specular so the sampling function will not appear in the image.

5. Simultaneous OCR "slicing" at two or more depths

5.1 Introduction

Low coherence reflectometry is a potentially powerful method for performing optical biopsy and non-invasive optical diagnostics *in vivo*. However, the usually low signal to noise ratio of light returned from *in vivo* tissue and the intrinsically limited speed of mechanical scanners require a longer time to produce good quality images than would be acceptable for such applications. Rapid acquisition is essential for imaging living tissue in motion, such as eye or heart tissue.

One reported LCR instrument capable of performing 4 frames a second acquisition [63] uses a cylindrical piezo-element with a long fibre stretch wrapped around it. A Doppler shift in the MHz range is generated in this fashion, avoiding the need for a mechanical translation stage for depth scanning.

One way of speeding up volume data acquisition allowed by *en face* OCT is the capture of data from more than one depth at a time. If this can be achieved, then the goal of real-time imaging using parallel channels "coherence tuned" to different depths will have moved closer.

This chapter therefore looks at the possibility of simultaneously producing transversal images from several layers in the human eye. The principle is demonstrated by generating two sets of en-face images from an *in vitro* retina for depth positions situated 250 μm apart.

5.2 Optical arrangement

The optical arrangement set-up is shown in Figure 5.1. It is similar to those presented in earlier chapters, and it has at its core the fibre Michelson interferometer. Light from a pigtailed superluminescent diode, SLD (Superlum SLD-361 series), is injected into a single mode directional coupler, DC2. The transmitted light from one of the output ports is injected into a second single mode

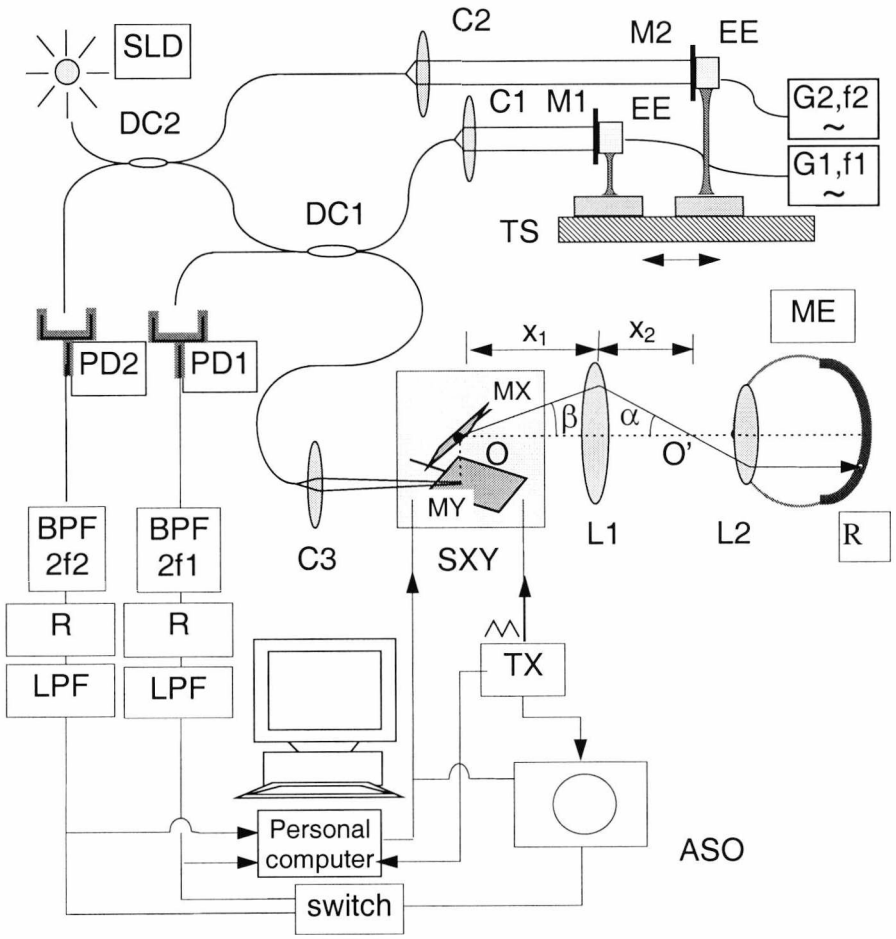

Figure 5.1 Instrument for multi-layer OCT [60]: PD1, PD2: photodetectors; BPF: bandpass filter; R: rectifier; LPF: low pass filters; TS: computer controlled translation stage; ASO: analogue storage oscilloscope; EE: electrostrictive element; G1, G2; sinusoidal generators.

coupler, DC1, whilst the light from the other port is directed to mirror M2. All three fibre ends were polished at a 10° angle to reduce the noise associated with backreflected light. The preparation of the post-mortem eye and its mounting in a suitable transparent container to allow light in are described in Appendix A.

5.2.1 System adjustments

Two Michelson interferometers are formed using this arrangement. The reference arm in each interferometer consists of a microscope objective, C1 (C2) and a mirror, M1 (M2). Both mirrors are mounted on the same computer controlled translation stage, TS. The OPD between the two interferometers (250 μm) is adjusted by shifting the supports of the fibre ends and collimators C1(C2) relative to mirrors M1 and M2. An analogue storage oscilloscope, ASO is used to assist in the adjustment of each interferometer.

In the sensing arm, light emerging from the fibre is collimated by a microscope objective C3. The beam enters a galvanometer scanning mirror arrangement (SXY), and passes through a converging lens of 60 mm focal length (L1) before entering a model eye (ME) consisting of a 1 cm diameter convergent lens of focal length 30 mm, L2, and a container with human retina in formalin.

The retinal tissue is placed 30 mm behind L2, in an attempt to reproduce the scale of the human eye. The beam spot on the last mirror in SXY and the anterior focus of L2 are conjugate points by virtue of L1.

5.2.2 Signal detection and preliminary processing

Two photodetectors, PD1 and PD2, collect the returned optical signals. After photodetection, the signals are band pass filtered (BPF), at $2f_1$ ($2f_2$). The signals are then rectified (R) and low pass filtered (LPF).

Processing the signal at double the frequency (2f) is preferable in order to avoid the residual intensity modulation at f. Mirrors M1 and M2 are vibrated by two electrostrictive elements, EE, driven by sinusoidal generators G1 and G2, at f_1 = 30 kHz and f_2 = 22.5 kHz respectively. The amplitude of the driving signals was adjusted to maximise the modulation at $2f_1$ and $2f_2$.

The triangle generator TX drives the horizontal line scanner, MX, and triggers the acquisition of the two analogue signals via an A/D interface.

5.2.3 LabView Virtual Instruments

Data acquisition and hardware commands are synchronised under the control of a LabView™ Virtual Instrument (VI). This is a computer program developed under National Instruments' proprietary graphical programming input interface LabView™, which allows a number of controls to be put in place for a variety of external instruments. It was found to be a convenient and inexpensive way of bringing together and synchronising control and acquisition tasks that have to be performed in a certain sequence and where timing is critical.

The full diagrams of the control VI's developed exclusively for this particular multi-layer OCT system are given in Appendix B. The Virtual Instrument produces incremental voltage steps via a D/A interface to drive the vertical scanner, MY, as well as a linear ramp to drive MX. It subsequently receives the data from the A/D acquisition card and displays it in the form of one or more graphic windows.

5.2.4 Scanning pattern

Since the Y scanner steps have to be interlaced with the X generated raster lines, a percentage σ of each T/2 interval is sacrificed to overlap with each step increment (the data collected during this time being of no use). Consequently, a line in the actual raster lasts for only $(1-\sigma)T/2$.

In the galvo-scanning pair MX was driven at 20 Hz, peak to peak amplitude 1 V, $\sigma = 0.1$ and MY was driven through 100 intermediate steps from -0.5 V to 0.5 V. For both mirrors, an applied signal of 1 V produces a 4° deflection. A scan of area 4 mm × 4 mm is thus generated on the target.

5.3 Retinal Images

The series of images shown in Figure 5.2 was obtained. They show the region of the optic nerve head of a post-mortem human retina. It can be noticed that the lower image at a longitudinal co-ordinate value $z = z'$ becomes similar to the upper one at $z = z' + 240$ μm, i.e. the optical path differences in the two interferometers are 240 μm apart. Both images in each frame were simultaneously acquired and displayed in less than 3 seconds.

The production of a twin image instead of a single one does not carry the penalty of a speed reduction or that of a drop in the signal to noise ratio in the first interferometer. The addition of a second coupler (and interferometer) is compensated for by a corresponding increase in optical power, so except for the larger Rayleigh

Figure 5.2 Ten image pairs showing a sample of the optic nerve region of a post-mortem human retina explored with the en-face interferometric multi-layer imaging technique (multi-layer OCT). For each longitudinal co-ordinate (given in microns below each frame) two images 240 μm apart in depth are simultaneously acquired and displayed.

scattering due to longer fibre lengths there is no negative impact of the addition of a second interferometer.

The technique is shown to give good results but there is a small decrease in the quality of the image obtained with the second interferometer, which may not be as good as the one in the first interferometer. This is discussed in more detail in the following paragraph.

5.3.1 Increasing the number of layers

For a higher number of layers (n) an expression can be obtained for the amount of optical power detected at the n^{th} photodetector. If the superluminescent diode power launched in the fibre is P_0, the photodetectors have a sensitivity η, the directional couplers DC have zero loss, the reflectivity of mirrors Mj is R_j, and the eye returns a fraction O of the incident power (both R_j and O adjusted to include coupling losses in and out of fibre) the power at photodetector PDn, is given by:

$$i_n = \eta P_0 \times \left[\frac{O}{2^{2n}} + \frac{1}{4} \sum_{j=1}^{n} \frac{R_j}{2^{2(n-j)}} + \frac{(-1)^{n-1}}{2^n} \sqrt{OR_n}\,\gamma(d_{On}) \cos\left(\frac{2\pi}{\lambda} d_{On}\right) + \sum_{j=1}^{n-1} c_j(n) \sqrt{OR_j}\,\gamma(d_{Oj}) \cos\left(\frac{2\pi}{\lambda} d_{Oj}\right) + \sum_{j,p=1}^{n} e_{jp}(n) \sqrt{R_p R_j}\,\gamma(d_{pj}) \cos\left(\frac{2\pi}{\lambda} d_{pj}\right) \right] \quad (5\text{-}1)$$

where γ stands for the modulus of the optical field correlation function, d_{Oj} is the OPD in interferometer j, d_{pj} is the OPD between mirrors Mj and Mp, c_j and e_{jp} numerical coefficients and λ is the central wavelength of the SLD spectral profile.

In equation above, the first two terms represent the bias, the third one is the useful signal, periodic with components at multiples of f_n. The fourth term represents interference events between the object and the previous reference mirrors, j=1,...n-1. These are periodic terms at multiples of frequencies f_j with $j \neq n$ which can be sufficiently attenuated by the band pass filter tuned to f_n, if the frequency values f_j are correctly selected.

The last term represents interference events between the signals reflected by the mirrors Mj and Mp with $p \neq j$. These are very small when the OPD increment from mirror to mirror exceeds the coherence length (due to the small value of $\gamma(d_{pj})$ in (5-1)). In the configuration shown in Figure 5.1, the depth separation between interferometers is d_{12} = 250 μm, which is much longer than the 25 μm coherence length of the source.

5.3.2 Optical power and number of layers

As one moves from one interferometer to the next, the object power decreases by the same factor that the reference power increases by. Consequently, a similar amplitude for the useful interference signal results at all photodetectors, given by the third term in (5-1).

An increase in the number of layers should be accompanied by a corresponding increase in the optical source power. For safety reasons, the power of the beam entering the eye should be limited to a value P_s, with $P_s = P_0/2^n$ from the third term in equation (5-1). It is clearly seen that the useful term is maintained constant as n increases if the source power is correspondingly increased. This increase in power is feasible with existing large bandwidth optical sources. The images in Figure 5.2 were

obtained with an SLD of 0.7 mW optical power. In principle, up to P_s= 0.2 mW CW power concentrated on a moving spot could be injected in the eye at 800 nm.

Given that the average power of solid state large bandwidth lasers [62], such as a Kerr lens mode-locked Ti:Al_2O_3 can exceed 400 mW, a very large number of interferometers may, in principle, be operating simultaneously, in parallel.

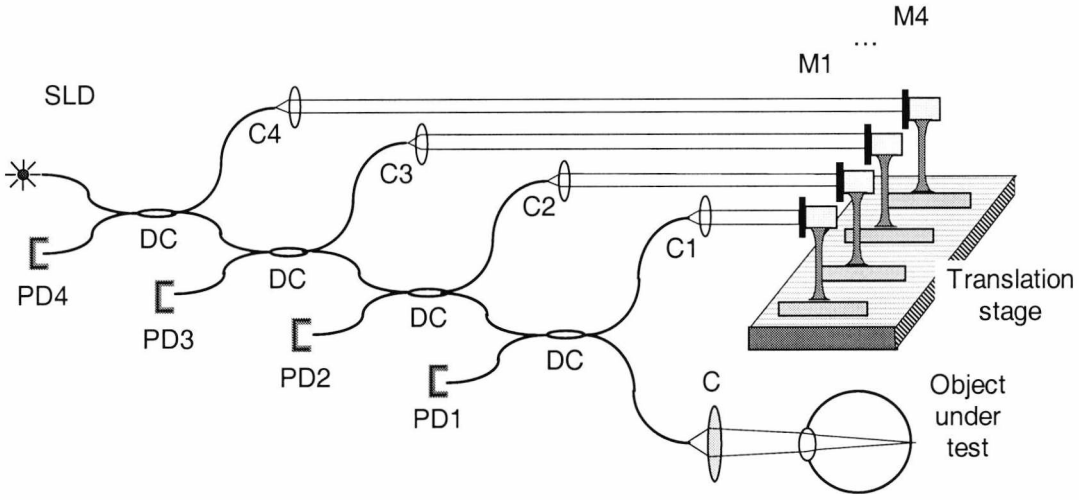

Figure 5.3 System with 4 couplers (interferometers) for the simultaneous display of 4 layers. SLD: low coherence pigtailed optical source (superluminiscent diode); DC:50:50 single mode directional couplers; PD1-4: photodetectors; M1-4: mirrors; TS: computer controllable translation stage; C1-5: microscope objectives.

Consequently, as equation (5-1) shows, one limitation for the number of layers would be the saturation power at the level of the n^{th} photodetector. If a photodetector saturation limit of 1 mW is imposed (for illustration only; higher values can be accommodated in practice), this would restrict the optical source power to 4 mW. In order to get P_s = 0.2 mW injected into the eye, no more than 4 interferometers could be used, as in this case $2^4 \times 0.2 = 3.2$ mW and $2^5 \times 0.2 = 6.4 > 4$ mW. The diagram in Figure 5.3 shows the concept extended to 4 interferometers.

5.3.3 Balance between noise and power

Another important constraint on increasing the number of layers (and accordingly of interferometers) derives from the fact that the interferometers are not physically independent. The interference signal from the first interferometer is present on the photodetector in the second interferometer, the interference signal from the second is present in the third interferometer and so on. The electronics in the n^{th} interferometer should have to filter out n-1 interference signals, as shown by the fourth term in (5-1).

In addition, the higher the number n, the higher the bias in (5-1) and the shot noise, both of which result in an increase of the noise level, although the noise given by the fourth term in (5-1) can be reduced by a correct selection of frequencies f_j.

On one hand, our electrostrictive elements were capable of vibrating millimetre size mirrors as fast as 35 kHz. As far as the galvo-scanner modulation is concerned, it was shown in Chapter 4 that a 20 Hz signal applied to the horizontal scanner results in a bandwidth enlargement of up to 0.5 kHz.

But with a quality factor setting of Q = 20 selected for the bandpass filter, a minimum carrier frequency of at least 20 kHz is desirable. In the 20-35 kHz range, at least 4 carriers could be selected at for instance 20, 23, 26 and 32.5 kHz, in such a way that no multiples of any one carrier fit inside the bandwidth of any other carrier and the nearest component is at least 4 kHz away from the tuned frequency. Higher modulation frequencies could be achieved by using electro-optic crystals, in which case another unmodulated crystal should be placed in the sensing arm to compensate for dispersion [49].

The contribution to noise of the constant power on the detector, represented by the first two terms in (5-1), could be kept low only by reducing the bandwidth, i.e. increasing the image acquisition time. Considering that all BPFs have the same bandwidth, that all the unwanted interference signals (the 4^{th} term in (5-1)) are largely attenuated, and assuming that the target object reflects considerably less light than either of the mirrors ($O \ll R_j \cong 1$), a calculation in the shot noise limited case [55] based on the shot noise value resulting from the second term in (5-1) reveals that compared to the first interferometer, the signal to noise ratio decreases by about 4 dB in the second interferometer, by 7 dB in the 3^{rd} interferometer and 10 dB in the 4^{th} interferometer.

5.3.4 Concluding remarks

In conclusion, an OCT system capable of producing two simultaneous *en face* images of the human retina was demonstrated. While the increase in the number of layers explored and displayed simultaneously is shown to be possible, there are also problems, some of which can be fairly easily overcome. It was shown that the quality of the image obtained with the second interferometer might not be as good as the one in the first interferometer. If a decrease of the signal to noise ratio by 10 dB is acceptable between successive images, up to 4 depth layers could be displayed simultaneously with a source of 3.6 mW optical power.

Only a simple configuration was considered here, although more complex ones could be designed using an extra coupler in each interferometer and replacing the flat mirrors with corner cube mirrors. Had these devices been available at the time of this particular work package, a balanced photodetection technique [55] could have been implemented as well as making the interferometers independent of each other. The disadvantage would be that the modulation of OPDs would be more difficult than that presented here, as the corner cubes are relatively large devices.

6. Improving OCT performance and versatility for the imaging of the *in vivo* retina

6.1 Introduction

The high depth resolution provided by low coherence interferometry is both an advantage and a disadvantage for the imaging process. In principle, there is a great potential for improving depth accuracy, as this depends on the source used and not on the object, as is the case with the confocal scanning laser ophthalmoscope (cSLO). However, the shorter the coherence length, the more sensitive the system is to eye movements and the easier it is disturbed by vibrations. Consequently, an acceptable trade-off must be found between the depth accuracy and the ease of obtaining good and readily interpretable images of the eye.

In view of the fact that the longitudinal images generated by commercial OCT cannot be directly compared with the transversal images provided by the scanning laser ophthalmoscope (SLO), one of the goals of the entire project was to investigate the possibility of using OCT to deliver both longitudinal and transversal images.

While previous chapters have emphasised novel improvements to OCT imaging, this chapter will concentrate on a recipe to produce a versatile instrument capable of delivering useful images of the living retina using "conventional" phase modulation. In the process, the intention is also to discuss the problems associated with the phase modulation, which is generated when scanning the eye transversally, and look in more detail at how this modulation can be effectively used as a carrier for the image signal.

6.2 Overview of the optics and electronics hardware

Precursors of the configuration described below have already been discussed in Chapters 3-5. The set-up shown in Figure 6.1 is an amalgamated version of several design stages previously looked at, with some added improvements. The common element is naturally the core Michelson interferometer with its reference and object

arms. A new addition is the presence of the retro-reflector and extra coupler in the reference arm that ensure reference light is not returned towards the source.

Light from a pigtailed superluminescent diode, SLD, central wavelength $\lambda = 0.85$ μm, is injected into directional coupler DC1, which transmits a percentage η of the optical power to the object arm.

Light in the object arm propagates through phase modulator PM, which consists of two turns of fibre wrapped around a piezo-cylinder. This type of phase modulation has the advantage of not requiring light to be coupled out and back into the fibre, rendering it a simple solution to implement.

Light subsequently travels through microscope objective C1, enters an

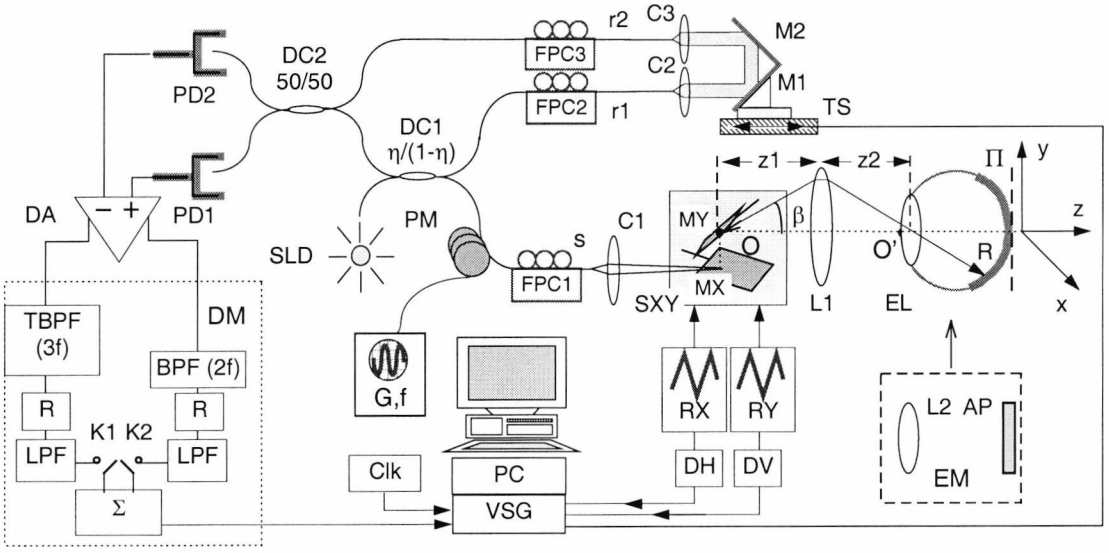

Figure 6.1 Block diagram of the OCT system; SLD: Superluminescent diode (Superlum SLD-361); C1, C2, C3: microscope objectives; DC1, DC2: directional couplers; PM: 5 cm diameter piezo-cylinder with 2 turns of fibre acting as a phase modulator; G: sinusoidal generator, f = 30 kHz; M1, M2: mirrors; L1: convergent lens; FPC1,2,3: polariser controllers; SXY: orthogonal scanning mirror pair; MX(MY): mirror of the X(Y) scanner; DM: demodulation block; RX, RY: ramp generators; PD1, PD2: photodetectors; DA: differential amplifier (PD1, PD2 and DA are parts of a Nirvana™ New Focus balanced photodetector module); TBPF: tuneable bandpass filter; BPF: bandpass filter; R: rectifier; LPF: low pass filter; Σ: analogue adder; K1, K2: switches; DH: monostable circuit for the VSG line trigger; DV: monostable circuit for the VSG frame trigger; Clk: VSG clock generator; EL: eye lens; R: human retina; EM: eye model; L2: lens; AP: aluminium plate; Π: imaginary plane perpendicular to the optic axis and tangential to the retina; TS: computer controlled translation stage; PC: personal computer.

orthogonal scanning mirror pair, SXY, and passes through converging lens, L1 (antireflection coated for 0.85 μm, of 6 cm diameter and 60 mm focal length) which brings the fan of rays to convergence at the eye lens. The reference beam, which emerges from port r1 of DC1, is of much higher power than the signal beam and is directed via microscope objectives C2 and C3 and mirrors M1 and M2 to receiving coupler DC2, thus avoiding feedback to the SLD (it is known that SLDs are prone to oscillations and that their correlation profile suffers from back reflections). Fibre end r1 is polished at a 10° angle to reduce the noise associated with backreflected light.

In the reference arm, mirrors M1 and M2, forming a retro-reflector arrangement with reduced sensitivity to tilt, are mounted on a computer controlled translation stage, TS, which can be moved continuously at a constant speed or discreetly in steps greater than or equal to 1 micron. Polarisation controllers, FPC, are present in the sensing arm and in each of the reference arm ports.

The spot where the beam falls incident on mirror MX is denoted O and is situated at a distance z_1 in front of the lens L1. The point O' where the rays enter the eye, at a distance z_2 behind lens L1, is a conjugate point to O by virtue of L1. OO' defines the optic axis of the system, which runs in the z direction in the chosen system of co-ordinates (Figure 6.1).

Two photodetectors, PD1 and PD2, collect the returned optical signals and their outputs are applied to the two inputs of a differential amplifier, DA, in a balanced detection configuration. The signal is then demodulated in the demodulator block, DM, and subsequently applied to a variable scan digital frame grabber, VSG.

Ramp generators RX and RY drive the transversal scanners X and Y respectively, and also trigger signal acquisition by the frame grabber, VSG. Several components (DC1, FPC1, C1, SXY and L1) are mounted on the chin rest used to accommodate the patient's head. A special mount was also devised for supporting different objects under investigation, such as the eye model, EM, which consists of an aluminium plate diffuser, AP, placed at the back of a lens, L2.

6.2.1 Modes of operation

The system may be operated in three different regimes, described below, with different settings for the drive parameters of translation stage TS and transversal scanner SXY. Demodulation block DM also requires re-configuring to switch between modes.

6.2.1.1 Transversal imaging (TI).

In this regime, the galvo-scanning mirror pair SXY can be used to generate a frame, which could be of any shape, such as for example a disk, in the plane perpendicular to the optic axis. Here only conventional rectangular frames were produced, with the X scanner driven by ramps of up to $F_x = 600$ Hz and the Y scanner driven by slower ramps, with a frequency $F_y = 1.18$ Hz. The number of lines in the raster could easily be adjusted by controlling frequency F_y.

As will be seen later in paragraph 6.3.2, depending on the required image size along the X-axis, which is governed by the amplitude U of the signal applied to the X-scanner, the demodulation block DM can be configured in two possible ways.

6.2.1.1.1 Signal processing with conventional phase modulation

For values of U less than 0.62 V, a conventional phase modulation technique is employed. Piezo-cylinder PM is driven by a sinusoidal signal at frequency f = 30 kHz. Two band pass filters are used: the fixed frequency BPF is tuned to 2f and the tuneable band pass filter, TBPF, is tuned to 3f. Both signals are present in the adder with both switches K1 and K2 at the adder input closed.

The residual intensity modulation from the phase modulator, at f, is avoided in this way. The amplitude of the driving signal applied to PM is adjusted to give the same modulation amplitude at 2f = 60 kHz and 3f = 90 kHz (this corresponds to an amplitude of the phase modulation of ≈ 3 rad).

The two band pass filter outputs are rectified (R) and low pass filtered (LPF). The analogue adder (Σ) adds the two signals and the resulting sum is applied to the frame grabber. Since the demodulated signals at 2f and 3f have complementary variations in respect to the phase fluctuations [23], the amplitude of the demodulated signal after the adder Σ is less sensitive to vibrations and thermal fluctuations.

For values of U higher than 0.62 V, only the tuneable band pass filter, TBPF, tuned to 90 kHz is used, with K1 closed and K2 open. In this case, the Newton rings modulation introduced by transversally scanning the target, discussed in Chapter 4, is employed either in addition or on its own (see paragraph 6.3.3).

6.2.1.2 Longitudinal imaging

Longitudinal images can be collected in two different ways, depending on the translation stage speed:

- SLI: slow longitudinal scan imaging with a slow moving translation stage TS and a fast transversal scan across X or Y. Each longitudinal scan results in an image where the horizontal lines are given by either the X or Y scans at 600

Hz. The configuration of signal processing depends on the voltage applied to the galvo-scanner, as is the case in the TI regime;

- DI: fast longitudinal scan imaging, with the modulation carrier generated by a Doppler shift. In this regime, the transversal scanner is run at a lower speed, or in fine steps. One complete run yields the image, while the lines are generated by repetitive movements of the translation stage TS. This regime, also used in the eye length measurements covered in Chapter 3, was generally favoured in OCT set-ups used for producing line scans [61]. The tuneable band pass filter is tuned to the Doppler frequency; switch K1 is closed and switch K2 is open.

6.3 Signal to noise ratio and bandwidth analysis

The photo-currents in detectors PD1 and PD2 are given respectively by i_1, i_2:

$$i_1 = \alpha P[\eta(1-\eta)\mu E + (1-\eta)(1-\mu)R + \\ +2(1-\eta)\sqrt{\eta\chi\mu(1-\mu)OR}\gamma(OPD)\cos(\varphi_o - \varphi_r - \frac{\pi}{2})] \quad (6\text{-}1)$$

$$i_2 = \alpha P[\eta(1-\eta)(1-\mu)E + (1-\eta)\mu R + \\ +2(1-\eta)\sqrt{\eta\chi\mu(1-\mu)OR}\gamma(OPD)\cos(\varphi_o - \varphi_r + \frac{\pi}{2})] \quad (6\text{-}2)$$

where P is the SLD power, φ_o the phase in the sensing arm and φ_r the phase in the reference arm. A phase shift of π was assumed to take place at each reflection (at the object and at mirrors M1 and M2). Additional symbols in the two equations above are as follows: O is the reflectivity of the object, E is the reflectivity of the fibre end at port s, μ is the splitting ratio of coupler DC2, χ is the efficiency of coupling the object power back into port s and R is the aggregate transfer efficiency of the reference beam from port r1 to port r2, which comprises the reflectivity of mirrors M1 and M2 and the loss in coupling the light into port r_2. Parameter α represents the responsivity of the photodetectors, which are assumed to be identical and γ(OPD) is the modulus of the correlation function of the field for an optical path difference of OPD. In (6-1) and (6-2) the assumption was made that R >> E >> O. After subtracting the photocurrents the differential amplifier delivers a signal proportional to:

$$\Delta i = \alpha P[\eta(1-\eta)(2\mu-1)E + (1-\eta)(1-2\mu)R + \\ +4(1-\eta)\sqrt{\eta\chi\mu(1-\mu)OR}\gamma(OPD)\sin(\varphi_o - \varphi_r)] \quad (6\text{-}3)$$

The case of $\mu = 0.5$ corresponds to a balanced coupler DC1. The first two terms which represent the contribution of the bias are eliminated in this balanced case [55], and the mean square current fluctuation, $\langle \Delta I_n^2 \rangle$, is expressed as:

$$\langle \Delta I_n^2 \rangle = 2\, e\, B[\langle I_{ref} \rangle + \langle I_E \rangle] + 4\, B\lambda^2 \frac{\langle I_{ref} \rangle \langle I_E \rangle}{c\Delta\lambda} \quad (6\text{-}4)$$

where e is the electron charge, B the electrical bandwidth, $\Delta\lambda$ the optical linewidth. The currents I_{ref} and I_E are the currents at both detectors taken together, resulting from the reference optical signal and from fibre end back reflections respectively.

6.3.1 Shot noise and excess photon noise

When the following condition is met:

$$\langle I_E \rangle << \frac{e\, c\, \Delta\lambda}{2\,\lambda^2} = 0.664\ \mu A, \quad (6\text{-}5)$$

the first term in equation (6-4) dominates, i.e. the system operates in the shot noise limited regime. This result is obtained assuming that $I_E << I_{ref}$; a value of $\Delta\lambda = 20$ nm was substituted in (6-4).

Looking at the first two terms in (6-1) and (6-2) which represent non-target light and assuming values of E = 3.5 % for fibre end reflectivity, $\eta = 25\%$ for coupler DC1 and $\alpha_{Silicon} = 0.5$ mA/mW, relation (6-5) leads to an upper limit for the source power P_{SNL} in the region of 200 μW. Higher power values would be obtained, for the same value of I_E, if the fibre end reflectivity were smaller. Whilst it is true that polishing the fibre at an angle lowers the end reflectivity, its counterproductive effect is that it reduces the efficiency of coupling the light back into the system. Higher collection efficiency from the object was considered a priority for this application and thus only the fibre end in port r1 was angle-polished.

Taking into account that the simplified model above neglects losses in the couplers and thermal and electronic noise, the instrument was operated above the derived value for P_{SNL}. The source power was increased to 360 μW, causing the

excess photon noise to become slightly larger than the shot noise. The amount of light incident on the eye is then 90 μW which is a level similar to that used by other research groups [63], [64] and most importantly is within the 400 μW level for 100 s irradiation permitted by the Laser safety regulations (Euronorm EN 60825-1), at wavelengths in the 800 nm band.

Evaluating the signal to noise ratio in the manner described in [55] we obtain (for $\mu = 0.5$, balanced DC1):

$$\frac{S}{N} = \frac{\alpha O \chi (1-\eta)\eta P}{eB[1+2\lambda^2 \alpha \eta (1-\eta)EP/(ec\Delta\lambda)]} \tag{6-6}$$

The size, d, of a pixel defined by the spot on the retina (or as it is represented in Figure 6.1, behind lens L2), is the diffraction limited spot size for a diameter of the beam D focused by a lens of focal distance L_2 and is given by:

$$d = 1.22\lambda \frac{L_2}{D} \tag{6-7}$$

Taking into account the number of pixels N_x which constitute a line scan of length ΔX in the imaginary plane Π in Figure 6.1, the image bandwidth can be evaluated as:

$$B_i = N_x \frac{1}{2T_x} = \frac{\Delta X}{d}\frac{1}{2T_x} = 0.41\frac{D}{\lambda}\frac{\Delta X}{T_x L_2} \tag{6-8 a,b,c}$$

where T_x represents the time taken to scan a line. This bandwidth will arise either side of the carrier, since the carrier is modulated in intensity by image reflectivity variations.

The relationship between the scan length ΔX and the amplitude U of the driving ramp generating it is obtained as:

$$U = \frac{z_2}{z_1}\frac{\Delta X}{2\gamma L_2} \tag{6-9}$$

where γ is the scanner sensitivity.

In order to get the maximum speed out of the X-scanner and obtain a 512 line image in less than 1 s, the scanner is driven at a frequency F_x higher than the roll-off

frequency, in which case k depends on F_x, higher values of F_x resulting in smaller values of k.

For F_x = 600 Hz for instance, γ = 45.38 mrad/V (1.54 times smaller than at 10 Hz) and the galvo-scanner flyback time is about 20% of the line period. A monostable circuit, DH, with a delay of 340 μs to trigger the line display of the grabber, ensures images are not displayed during fly-back. Consequently, the duration of a line scan is T_x = 1.33 ms.

6.3.2 Relationship between bandwidth and spot size

The carrier frequency f should be chosen in such a way that the band near the frequency 2f does not overlap with the band near 3f, which implies that:

$$f > 2B_i \tag{6-10}$$

Since our piezo-cylinder element is limited to 30 kHz (although higher piezo-modulation frequencies have been reported in literature [63]), B_i will be below 15 kHz. Such a bandwidth would limit the size of the image to ΔX = 0.42 mm (N_x= 40 pixels) and the amplitude of the X-scanner voltage to U_1 = 0.16 V. These numerical results are obtained here using equations (6-8 a,b,c) and (6-9), for λ = 0.85 μm, D = 2 mm, z_2 = 10.2 mm, z_1= 14.5 mm, L_2 = 20 mm, a bandwidth of 15 kHz.

For larger ΔX values, higher carrier frequencies and values for B are required. In order to limit the distortion of the deflected beam due to the size of lens L1, the amplitude applied to the scanner was limited to U_M = 1.3 V, resulting in a span ΔX = 3.35 mm (equation (6-9)). Consequently the value of B_i goes up to 121 kHz (equation (6-8 a,b,c)), and the 30 kHz modulation cannot act as a carrier any longer. For images of larger sizes, therefore, in the absence of a faster device, a different method of providing phase modulation has to be used.

6.3.3 Using Newton rings sampling for larger images

It was shown in Chapter 4 that those parts of the object situated at coherence with the reference surface are sampled with a function whose Newton rings appearance is a consequence of a quadratic OPD dependence on the scanning mirror deflection angle β. When the beam is scanned across the sampling function, the photodetected signal is modulated at a frequency ν. Following on from equation (4-20) one can obtain the maximum value of this frequency, ν_g, as:

Figure 6.2 The frequency ν_g due to galvo-scanner modulation and the image bandwidth, B_i against the amplitude of the driving signal, U.

$$\nu_g = \frac{4kU}{\lambda T_x} L_2 \frac{z_1^2}{z_2^2} |\beta_m| \tag{6-11}$$

where $|\beta_m|$ is the maximum angle for which interference still occurs. Interference signals are produced for $|OPD| < l_c$, where l_c is the coherence length of the source, and the angle β for which $|OPD| = l_c$ is β_C:

$$\beta_C = \sqrt{\frac{l_c}{L_2}} \frac{z_2}{z_1} \tag{6-12}$$

For $|\beta| > \beta_C$, $|\beta_m| = \beta_C$ and for $|\beta| < \beta_C$, $|\beta_m| = kU$. According to (6-11), this means that for $U < U_C = \beta_c/k$, ν_g has a quadratic dependence on U and for $U > U_C$ the dependence becomes linear. This can be understood by the fact that for $|\beta|$ values above β_C, the explored areas correspond to $|OPD|$ values outside coherence and consequently they do not contribute to the interference signal. Up to β_C, interference is obtained during the entire duration of a transversal scan, T_X. Above β_C, the time interval during which interference takes place, and also the period $1/\nu$ of the modulation signal, are proportional to β_C/β and consequently both decrease with increasing U. As a result, the dependence ν_g (U) becomes linear. This behaviour is illustrated in the graph in Figure 6.2.

For $U > U_C$, components up to ν_g are generated (from (6-11) and (6-12)):

$$\nu_g = 4k \frac{U}{T_x} \frac{z_1}{z_2} \frac{\sqrt{L_2 l_c}}{\lambda} \tag{6-13}$$

With $l_c = 31.9$ μm and the numerical values above, $U_C = 0.62$ V and for $U_M = 1.3$ V, the value for ν_g is 236 kHz.

Table 6-1 displays the numerical values for the ΔX span size at the back of lens L2 of 2 cm focal length, B_i and ν_g in respect to the voltage applied to the X-scanner. ΔR represents the gap between adjacent Newton rings at the edge of the sampling function for each amplitude value U, and this is ultimately the parameter that imposes a limit on the smallest resolvable feature size.

Table 6-1

Key bandwidth values on the horizontal axis of the graphs in Figure 6.2.	U(V)	ΔX(mm)	B_i(kHz)	ν_g(kHz)	ΔR Newton rings (μm)
1 (B_i =15 kHz)	$U_1 = 0.16$	0.416	15	7.5	58
2 (B_i= 22.5 kHz)	$U_2 = 0.24$	0.62	22.5	17	39
3 ($B_i = \nu_g$)	$U_3 = 0.32$	0.83	30	30	29
4 (ν_g =60 kHz)	$U_4 = 0.45$	1.16	42	60	21
5 (ν_g =90 kHz)	$U_5 = 0.55$	1.43	52	90	17
C (ν_g becomes linear in U)	$U_C = 0.62$	1.6	57	113	15
M (max voltage applied)	$U_M = 1.3$	3.35	121	236	7

6.3.4 Comparison of the two types of modulation

The arrangement (EM) in Figure 6.1 was used to determine the galvo-scanner modulation parameters experimentally. The X-scanner was driven by ramp signals of frequency F_x = 600 Hz and different amplitudes U, without driving the Y-scanner.

Several components in the spectrum of the photodetected current were measured both with and without the sinusoidal PM modulation at 30 kHz. Specifically, the signal contained in a bandwidth of 6 kHz about 60 kHz (i.e. 2f) on one hand and in a bandwidth of 9 kHz about 90 kHz (i.e. 3f) on the other hand were recorded, averaged over 100 measurements and plotted in the graphs in Figure 6.3.

These graphs show that for voltages higher than U_C = 0.62 V (ΔX = 1.6 mm), the PM modulation does not have any noticeable effect on the demodulated signal, ν_g acting as an efficient carrier. Little enhancement is brought about by PM in the range U_3 to U_C. For $U < U_3$ =0.32 V, $\nu_g < B_i$ and ν_g cannot act as a carrier. Consequently, for $U < U_3$, the modulation introduced by PM becomes more important, as proved by the graphs in Figure 6.3. The modulation is essential for the case $U < U_1$, when (6-10) is satisfied and $\nu_g << B_i < 15$ kHz.

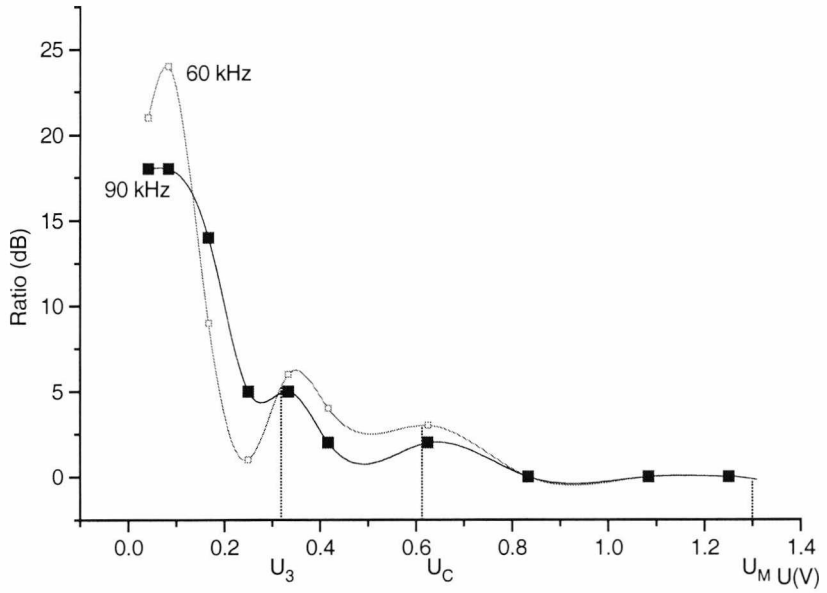

Figure 6.3 Ratio of the amplitudes of the 60 kHz and 90 kHz components in the photodetected signal spectrum with and without the sinusoidal PM modulation, versus the amplitude of the ramp driving signal, U.

6.3.5 Pixel size

When $U > U_C$, the tuneable band pass filter TBPF should be tuned to 90 kHz and operating at a quality factor value Q = 2, to give a value of B = 45 kHz. Higher bandwidth values are not possible owing to the differential amplifier in the balance photodetection block (New Focus Nirvana, 125 kHz). This means that in order to generate a frame in the minimum time allowed by the speed of the galvo-scanner, image bandwidth should be sacrificed, which we have seen that reduces transversal resolution. Consequently, the pixel size on the target is increased from the value given by (6-7), d = 10.4 μm, to an effective value d_{eff}.

Taking into account that the receiver acts as a low pass filter of bandwidth B/2, thereby lowering the processed signal bandwidth from B_i to B/2, the effective pixel size is $d_{eff} = (2B_i/B)d = 56$ μm. For the maximum image size of 3.35 mm imposed above (when $U = U_M = 1.3$ V), the corresponding number of pixels is $N_x = 60$, although this is a very conservative calculation. When $\nu_g = 90$ kHz (point 5 in Table 1), it can be shown using equation (4-22) that the gap ΔR between adjacent Newton rings is 17 μm, which allows sampling of pixels of sizes down to 34 μm. The pixel

size varies in fact between 34 and 56 μm across the target, depending on the inclination of different object features relative to the coherence wavefront.

The diffraction limited pixel size given by (6-7) could be achieved for $U = U_M$ and B = 45 kHz when the X-scanner is driven at line rates below 111 Hz. In this case, the time taken to produce a frame increases proportionally with $1/F_x$.

6.3.6 Acquisition time

The total time to produce a frame for the transversal imaging regime is:

$$T_T = \frac{N_y}{F_x} \tag{6-14}$$

with N_y the number of lines in the frame. At a line rate of F_x = 600 Hz a 768 × 512 pixels image is generated in T_T = 0.85 s.

6.3.7 Minimum detectable signal

For a given bandwidth B, the minimum signal that could be detected by the system is obtained from (6-6) for a signal to noise ratio of one. For the example considered above, with χ = 0.4, P = 360 μW and B = 45 kHz a minimum detectable value of the object reflectivity O_{min} = -90.2 dB is obtained. When U < 0.16 V, the quality factor Q of the band pass filters could be increased to enhance the signal to noise ratio.

6.4 Issues affecting cross section imaging with *en face* OCT

For longitudinal images in the SLI regime, the bandwidth and the minimum detectable signal are the same as in the transversal imaging case. Different speeds can be used. An acquisition time of 0.8 s, approximately equal to T_T, allows the use of the same VSG settings for longitudinal imaging as those for the transversal imaging.

In order to allow enough time for the translation stage to gain speed, the image is produced after a 0.2 s delay introduced by the monostable circuit DV. The clock signal controlling VSG is the same as the one used in the transversal imaging regime, so the displayed ΔZ in mm (the frame height) is 0.8 s multiplied by the speed in mm/s. The translation stage speed should be limited to such a value that during the time taken to produce a transversal line, $1/F_x$, the reference path is modified by less than half the longitudinal pixel size which is around half of the coherence length of the source, l_c:

$$v_{max} = \frac{l_c}{4} F_x = 4.78 \text{ mm / s} \tag{6-15}$$

For this value, it can be shown that the Doppler frequency is much less than the bandwidth B_i, so the tuneable band pass filter in the demodulation block does not need re-tuning. Depending on the depth size ΔZ, the number of pixels N_z is given by

$$N_z = \frac{2\Delta Z}{l_c} \tag{6-16}$$

For longitudinal images in the DI regime VSG displays the object Z-axis along the horizontal direction and the object X or Y axis along the vertical direction. For this regime, devices for fast longitudinal OPD variation are needed [63], [65]. The translation stage used here has a limited speed, resulting in too long a time to produce a frame from a moving target but can employed successfully to produce a coherence reflectogram along the Z axis as described in Chapter 3.

6.5 Adjustment and image settings. Wavefront distortion

The transversal images collected from the eye need correction owing to the curvature of the coherence surface behind the eye lens. Again the eye model arrangement can be used to illustrate this. Ramps of 1.3 V amplitude were applied to both galvo-scanners and translation stage TS shifted in 24 steps of 5 μm. The transversal images evolve from a disk through circles of expanding radius when the reference path is increased, as shown by four of the images presented in Figure 6.4.

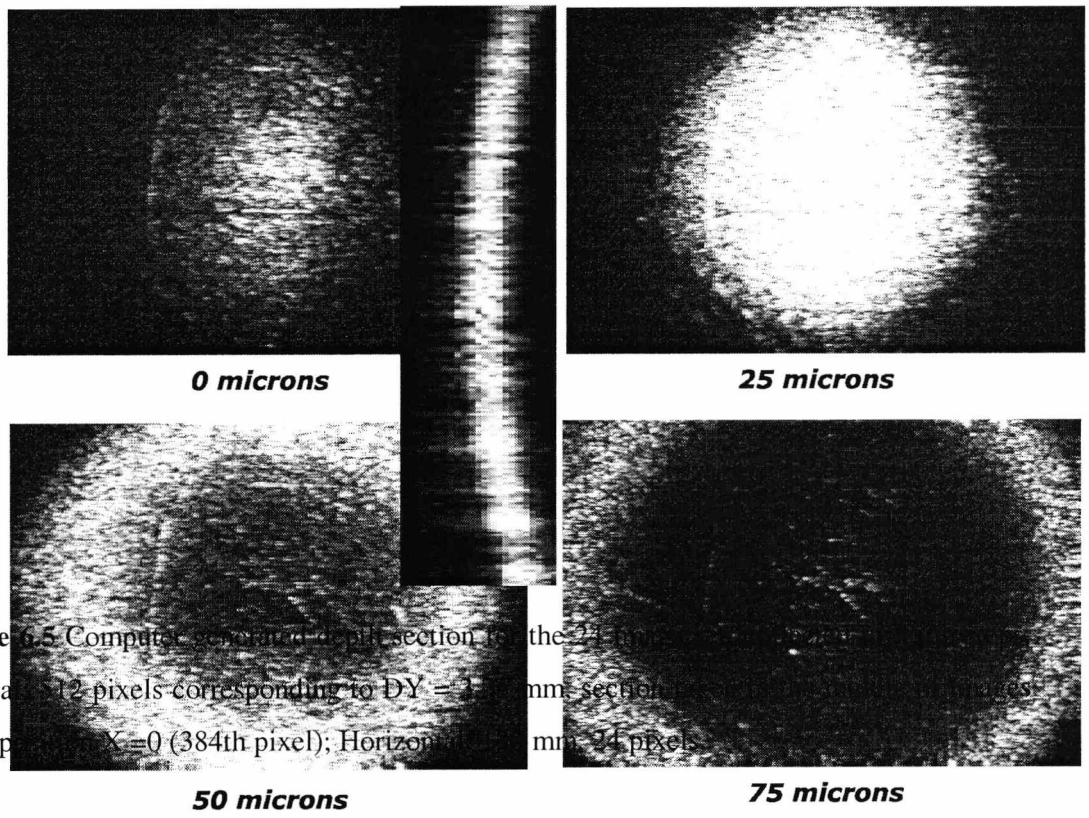

Figure 6.5 Computed pseudo-longitudinal depth section for the 24 images
Vertical: 512 pixels corresponding to DY = 3.35 mm; section
at the p X =0 (384th pixel); Horizon mm, 24 pixels

Figure 6.4 Images collected from the aluminum plate in the TI regime for 4 different positions of the translation stage. Amplitude of the ramp voltage applied to both scanners: 1.3 V (raster size of 3.35 mm by 3.35 mm on the aluminium plate); modulation imprinted by the galvo-scanner only, $F_x = 600$ Hz, $T_y = 0.85$ s

A computer program then generates the pseudo-longitudinal image shown in Figure 6.5. For any (x,y) pixel in the image, the program calculates the amplitudes of the coherence signal for all 24 depth positions. In Figure 6.5 this dependence on z is observable for all the pixels along the line (384, y) with y from 1 to 512. A similar image was obtained in the SLI regime moving the translation stage TS at a speed v = 0.35 mm/s over 280 μm.

Figure 6.4 and Figure 6.5 clearly show that the longitudinal slice looks curved. This curvature has to be taken into account when deconvoluting raw retinal images. With the system at the extremity of the target, i.e. for the ray deflected when the driving voltage is at a maximum, half of the OPD is about ε = 70 μm greater than for the central ray. This value is in agreement with ε given by:

$$\varepsilon = L_2\left[1-\cos\left(\frac{z_1}{z_2}kU\right)\right] \qquad (6\text{-}17)$$

for U = 1.3 V and L_2 = 2 cm.

The distortion is due to the particular optics used, with the fan of rays convergent on the eye. Had a telecentric optical system been used, the surface reconstructed in the longitudinal image would appear as a plane. Unfortunately, a telecentric system is not applicable to the eye due to the small aperture (pupil diameter) available.

6.6 OCT images of the *in vivo* retina

All the images presented from hereon were collected with 90 μW of optical power incident on the eye. No averaging and no enhancement procedures were applied. The images' size is 768 by 512 pixels. The intensity of each pixel represents the 8-bit digital value of the analogue signal at the output of the demodulation block.

6.6.1 En-face images at different depths

Batches of 30 en-face images were collected from the living eye at different Z depths obtained by stepping translation stage TS by 50 μm every 1 s. After storage, the images were inspected and the batches showing disturbances due to eye movement discarded. Figure 6.6 shows 6 images retained from a larger batch, accompanied by the respective section depth values (the higher the value under each image, the deeper the location into the retina and the eye).

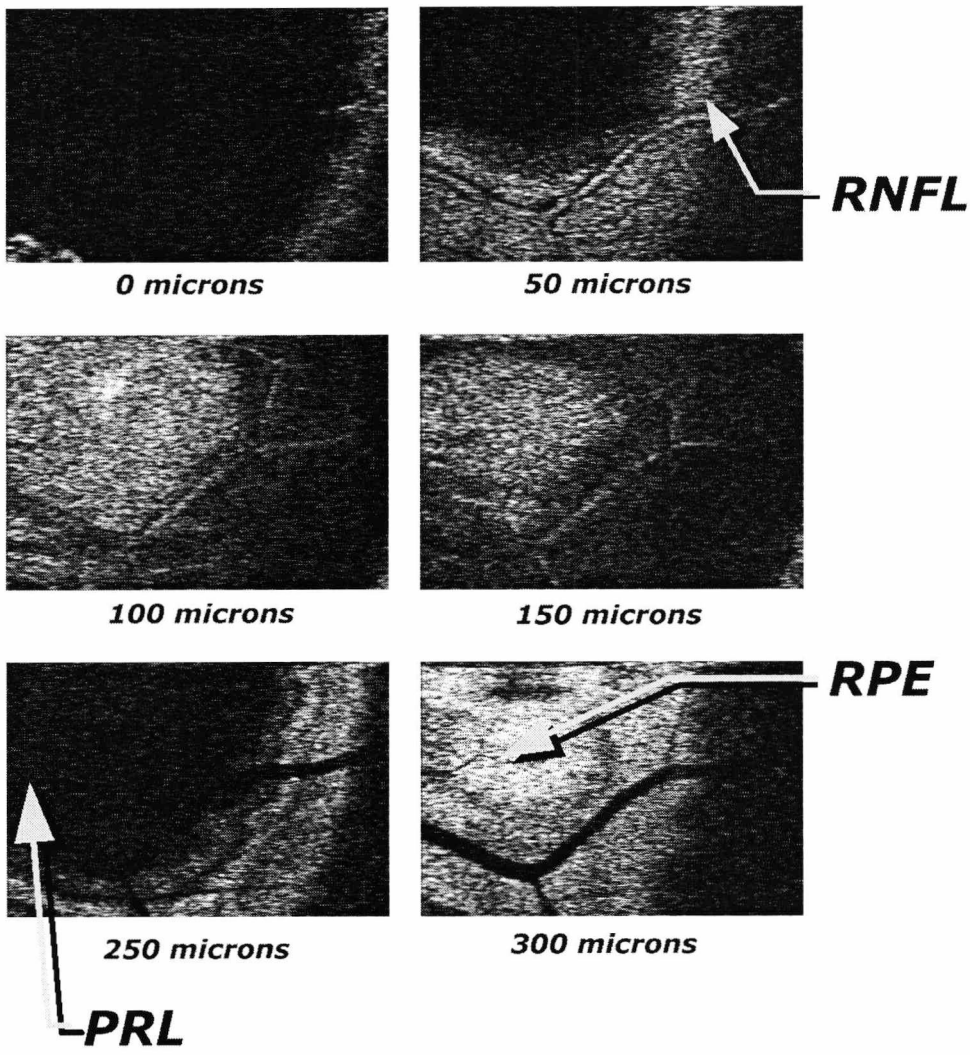

Figure 6.6 Transversal images collected from the left eye of a volunteer in 50 μm steps in depth. Details of a blood vessel are noticeable. The size of the image is approximately ΔX = 3.35 mm by ΔY = 2.57 mm. RNFL: retinal nerve fiber layer; PRL: photoreceptor layer (minimal backscatter signal); RPE: retinal pigment epithelium.

Pixel brightness is proportional to the amplitude of the coherence signal. From the 4th to the 5th image, the depth difference is 100 μm because during the collection of the image for the intermediate step the subject blinked and the image was discarded. There are noticeable differences between the images with different details coming into and out of coherence as the reference path is scanned. Owing to the curvature of the retina, fragments of retinal features are visible in a 400 μm longitudinal range. These images show that the blood vessel which appears dark in

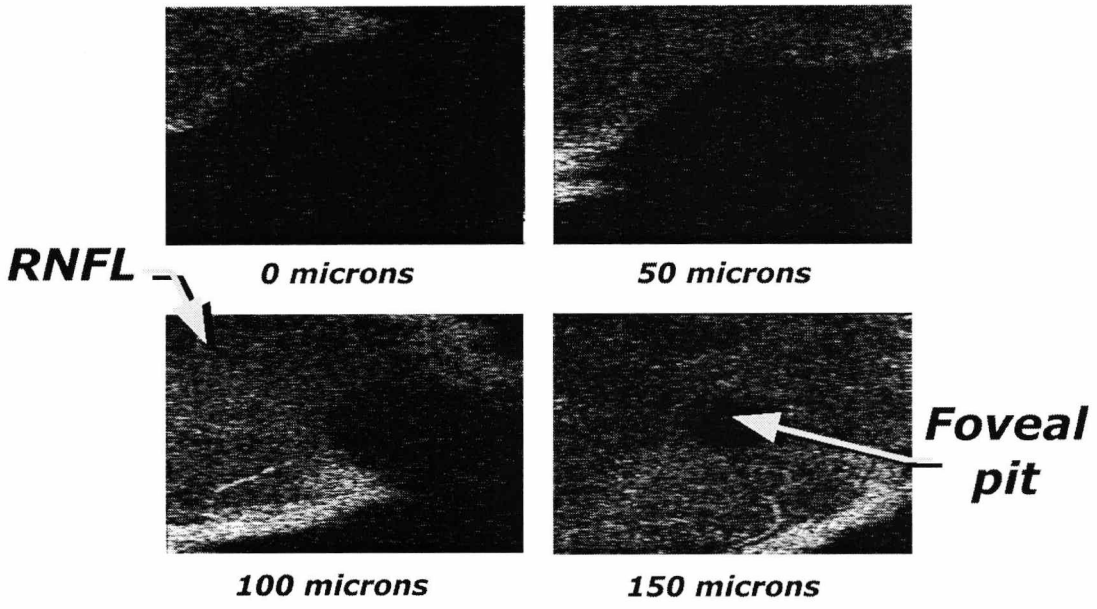

Figure 6.7 Transversal images collected from the left eye of a volunteer in 50 μm steps in depth. The foveal pit is noticeable. The size of the image is approximately ΔX = 3.35 mm by ΔY = 2.57 mm. RNFL: retinal nerve fibre layer

the last image in Figure 6.6 is about 200 μm thick (based on a value of 1.4 on average for the index of refraction of the retinal tissue).

Another batch of transversal images, of a different volunteer, is shown in Figure 6.7. In this case the eye was orientated so that when the transversal scanners were not driven the patient could see the spot in the centre of his visual field, thus bringing the foveal pit into the centre of the image.

6.6.2 Longitudinal images

Images from the same eye were collected in the SLI regime with the same orientation as in Figure 6.7. A set of 4 images is presented in Figure 6.8, with v = 0.625 mm/s for the top images, 1 and 2 mm/s for the bottom images, producing a frame of height ΔZ = 0.5, 0.8 and 1.6 mm respectively.

The characteristic foveal pit can be easily seen. For the images at the bottom of Figure 6.8 obtained with a 1.3 V amplitude signal applied to the X-scanner (ΔX = 3.35 mm, minimum 60 pixels,), only galvo-scanner induced phase modulation was employed.

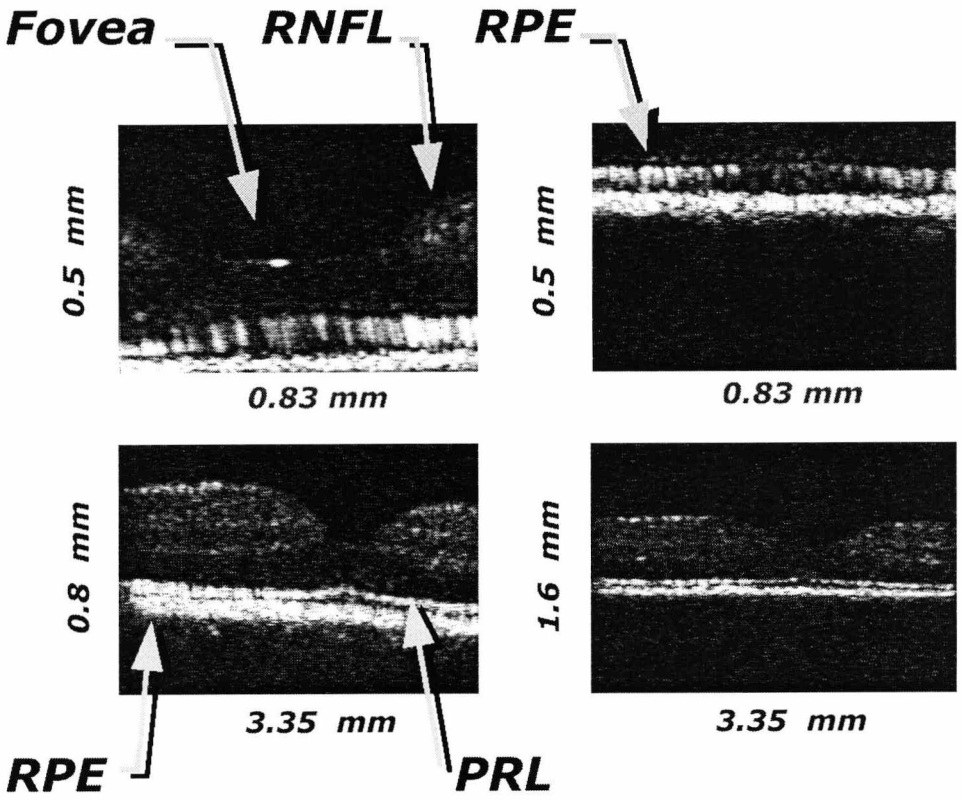

Figure 6.8 Longitudinal images of the retina for the eye in Figure 6.7 for different depths ΔZ as shown on each picture, taken at different speeds v(mm/s) = ΔZ mm /(0.8 s). (To obtain the geometric thickness, ΔZ must be divided by the index of refraction, ≈ 1.4); Y-scanner not driven. Top: U = U_3 = 0.32 V, PM modulated; Bottom: U = U_M = 1.3 V, PM not modulated

For the images at the top of Figure 6.8 obtained with U = U = 0.32 V (ΔX = 0.83

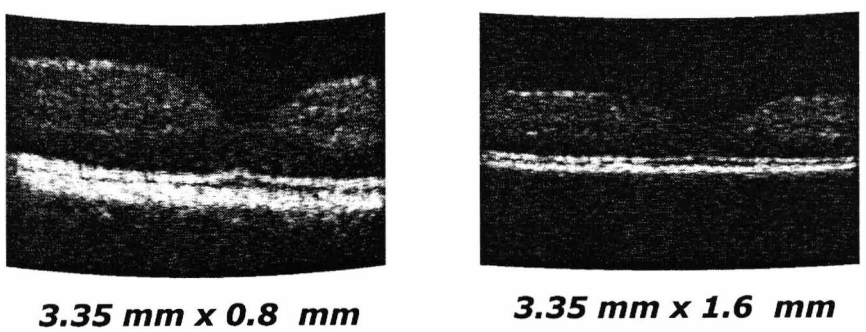

Figure 6.9 The two images at the bottom of Figure 6.8 corrected for the wavefront tilt shown in Figure 6.5.

mm) phase modulation generated was applied to enhance the signal. In this last case, B_i = 30 kHz, so that the pixel size was about d_{eff} = (60/45)d = 14 μm, i.e. there were

N_x = 59 pixels. The vertical pixel size was about $l_c/2$ = 16 μm, i.e. there were N_z = 31 vertical pixels in the two top images, 50 in the bottom left image and 100 in the bottom right image.

Figure 6.9 shows the images at the bottom of Figure 6.8 corrected for the wavefront distortion described earlier in Figure 6.5, using the equation:

$$\text{Correction}(X_{\text{pixel}}) = \frac{\varepsilon}{512\Delta Z}(X_{\text{pixel}} - 384)^2 \qquad (6\text{-}18)$$

for ε = 70 μm and ΔZ = 0.8 and 1.6 mm respectively. This is only an approximate correction, which depends mainly on the estimated focal length of the measured eye.

7. Conclusions

7.1 Introduction

A series of interference measurement techniques are shown to enable high resolution imaging of the human retina *in vivo*. The practical implementation of a multifunctional OCT instrument for clinical use is demonstrated.

The instrument is capable of generating transversal as well as longitudinal images of the living eye in less than 1 s, which goes some way towards the main objective of bringing nearer the goal of obtaining real time depth "slices" of the inner human eye. As well as eye measurements, other applications in the field of topometrics of either biological tissue or industrial targets can also be envisaged with the systems investigated.

7.2 Acquisition time issue

While the subjective quality of the majority of images collected with the techniques indicated here is good, eye movement still remains an issue for quantitative, reference measurements.

Since cross sectional tomographic images can be extracted from a volume of data at any conceivable angle, using a 3D profile to characterise morphological changes to a patient's eye tissues over a period of time is a very attractive goal. However, even at a frame rate of 0.85 s, building a 3D profile from multiple stacks of transversal frames, taken at successive depths, appears to be very difficult due to inconsistencies that can appear when the subject's eye changes orientation owing to the continuous movement generated by eye muscles.

A way of dealing with this problem is to collect a large number of images and to subsequently discard those showing significant departures from the set prediction due to eye movement. Such a task may be even automated with additional post-processing.

7.3 Eye imaging applications

Two imaging modes are discussed in Chapters 4 to 6 for images of the human retina: transversal and longitudinal. Both types of data are useful to clinicians and allow eye diseases such as glaucoma to be discovered early, with improved chances of providing an effective treatment. As well as the imaging OCT, an accurate eye-length measurement technique is proposed in Chapter 3 which minimises errors associated with longitudinal head movements.

7.3.1 Transversal images

In the galvo-scanning mirror based apparatus developed for clinical use two modulation procedures can be employed. On one hand, for small transversal size images, where the image bandwidth is less than 15 kHz, phase modulation is introduced by several turns of optical fibre wrapped around a piezo-cylinder. For larger sizes, on the other hand, it is demonstrated theoretically and experimentally that the path modulation introduced by the galvo-scanner itself can be used to obtain both longitudinal and transversal *en face* OCT images.

A frame rate of 0.85 seconds was obtained, albeit by sacrificing some transversal resolution and by driving the galvo-scanner at a speed such that 20% of the line has to be discarded during the scanner flyback. The main limitation to acquisition speed is the galvo-scanner and the bandwidth of the balanced detection receiver. It could be expected that both these issues can be overcome with increasingly available technology, not necessarily at a cost premium.

7.3.2 Longitudinal images

Longitudinal imaging at a speed of 1 mm/s speed proved to be remarkably easy, with no difficulty encountered in positioning the head and the eye to obtain an image. Naturally, the interpretation of individual OCT longitudinal images is considerably easier than that of OCT transversal images because the latter slice the data volume too fine.

7.4 Improvements and future work

The *en face* images presented in Chapters 4-6 demonstrate the potential of *en face* OCT to section the retina with very high depth resolution. Images taken at 50 μm depth intervals show clearly noticeable differences. However, to take advantage of this

resolution, further reduction of the acquisition time is necessary and the patient's head must be firmly fixed in place, thereby minimising target motion during data-taking.

7.4.1 Hardware

One way of improving image quality is to carry out a full analysis of ray geometry using a commercially available lens design package and to establish what correction, if any, can be applied at the post-processing stage.

Optical path distortion (caused by the scan head or imaging system) does also adversely affect the quality of the image and needs to be investigated further. The effect of such path length variations is to cause blurring and distortion in certain parts of image due to changes in the coherence surface.

7.4.2 Software

The LabView™ programs developed for simultaneous multi-layer imaging are an inexpensive substitute for a multi-channel programmable frame grabber. The data is collected and processed through a single channel but is subsequently displayed in the form of an array. This procedure can be successfully employed because data acquisition is inherently single point owing to the galvo-mirror type scanning.

However, due to bandwidth limitations imposed by the software sequencing controls it is almost always preferable to use a frame grabber instead. Some fairly complex frame grabber models are becoming available on the market which allow customisation and further processing of data, which is a useful feature when, as we have seen, some images require re-shaping.

7.4.3 Combined SLO/OCT

Although the OCT images, particularly the transversal ones, look fragmented, they show details unobservable with commercial scanning laser ophthalmoscopes (SLO), which have become increasingly available in recent years. For the OCT instruments of the type presented in Chapters 4-6 an image is obtained only when the path difference between the sensing arm and the reference arm is less than half of the coherence length of the SLD, which gives a slicing resolution of ≈ 17 μm in this case. We have shown that this fine depth resolution of the OCT results in the capability of displaying small fragments (under 0.1 mm size).

Details such as the curvature of the retina or the height of the optic nerve disk summit cannot be determined confidently with the SLO but can be measured using the longitudinal imaging mode of the OCT. For easy interpretation and efficient diagnosis

of OCT images, it would be ideal to have an SLO image simultaneously provided. One obstacle to this is for the time being the fact that SLOs work at video rate, 15 kHz, whilst the line scanning rates for the OCT are about a few hundred Hz. Inadvertent eye movements could potentially be evaluated from sets of SLO frames collected during an OCT frame, if means are provided for the synchronisation between the SLO and OCT.

The conclusion is that OCT has great potential to provide more insight into retinal diseases, but supplementary research is needed to make this technique suitable for diagnosis. Furthermore, while the real strength of OCT systems is in their ability to narrow the target depth range to a little more than ten microns, it would prove very useful to allow the operator and/or the practitioner to simultaneously refer to a more comprehensive view of the target tissue, such as the one provided by SLO. It would then become possible to conduct direct comparisons and highlight the advantages that each brings to the understanding of the patient's eye morphology, making the standalone dual OCT/SLO system potentially an important tool for the community of specialist ophthalmic practitioners.

Appendix A - Properties of the eye

A1. Anatomical properties of the eye [66]

Cornea

- The outermost eye tissue through which light passes. No blood vessels. It is comprised of several layers and, therefore, the optical properties are measured for the whole cornea rather than generalising from a tissue sample.
- Convexity of a radius of about 8 mm
- Refractive Index: 1.3771
- Posterior (back) surface distance along axis from corneal pole: 0.55 mm, radius of curvature: 6.5 mm
- Anterior (front) surface radius of curvature: 7.8 mm

The aqueous humour

- The aqueous humour is the fairly homogenous clear liquid between the cornea and the lens.
- The space that it inhabits is called the anterior chamber.
- Index of Refraction: 1.3374

Lens

- Near Point: upper limit of accommodation ~ 10 diopters = ~10.2 cm
- Far Point: lower limit of accommodation ~ 0 diopters = infinity
- Diopters = the power of a lens as defined by the inverse of the focal length in meters (focal length of 20 cm corresponding to 5 diopters)
- Index of Refraction: 1.42 Unaccommodated
- Index of Refraction: 1.427 Accommodated
- Anterior surface: distance from cornea: 3.6 mm unaccommodated, 3.2 mm accommodated
- Radius of curvature: 10.2 unaccommodated, 6.0 accommodated

- Posterior surface: distance from cornea: 7.6 mm unaccommodated, 7.7 mm accommodated
- Radius of curvature: -6.0 unaccommodated, -5.5 accommodated

The vitreous humour

- The vitreous humour is the clear liquid between the lens and the retina, filling a space called the vitreous body.
- Index of Refraction: 1.336

Retina

- In most primates the retina is about 200-250 micrometers thick.
- The primary layers and structures of the retina from outermost surface to innermost surface:

◊ Optic disk/blind spot - point at which the ganglion cell axons leave the eyeball oval which is taller than it is wide. Size 1.5 - 1.8 mm x 2 - 2.4 mm, 5 - 6 degrees x 7 - 8 degrees. Location: 4.8 mm nasal of visual pole and .47 mm above horizontal median

◊ Pigment epithelium - supporting cells for the neural portion of the retina (photo pigment regeneration, blood) dark with melanin, which decreases light scatter within the eye.

◊ Rod and cone layer/Bacillary layer, Layer of photoreceptor cells - contains the outer segments and inner segments of the rod and cone photoreceptors.

◊ Outer limiting membrane -

◊ Outer Nuclear Layer (ONL) - cell bodies of rods & cones

◊ Outer Plexiform Layer (OPL) - rod and cone axons, horizontal cell dendrites, bipolar dendrites

◊ Inner Nuclear Layer (INL) - Nuclei of horizontal, bipolar and amacrine cells

◊ Inner Plexiform Layer (IPL) - axons of bipolars (and amacrines), dendrites of ganglion cells

◊ Layer of Ganglion cells (GCL) - Nuclei of the ganglion cells and displaced amacrine cells

◊ Layer of retinal nerve fibres (RNFL) - fibres from ganglion cells traversing the retina to leave the eyeball at the optic disk.

A2. Irradiation of the eye

The maximum power of optical radiation that the eye can be safely exposed to is given in a variety of laser safety standards of which the American National Standards for Safe Use of Lasers (ANSI) is the widest quoted by researchers in this field. It sets the maximum permissible level for continuous exposure intrabeam viewing through a 7 mm pupil at 830 nm at 200 μW. Since localised damage from optical radiation is related to the energy absorbed by a small area of retinal tissue above a certain threshold, the maximum level is considerably higher at 1.3 mW [67] in the case of a non-interrupted scan across the retina [68].

A3. In-vitro eyes (post-mortem)

All in-vitro eyes were prepared from samples supplied by Dr Fred Fitzke of the Institute of Ophthalmology, London. The retina and its supporting tissue were separated from the rest of the eye and placed in formalin in a purpose-built steel container with a flat, transparent inspection window at the front.

Pictures are shown below of the biological sample viewed through the inspection window. The volume surrounding the sample is filled with formalin.

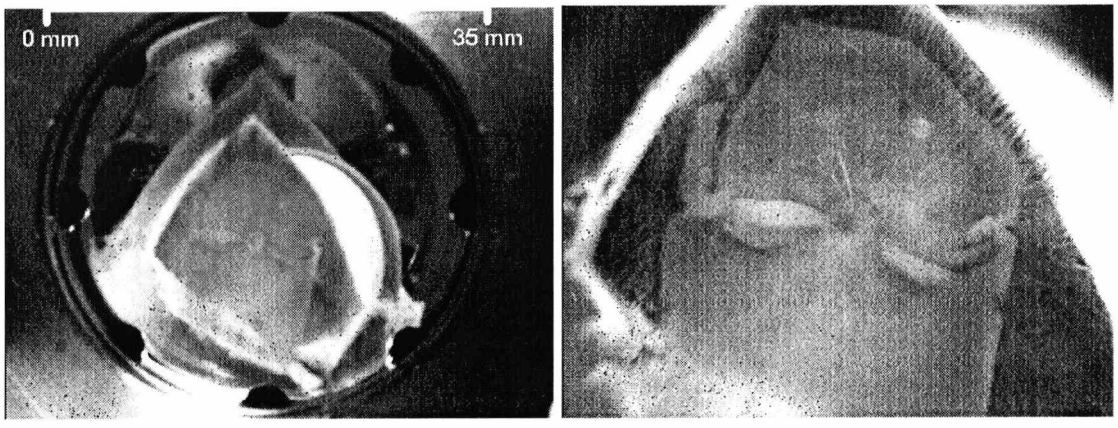

Figure A.1 Post-mortem retinal tissue: Left: the piston pushes the sample from behind right up against the transparent window. Right: a magnified view of the retinal tissue showing details such as the optic nerve head.

Appendix B - LabView™ frame grabber emulator program

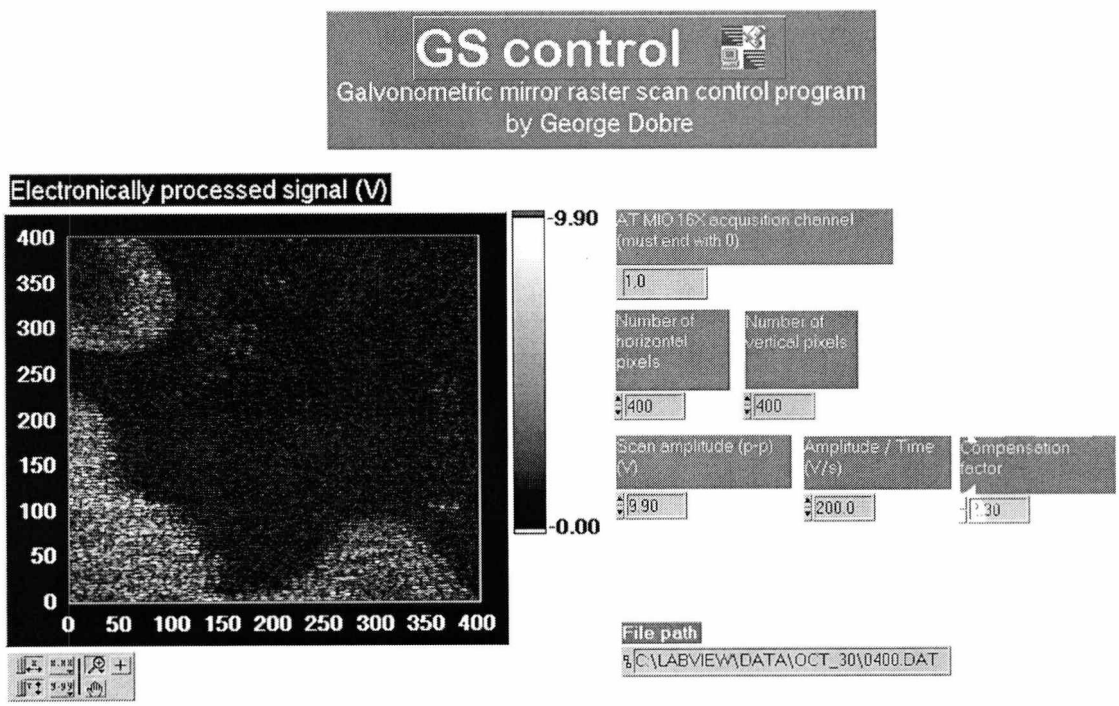

Figure B.10. Front panel screen capture of raster scan and acquisition control program written in LabView. The program above is a precursor of the routine used for the simultaneous imaging of multiple layers. Data is displayed in the window to the left every time one frame is completed.

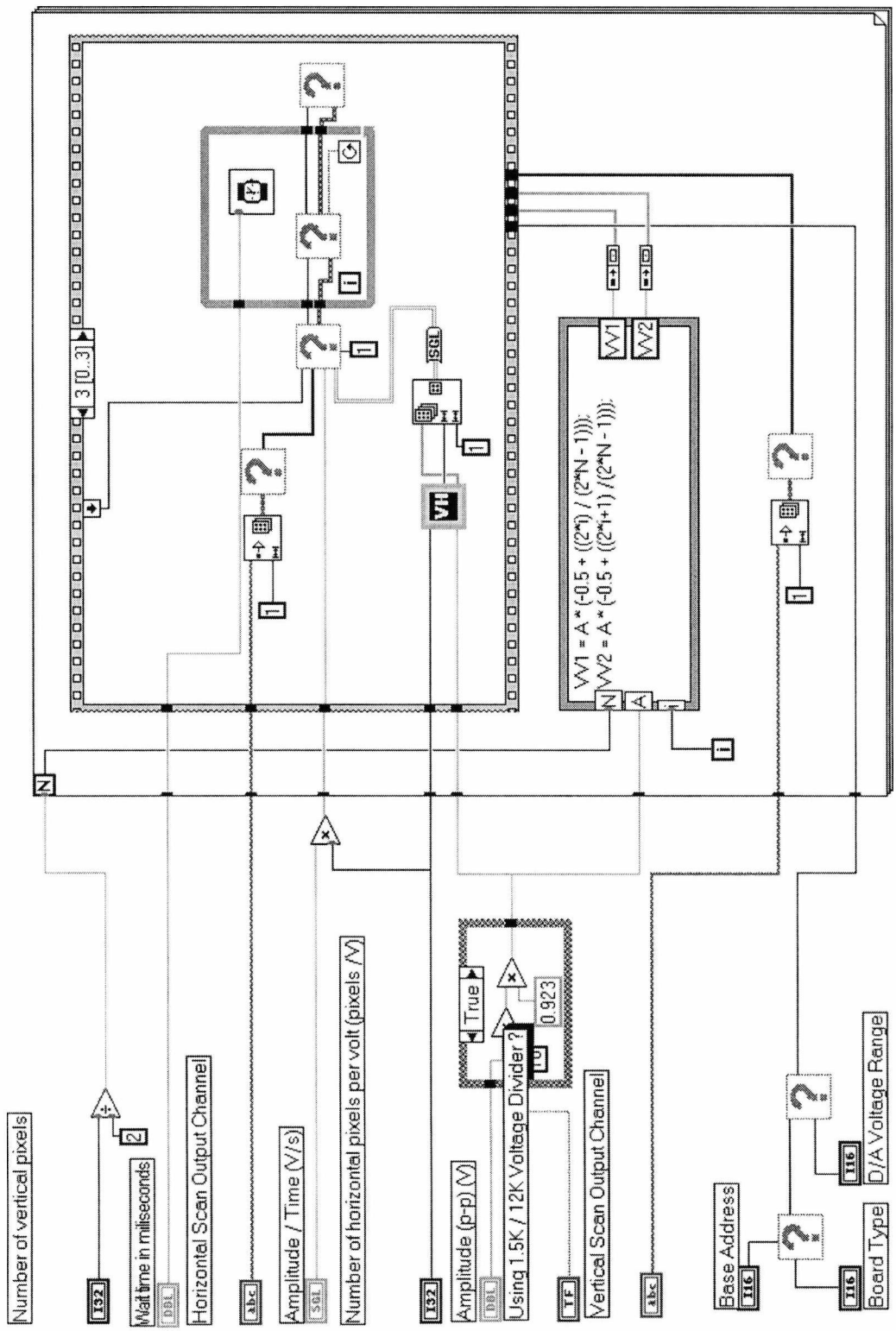

Figure B.2. Diagram of LabView Virtual Instrument shown in Front Panel format in Figure B.1.

Appendix C - Publications arising from this work

A. Gh. Podoleanu, M. Seeger, G. M. Dobre, D. J. Webb, D. A. Jackson, F. Fitzke "Transversal and Longitudinal Images from the Retina of the Living Eye Using Low Coherence Reflectometry, republished in "Selected Papers on Optical Low-Coherence Reflectometry & Tomography", B. R. Masters and B. J. Thompson eds., SPIE Milestone Series, vol. MS165, SPIE Optical Engineering Press, Washington, 2000, USA, pp. 461-469. Journal of Biomedical Optics, 3, (1), (1998), pp. 12-20.

A. Gh. Podoleanu, G. M. Dobre, D. J. Webb, D.A. Jackson "Coherence Imaging by Use of a Newton Rings Sampling Function", Republished in "Selected Papers on Optical Low-Coherence Reflectometry & Tomography", B. R. Masters and B. J. Thompson eds., SPIE Milestone Series, vol. MS165, SPIE Optical Engineering Press, Washington, 2000, USA, pp. 200-202.

A. Gh. Podoleanu, J. A. Rogers, B. Wacogne, S. Dunne, H. Porte, T. Gharbi, G. M. Dobre, D. A. Jackson, Towards 3D OCT Imaging, SPIE Proc. Vol., "Coherence Domain Optical methods in Biomedical Science and Clinical Applications", 3915, V. Tuchin, J. A. Izatt, eds, p. 46-54, (Conf. BIOS'2000, San Jose, 22-28 Jan., 2000).

G. M. Dobre, A. Gh. Podoleanu, D. A. Jackson, Extended Range, Micron Accuracy, Absolute Fibre-Optic Remote Distance Measurement System Based on Low Coherence Ranging, Proced. ODIMAP II, 2nd Top. Meeting on Optoel. Distance Measurement and Applic., Pavia, Italy., May. 20-22, 1999, LEOS Italy and Univ. Pavia, pp. 21-26, ISBN-88-87 237-06-9.

A. Gh. Podoleanu, G.M. Dobre, M. Seeger, D. J. Webb, D. A. Jackson, W. Fitzke, A.S. Halfyard, "Low Coherence Interferometry for En-face Imaging of the Retina", Lasers and light in ophthalmology, Vol. 8, No. 3, (1998), pp. 188-192.

A. Gh.Podoleanu, G. M. Dobre, D. A. Jackson, "En-face Coherence Imaging Using Galvanometer Scanner Modulation" Opt. Letters, (1998), vol. 23, pp. 147-149.

A.Gh.Podoleanu, G.M.Dobre, D.J.Webb, D.A.Jackson, "En-face imaging of the retina using path modulation introduced by the transversal scanning mirror", TOPS Vol.XXI, Advances in Optical Imaging and Photon Migration, J. G. Fujimoto and M. S. Patterson eds, pp. 325-330, OSA, Washington, DC, 1998, (shorter version in the Vol. of the OSA meeting: Advances in Optical Imaging and Photon Migration, March. 8-11, 1998, Orlando, pp. 83-85).

A.Gh.Podoleanu, M. Seeger, G.M.Dobre, D.J.Webb, D.A.Jackson, Adjustable depth resolution OCT imaging, Proc. SPIE, Vol. 3491, Applic. of Photonics Technology, G. A. Lampropoulos, R. A. Lessard, pp. 1158-1162 (ICAPT'98 Intern. Conf.), Ottawa, Canada, 27/07-30/07.

A.Gh.Podoleanu, M. Seeger, G.M.Dobre, D.J.Webb, D.A.Jackson, "Digital signal processing for fast OCT imaging", Applied optics and optoelectronics 1998, K T V Grattan ed. Brighton 16-19 March 1998, pp.140-144.

A. Gh.Podoleanu, G. M. Dobre, D. J. Webb, D. A. Jackson, "Fiberised Set-up for En-face Imaging of the Retina Using Low Coherence Interferometry" CLEO' 97, Baltimore, May 18-23, 1997, CTuT3, p. 168.

A. Gh.Podoleanu, G. M. Dobre, D. J. Webb, D. A. Jackson, "Low Coherence Interferometry for En-face Imaging of the Retina", 6th International Meeting on Scanning Laser Ophthalmoscopy, Tomography and Microscopy, Paris, 13-14 Febr. 1997

A. Gh.Podoleanu, G. M. Dobre, D. J. Webb, D. A. Jackson, "Simultaneous En-face Imaging of Two Layers in Human Retina" Opt. Lett., Vol. 22, No. 13, pp. 1039-1041 (1997)

A. Gh.Podoleanu, G. M. Dobre, D. J. Webb, D. A. Jackson "Fiberised Set-up for Eye Length Measurement" Full length article in Optics Commun., 137, pp. 397-405, (1997)

A.Gh.Podoleanu, G.M.Dobre, D.J.Webb, D.A.Jackson, "A Versatile system for Ocular Topographic Sensing Based on Two Low Coherence Interferometers", Volume of the 12th Int. Conf. on Optical Fiber Sensors, (OFS 1997), OSA, Washington DC, (1997), pp. OTHA6-1/369- OTHA6-4/372.

A.Gh.Podoleanu, G.M.Dobre, D.J.Webb, D.A.Jackson, "Fiberised Set-up for retinal Imaging of the Living Eye Using Low Coherence Interferometry", IEE Colloq. On Progress in Fibre Optic Sensors & their Applic., Savoy Place, 2 April. 1997, p.12/1-12/5.

A. Gh.Podoleanu, G. M. Dobre, D. J. Webb, D.A. Jackson "Coherence Imaging by Use of a Newton Rings Sampling Function", Opt. Lett., Vol. 21, pp. 1789-1791, (1996).

A.Gh.Podoleanu, G.M.Dobre, D.A.Jackson, A.T.Semenov, S.A.Safin, V.R.Shidlovski, "Three Electrode Laser as a Source and Detection Unit for Low Coherence Interferometry", OFS-11, 11th Intern. Conf. on Opt. Fiber Sensors, Sapporo, May 21-24, (1996), p.312-315.

Bibliography

1. G. E. Moss, L. R. Miller, R. L. Forward, "Photon noise limited laser transducer for gravitational antenna", Applied Optics, v. 10, pp. 2495-2498. 1971
2. D. A. Jackson, "Monomode optical fibre interferometers for precision measurement", Instrument Science and Technology, v. 18, 981-1001. 1985
3. K. Takada, I. Yokohama, K. Chida, J. Noda, "New measurement system for fault location in optical waveguide devices based on an interferometric technique", Applied Optics, v. 26, pp. 1603-1606. 1987
4. R. C. Youngquist, S. Carr, D. E. N. Davies, "Optical coherence-domain reflectometry: A new optical evaluation technique", Optics Letters, v. 12, pp. 158-160. 1987
5. H. H. Gilgen, R. P. Gilgen, R. P. Salathe, "Submillimeter optical reflectometry", Journal of Lightwave Technology, v.7, pp. 1225-1233. 1989
6. L. Deck, P. De Groot, "High-speed noncontact profiler based on scanning white light interferometry", Applied Optics, v. 33, pp. 7334-7338. 1994
7. A. Knuttel, J. M. Schmitt, "Stationary depth-profiling interferometer based on low-coherence interferometry", Optics Communications, v.102, pp. 193-198. 1993
8. D. P. Hand, T. A. Carolan, J. S. Barton and J. D. C. Jones, "Profile measurement of optically rough surfaces by fibre optic interferometry". Optics Letters, v.18, pp.1361-1363. 1993
9. V. Gelikopnov, A. Sergeev, G. Gelikonov, F. Feldchtein, N. Gladkova, J. Ioannovich, K. Fragia, T. Pirza, "Compact fast-scanning OCT device for in-vivo biotissue imaging", Conference on lasers and electro-optics, vol. 9, pp. 58-59. 1996

10. J. A. Izatt, H. W. Wang, M. Kulkarni, M. I. Canto, M. V. Sivak, "Optical coherence tomography in gastrointestinal tissues", Conference on lasers and electro-optics, vol. 9, pp.56-57. 1996

11. T. C. Strand, Y. Katzir, "Extended unambiguous range interferometry", Applied Optics, v. 26, pp. 4274-4281. 1987

12. C. C. Williams, H. K. Wickramasinghe, "Optical ranging by wavelength multiplexed interferometry", J. Applied Physics, v. 60, pp. 1900-1902. 1986

13. K. Creath, "Measuring step heights using an optical profiler", Proceedings SPIE, v. 661, pp. 296-301. 1986

14. K. Creath, J. C. Wyant, "Absolute measurement of surface roughness", Applied Optics, v. 29, pp. 3823-3827. 1990

15. E. Hecht, "Optics", 2nd edition, Addison-Wesley publishing company, Inc. 1987

16. W. H. Woon, F. W. Fitzke, A. C. Bird, J. Marshall, "Confocal imaging of the fundus using a scanning laser ophthalmoscope". British Journal of Ophthalmology, v. 76, pp. 470-474. 1992

17. T. Wilson, "Scanning optical microscopy", International Journal of Optoelectronics, v.3, pp.121-152. 1988

18. D. K. Hamilton, T. Wilson, "Scanning optical microscopy by objective lens scanning", Journal Of Physics E-Scientific Instruments, v.19, pp.52-54. 1986

19. T. Dresel, G. Hausler, H. Venzke, "Three-dimensional sensing of rough surfaces by coherence radar", Applied Optics, v. 31, pp. 919-925. 1992

20. G. Hausler, J. Neumann, "Coherence radar - an accurate 3-D sensor for rough surfaces", Proceedings of the Society of Photonics Instrumentation engineers, pp. 200-205. 1992

21. A. Quigley, E. M. Addicks, "Regional differences in the structure of the lamina cribrosa and their relation to glaucomatous optic nerve damage". Archives of Ophthalmology v. 99, pp. 137-143. 1981

22. R. Klein, B. E. K. Klein, S. E. Moss, "Visual impairment in diabetes", Ophthalmology, v. 91, pp.1-9. 1984

23. C. A. Puliafito, M. R. Hee, C. P. Lin, E. Reichel, J. S. Schuman, J. S. Duker, J. A. Izatt, E. A. Swanson, J. G. Fujimoto, "Imaging of macular diseases with optical coherence tomography", Ophthalmology, v. 102, pp. 217-229. 1995

24. The Eyecare Professionals' Premier Online Information Resource Web Site, http://www.eyemax.com/ocularlinks/index.html

25. J. L. Taveras, B. G. Halik, "Magnetic resonance imaging in ophthalmoscopy", B. R. Masters ed., "Noninvasive diagnostic techniques in ophthalmology", New York, Springer Verlag NY Inc., pp. 32-46. 1990

26. W. Drexler, C. K. Hitzenberger, H. Saltmann, A. F. Fercher, "Measurement of the thickness of fundus layers by partial optical coherence tomography", Optical Engineering, v. 34, pp. 701-709. 1995

27. C. J. Pavlin, M. D. Sherar, F. S. Foster, "Subsurface ultrasound microscopic imaging of the intact eye", Ophthalmology, v. 97, pp. 244-50. 1990

28. C. J. Pavlin, K. Harasiewicz, M. D. Sherar, F. S. Foster, "Clinical use of ultrasound biomicroscopy". Ophthalmology, v. 98, pp. 287-95. 1991

29. M. Shahidi, Y. Ogura, N. P. Blair, M. M. Rusin, R. Zeimer, "Retinal thickness analysis for quantitative assessment of diabetic macular edema", Archives of Ophthalmology, v. 109, pp.1115-1119. 1991

30. V. S. Lee, R. M. Kingsley, E. T. Lee, M. Lu, D. Russell, N. R. Asal, R. H. Bradford, C. P. Wilkinson, "The diagnosis of diabetic-retinopathy - ophthalmoscopy versus fundus photography" Ophthalmology, v.100, pp.1504-1512. 1993

31. C. K. Hitzenberger, W. Drexler, C. Dolezal, F. Skorpik, M. Juchem, A. F. Fercher, H. D. Gnad, "Measurement of the axial eye length of cataract eyes by laser Doppler interferometry", Investigations in Ophthalmology and Visual Science, v. 34, pp. 1886-1893. 1993

32. A. W. Dreher, E. D. Bailey, "Retinal nerve fiber thickness measurement by scanning laser polarimetry", Vision Science and Its Applications, Technical Digest Series, v. 2, pp. 122-125, OSA Washnigton DC. 1994

33. R. H. Webb, F. C. Delori, "How we see the retina", In J. Marshall, ed. "Laser technology in ophthalmology", Amsterdam, Kugler and Ghedini publications, pp. 3-14. 1990

34. J. A. Izatt, M. R. Hee, G. M. Owen, E. A. Swanson, J. G. Fujimoto, "Optical coherence microscopy in scattering media", Optics Letters, v. 19, pp. 590-592. 1994

35. J. M. Schmitt, A. Knuttel, R.F. Bonner, "Measurement of optical properties of biological tissues by low coherence reflectometry", Applied Optics, v. 32, pp. 6032-6042. 1993

36. D. Weinberger, H. Stiebel, D. D. Gaton, E. Priel, Y. Yassur, "Three-dimensional measurements of idiopathic macular holes using a scanning laser tomograph", Ophthalmology, v. 102, pp.1445-1449. 1995

37. J. M. Schmitt, A. Knuttel, R.F. Bonner, "Measurement of optical properties of biological tissues by low coherence reflectometry", Applied Optics, v. 32, pp. 6032-6042. 1993

38. A. P. Fercher, "New techniques in OCT", Proceedings CLEO 96, pp.54-55. 1996

39. M. Born, E. Wolf, "Principles of Optics", Pergamon Press, 6th edition. 1980

40. A. Yariv, "Introduction to Optical Electronics", Holt Rinehart and Winston Publishing, Inc.1971

41. A. Siegman, Lasers, University Science Books. 1986

42. "Fibre Optic Sensors: An Introduction for Engineers and Scientists", Edited by Eric Udd. John Wiley and Sons, Inc. 1991

43. J. W. Goodman, Statistical Optics, Wiley. 1985

44. J. Godgebuer, A. Hamed, H. Porte, N. Butterlin, "Analysis of optical crosstalk in coherence multiplexed systems employing a short coherence laser diode with arbitrary power spectrum" Journal of Quantum Electronics, v. 26, pp. 1217. 1990

45. M. R. Hee, J. A. Izatt, E. A. Swanson, D. Huang, J. S. Schuman, C. P. Lin, C. A. Puliafito, J. G. Fujimoto, "Optical coherence tomography of the human retina", Archives Of Ophthalmology, Vol.113, pp.325-332. 1995

46. N. A. Zhuchkov, S.A.Safin, A.T. Semenov and V. R. Shidlovski, "Multifunctional semiconductor light sources and modules based on them", Soviet Journal of Quantum Electronics, v. 21, pp. 1176-1178. 1991

47. A. Simon, R. Ulrich, "Evolution of polarization along a single-mode fibre", Appl. Phys. Lett, vol. 31, p. 517. 1977

48. A. Kohlhaas, C. Fromchen, E. Brinkmeyer, "High-resolution OCDR for testing integrated-optical waveguides: dispersion corrupted experimental data corrected

by a numerical algorithm", Journal of Lightwave Technology, v. 9, pp. 1493-1502. 1991

49. N. Shibata, M. Tsubokawa, T. Nakashima and S. Seikau, "Temporal coherence properties of a dispersively propagating beam in a fiber-optic interferometer", J. Opt. Soc. Am. A, v. 4, pp. 494- 497. 1987
50. H. J. Aronson, "Acousto-optic scanning", Laser Focus, v. 12, p. 36-39. 1976
51. A.Gh.Podoleanu, G.M.Dobre, D.A.Jackson, A.T.Semenov, S.A.Safin, V.R.Shidlovski, "Three Electrode Laser as a Source and Detection Unit for Low Coherence Interferometry", OFS-11, 11th Intern. Conf. on Opt. Fiber Sensors, Sapporo, May 21-24, (1996), p.312-315
52. A.S. Gerges, T.P. Newson and D.A. Jackson, "Coherence tuned fiber optic sensing system with self-initialisation, based on a multimode laser diode", Applied Optics, Vol. 29, pp. 4473-4480, 1990.
53. A. Gh. Podoleanu, S. R. Taplin, D. J. Webb and D. A. Jackson, "Channelled Spectrum Display Using a CCD Array for Student Laboratory Demonstrations", Euro. J. Phys., v. 15, pp.266-271. 1994
54. D. N. Wang, S. Chen, K. T. V. Grattan and A. W. Palmer, "A low coherence "white light" interferometric sensor for eye length measurement", Rev. Sci. Instrum., v. 12, pp. 5464-5468. 1995
55. K. Takada, A. Himeno and K. Yukimatsu, "Phase-noise and shot-noise limited operations of low coherence optical time domain reflectometry", Appl. Phys. Lett, v. 20 , pp. 2483-2485. 1991
56. A. Gh. Podoleanu, G. M. Dobre, D. J. Webb, D. A. Jackson, "Fiberised Set-up for Eye Length Measurement", Optics Commun., 137, (1997), pp. 397-405.
57. V. Greco, G. Molesini and F. Quercioli, Remarks on the Gaussian formula for refraction at a single spherical interface", Am. J. Phys., v. 60, pp. 131-135. 1992
58. A. F. Leung and J. E. Lee, "Newton's rings: A classroom demonstration with a He-Ne laser", Am. J. Phys, v. 59, pp. 663-664. 1991
59. A. Gh.Podoleanu, G. M. Dobre, D. J. Webb, D. A. Jackson, "Coherence Imaging by Use of a Newton Rings Sampling Function", Opt. Lett., Vol. 21, No. 21, (1996), pp. 1789-1791.

60. A. Gh. Podoleanu, G. M. Dobre, D. A. Jackson, "En-face Coherence Imaging Using Galvanometer Scanner Modulation", Opt. Letters, (1998), vol. 23, pp. 147-149.

61. A. F. Fercher, "Optical coherence tomography", J. Biomed. Opt., v. 2, pp. 157-173. 1996

62. B. Bouma, G. J. Tearney, S. A. Boppart, M. R. Hee, M. E. Brezinski, J. G. Fujimoto, "High-resolution optical coherence tomographic imaging using a mode-locked Ti:Al_2O_3 laser source", Opt. Lett., v. 20, pp. 1486-1488. 1995

63. G. J. Tearney, B. E. Bouma, S. A. Boppart, B.Golubovic, E. A.Swanson and J. G. Fujimoto, Opt. Lett., v. 21, No.17, pp. 1408-1410. 1996

64. E. A. Swanson, J. A. Izatt, M. R. Hee, D. Huang, C.P. Lin, J. S. Schuman, C. A. Puliafito and J. G. Fujimoto, "In vivo retinal imaging by optical coherence tomography", Opt. Lett., v. 18, pp. 1864-1867. 1993

65. C. B. Su, "Achieving variation of the optical path length by a few millimetres at millisecond rates for imaging of turbid media and optical interferometry: a new technique", Opt. Lett, v. 22, No. 10, pp. 665-667. 1997

66. Y. Le Grand, "Light, Colour, and Vision". London, Chapman and Hill. 1968

67. A. Gh. Podoleanu, J. A. Rogers, D. A. Jackson, S. Dunne, "Three dimensional OCT images from retina and skin," Opt. Express 7, 292-298 (2000)

68. American National Standards Institute, "American National Standards for Safe Use of Lasers ANSI Z136.1-1993", Orlando, Florida, The Laser Institute of America, pp. 41-42. 1993